

Calculation of Gluon PDF in the Nucleon using Pseudo-PDF Formalism with Wilson  
Flow Technique in LQCD

Md Tanjib Atique Khan

Jessore, Bangladesh

Master of Science, College of William & Mary, 2017  
Bachelor of Science, Bangladesh University of Engineering and Technology, 2006

A Dissertation presented to the Graduate Faculty  
of The College of William & Mary in Candidacy for the Degree of  
Doctor of Philosophy

Department of Physics

College of William & Mary  
January 2022

©  
Md Tanjib Atique Khan  
All rights reserved.

## APPROVAL PAGE

This Dissertation is submitted in partial fulfillment of  
the requirements for the degree of

Doctor of Philosophy



---

Md Tanjib Atique Khan

Approved by the Committee November 2021



---

Committee Chair  
Konstantinos Orginos, Professor, Physics  
College of William & Mary



---

Committee Co-Chair  
David Richards, Adjunct Professor, Physics  
College of William & Mary



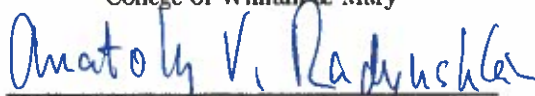
---

David Armstrong, Professor, Physics  
College of William & Mary



---

Christopher Monahan, Assistant Professor, Physics  
College of William & Mary



---

Anatoly Radyushkin, Professor, Physics  
Old Dominion University

## ABSTRACT

A comprehensive study of the gluonic content in the nucleon from a first principles lattice quantum chromodynamics calculation is presented. The unpolarized gluonic distribution in the nucleon is calculated using the pseudo-PDF framework on the lattice. First, the spectral analyses of the low-lying states in the nucleon, as well as in the  $\Delta$  are performed on the lattice, identifying baryon states with hybrid characteristics, in which the gluons play a manifestly structural role, and determining a set of operators which have significant overlaps onto the ground state of the nucleon. Techniques such as distillation for smearing the quark fields, momentum smearing to achieve a better signal at the higher momenta, the gradient flow technique for suppressing the gauge fluctuations, and the solution of the summed generalized eigenvalue problem employing a set of operators determined by the nucleon spectral analysis are implemented to calculate the gluonic matrix elements. A combination of these techniques provides the most precise lattice determination of the gluonic distribution in the nucleon to date. Short distance factorization provides the perturbative matching kernel which, in turn, allowed us to calculate the gluon Ioffe-time distribution in the  $\overline{\text{MS}}$  scheme at  $\mu = 2$  GeV. To accomplish this task, a parametrization in terms of Jacobi polynomials is used in an approximation in which the mixing with the quark singlet sector is neglected. Finally, the results are compared with the phenomenological determinations.

# TABLE OF CONTENTS

Acknowledgments . . . . .	iv
Dedication . . . . .	v
List of Tables . . . . .	vi
List of Figures . . . . .	vii
CHAPTER	1
1 Introduction . . . . .	2
2 Parton Model and Light-cone PDF . . . . .	8
2.1 Parton Model . . . . .	8
2.2 Successes and Limitations . . . . .	12
2.3 Field-theoretic Implementation . . . . .	13
3 Lattice QCD . . . . .	16
3.1 Clover Fermion Action . . . . .	17
3.1.1 Naive Fermion Action . . . . .	17
3.1.2 Wilson Fermion . . . . .	19
3.1.3 Wilson Gauge Action . . . . .	20
3.1.4 Symanzik Improvement . . . . .	22
3.2 Importance Sampling and Lattice QCD . . . . .	24
3.3 PDF on the Lattice . . . . .	29
4 Computational Details . . . . .	33
4.1 Distillation . . . . .	34
4.2 Momentum Smearing . . . . .	37

4.3	Lattice Details . . . . .	38
5	Positive-parity Nucleon and Delta Spectra . . . . .	40
5.1	Baryon Interpolators . . . . .	41
5.2	Variational Method . . . . .	45
5.3	Fitting Procedure . . . . .	48
5.4	Spin Identification . . . . .	50
5.5	Stability under variation of Distillation Space . . . . .	53
5.6	Delta and Nucleon Spectra . . . . .	56
5.6.1	Hybrid States . . . . .	58
5.7	Comparison with Previous Work . . . . .	59
6	Gluon PDF Calculation . . . . .	66
6.1	Theoretical Background . . . . .	66
6.1.1	Matrix Elements . . . . .	66
6.1.2	Reduced Matrix Elements . . . . .	68
6.1.3	Position-space Matching . . . . .	69
6.2	Computational Framework . . . . .	71
6.2.1	Gluonic Current Calculation . . . . .	71
6.2.2	Gradient Flow . . . . .	74
6.2.3	Nucleon Two-point Correlator . . . . .	76
6.3	Variational Analysis . . . . .	78
6.4	Matrix Element Extraction . . . . .	81
6.4.1	Three-point Correlator . . . . .	81
6.4.2	sGEVP Method . . . . .	82
6.4.3	Bare Matrix Elements . . . . .	86
6.4.4	Autocorrelation of the Matrix Elements . . . . .	89

6.4.5	Bayesian Analysis . . . . .	92
6.4.6	Reduced Matrix Elements and Zero Flow Time Extrapolation . . . . .	99
6.5	Gluon PDF Extraction . . . . .	102
6.5.1	Jacobi Polynomial Parametrization . . . . .	102
6.5.2	Comparison with Phenomenological PDFs . . . . .	117
7	Conclusion and Outlook . . . . .	122
	Bibliography . . . . .	125

## ACKNOWLEDGMENTS

First and foremost, I would like to thank my Ph. D. advisor Konstantinos Orginos. During my study at College of William & Mary, he has been a constant source of inspiration to me. Whenever I got stuck on a problem, I could approach him, and he would help me steer in the right direction. Last year, when I developed tennis elbow in my right arm, it was Kostas's encouragement and support which led me to complete the projects and fulfill the requirements for the Ph. D. degree.

I am especially grateful to my co-advisor David Richards. He is the person who helped me get familiarized with the complicated systems of Jefferson Lab and other supercomputing systems which were essential to my research. His constant encouragement and fruitful discussions on different research topics greatly assisted me in my research work.

I would like to express my gratitude to Mohammed Arshad Momen and Golam Mohammed Bhuiyan, professors of physics at the University of Dhaka, Bangladesh who encouraged me to pursue physics.

My special thanks go to Raza Sabbir Sufian for his unwavering support and countless discussions and suggestions which have been vital to my research. I cannot thank Joseph Karpie enough for we have spent hours on having insightful discussions related to my research, and debugging complicated codes. I want to thank all the members of the HadStruc collaboration for the fruitful and stimulating exchanges, especially Eloy Romero for his help in solving numerous coding-related issues.

I am forever thankful to Archana Radhakrishnan and Luka Leskovec for offering their help, which greatly assisted my research.

I want to thank my friends Azam Babul, Sabiha Sultana Jui, Amit Seal Smi, Prianka Mandal, Nur-E-Tanjim, Dibhya Saha, and Obaidul Kabir Rubayed for their support, especially when I needed them the most.

I would like to thank my parents and my sister who encouraged me to pursue my study in physics.

Last but not least, I would like to thank the Almighty Allah for everything.

This work is dedicated to my parents, Atique and Parul, and my sister Simmee, whose encouragement and inspiration led me where I am today.

## LIST OF TABLES

4.1	The ensemble parameters. . . . .	39
5.1	The $\Delta$ and $N$ interpolating operators for baryon spectra calculation. . . . .	44
6.1	The nucleon interpolating operators used in the gluon distribution calculation. . . . .	77
6.2	Nucleon interpolators of the models to construct matrix elements. . . . .	88
6.3	The fitted parameters and the goodness-of-fits for the matrix elements shown in Figure 6.9. . . . .	97
6.4	The reduced matrix elements extrapolated to the zero flow time. . . . .	102
6.5	The goodness-of-fit quantities of different models used to perform the Jacobi polynomial parametrization. . . . .	115

## LIST OF FIGURES

1.1	Phenomenological parton distribution functions of the up, down, strange quarks, their corresponding antiquarks and gluon in the nucleon . . . . .	4
2.1	The handbag diagram, and the parton model in the field theory for the quark distribution. . . . .	10
2.2	The gauge invariant diagram for the unpolarized gluon distribution. . . . .	14
3.1	The plaquette, $U_{\mu,\nu}(n)$ . . . . .	22
3.2	Graphical representation of the sum, $Q_{\mu\nu}(n)$ . . . . .	24
5.1	Fits to the principal correlators for the low-lying positive-parity spectrum of the $\Delta$ . . . . .	49
5.2	Histogram plot of the operator overlaps for the $\Delta$ . . . . .	51
5.3	Comparison of the low-lying $\Delta$ spectra between the operators within an irrep. from a given angular momentum and all operators within a lattice irrep.. . . . .	53
5.4	The dependence of the $\Delta$ spectrum on the number of distillation eigenvectors. . . . .	54
5.5	Operator overlap distribution of the $\Delta$ for different number of distillation eigenvectors. . . . .	55
5.6	The low-lying positive-parity $\Delta$ spectrum on the <i>a094m278</i> and <i>a094m358</i> ensembles. . . . .	57
5.7	The low-lying positive-parity $N$ spectrum the <i>a094m278</i> and <i>a094m358</i> ensembles. . . . .	58
5.8	The excitation energies for the $\Delta$ with respect to the ground state nucleon. . . . .	60
5.9	The excitation energies for the $N$ with respect to the ground state nucleon. . . . .	61
5.10	The operator overlap distribution of the $\Delta$ for the ensembles <i>a094m278</i> , <i>a094m358</i> and from [1]. . . . .	63
5.11	The operator overlap distribution of the $N$ for the ensembles <i>a094m278</i> , <i>a094m358</i> and from [1]. . . . .	64

6.1	Graphical representation of the gluonic current, $O(G_{\mu\alpha}, G_{\lambda\beta}, z)$ . . . . .	72
6.2	Fits to the principal correlators for the nucleon with $p = 0.82$ GeV. . . . .	79
6.3	Fits to the principal correlators for the nucleon with $p = 2.46$ GeV. . . . .	80
6.4	The ground state nucleon dispersion relation. . . . .	81
6.5	Overlap of the operators onto the ground state of the nucleon for different momenta. . . . .	87
6.6	Comparing the matrix elements calculated using different sets of interpolators. . . . .	89
6.7	The integrated autocorrelation time of the bare matrix elements. . . . .	92
6.8	Fitting the matrix elements with different fit expressions. . . . .	94
6.9	Extraction of the matrix elements using the sGEVP method. . . . .	98
6.10	The reduced matrix elements, $\mathfrak{M}(\nu, z^2)$ with respect to the Ioffe-time for the flow time = 1.0 in lattice units. . . . .	100
6.11	The reduced matrix elements, $\mathfrak{M}(\nu, z^2)$ with respect to the Ioffe-time for the flow time = 1.4 in lattice units. . . . .	103
6.12	The reduced matrix elements, $\mathfrak{M}(\nu, z^2)$ with respect to the Ioffe-time for the flow time = 1.8 in lattice units. . . . .	104
6.13	The reduced matrix elements, $\mathfrak{M}(\nu, z^2)$ with respect to the Ioffe-time for the flow time = 2.2 in lattice units. . . . .	105
6.14	The reduced matrix elements, $\mathfrak{M}(\nu, z^2)$ with respect to the Ioffe-time for the flow time = 2.6 in lattice units. . . . .	106
6.15	The reduced matrix elements, $\mathfrak{M}(\nu, z^2)$ with respect to the Ioffe-time for the flow time = 3.0 in lattice units. . . . .	107
6.16	The reduced matrix elements, $\mathfrak{M}(\nu, z^2)$ with respect to the Ioffe-time for the flow time = 3.4 in lattice units. . . . .	108
6.17	The reduced matrix elements, $\mathfrak{M}(\nu, z^2)$ with respect to the Ioffe-time for the flow time = 3.8 in lattice units. . . . .	109
6.18	The reduced matrix elements extrapolated to the $\tau \rightarrow 0$ limit. . . . .	110
6.19	The reduced Ioffe-time pseudo-distribution plotted with respect to the Ioffe-time. . . . .	111
6.20	Comparison among the light-cone Ioffe-time distributions calculated from different models. . . . .	113
6.21	Comparison among the $xg(x)$ distributions calculated from different models. . . . .	114
6.22	The lattice reduced pseudo-ITD shown along with their reconstructed fitted bands calculated for the model: 2-param (Q). . . . .	116
6.23	The Ioffe-time distribution along with the light-cone ITD calculated for the model: 2-param (Q). . . . .	117
6.24	The unpolarized gluon PDF extracted from the lattice data using the 2-param (Q) model. . . . .	119

6.25	The unpolarized gluon PDF shown in log-scale to enhance the view of the large- $x$ region. . . . .	120
------	--	-----

CALCULATION OF GLUON PDF IN THE NUCLEON USING PSEUDO-PDF  
FORMALISM WITH WILSON FLOW TECHNIQUE IN LQCD

# CHAPTER 1

## Introduction

Most of the visible universe is made of leptons such as electrons, and hadrons such as protons and neutrons. The method of classifying hadrons, according to the symmetry properties, known as the Eightfold Way, not only leads to the prediction of the existence of heavier hadrons but also puts forth the idea that hadrons might have internal structures. Indeed, to explain the basis of the Eightfold Way, in 1964, Murray Gell-Mann [2] theorized that hadrons consist of quarks, establishing the foundation for the modern quark model of hadrons. This concept of hadrons having inner structure was established through the Nobel-prize winning SLAC-MIT experiment [3]. From then, understanding the structure of hadrons in terms of quarks and gluons has been one of the holy grails of modern physics. There is a long history of exploring the nature of hadrons through investigating the energy spectra, but deep inelastic scattering processes (DIS) in which hadrons are probed with leptons allow us to enhance our knowledge regarding hadrons in-depth.

Hadrons are classified into two groups: mesons with integer spin, and baryons with half-integer spin. The lightest baryon is the nucleon, which is a collective name for protons and neutrons. The nucleon is one of the most important building blocks of almost

everything in the visible universe.

Most of the resonances registered in the Particle Data Group [4], which stem from the analysis of scattering data from different experiments, can be explained by phenomenological approaches like the quark model [5, 6, 7] which exhibits a counting of energy levels commensurate with  $SU(6) \otimes O(3)$  spin-flavor symmetry [8]. Also predicted are “hybrid” baryon states [1] for which there is no evidence in the spectra obtained from the scattering experiments, but suggested by various models describing the behaviors of hadrons. Such models include the bag model [9] where the quark and gluon fields are confined within a cavity with the fields satisfying appropriate boundary conditions at the wall of the cavity. In the flux-tube model [10, 11], quarks sit at the ends of a string-like structure. A meson contains a single flux tube between a quark and an antiquark; in a hybrid meson, this string is excited by a transverse oscillation. For the case of a baryon, there are three tubes that either meet at a junction or form a triangle. There is also the QCD sum rule method [12] that makes predictions about the hybrid baryons.

In the hybrid baryons, the gluonic degrees of freedom play an essential, structural role, with a common mechanism with comparable states in the meson spectra. For the case of mesons, there can exist “exotic” states that have quantum numbers  $J^{PC}$  not available within a regular  $q\bar{q}$  valence structure. Such states may have a dominant  $qq\bar{q}\bar{q}$  component, the so-called tetraquarks [13, 14], or be predominantly “hybrid”  $q\bar{q}g$  states [15, 16, 17, 18, 19], with a manifestation of the gluonic valence component. Thus it is straightforward to separate some “exotic” meson states from regular ones. But for baryons, the regular  $qqq$  states can have all the  $J^P$  values. So, the hybrid states will always have to “share” quantum numbers with the regular states, thus making them very difficult to identify.

To explain the experimental results of  $N\pi$  scattering, the concept of an excitation of the nucleon with the mass between its ground state and first negative parity state  $N^*(1535)$ , was introduced [20]. This excitation,  $N^*(1440)$  is known as the Roper resonance.

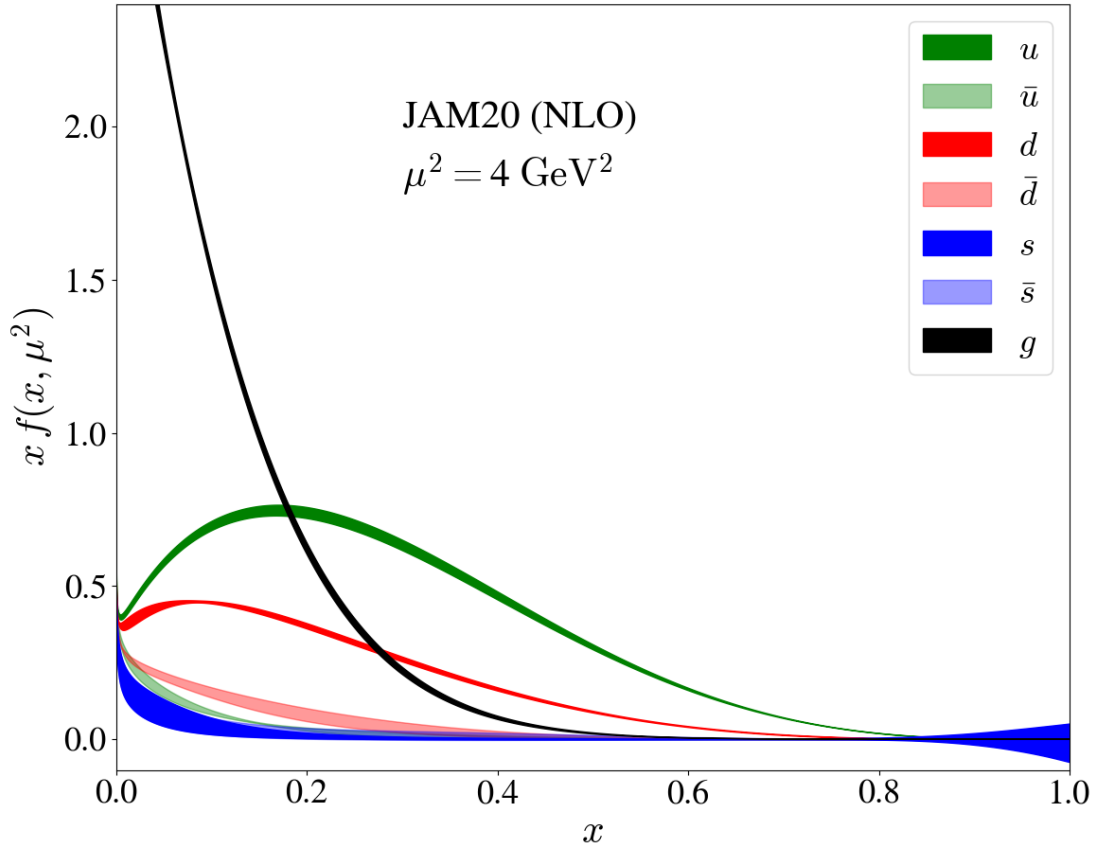


FIG. 1.1: Phenomenological parton distribution functions (PDFs) of the up ( $u$ ), down ( $d$ ), strange ( $s$ ) quarks, their corresponding antiquarks and gluon in the nucleon from global fits to experimental data, JAM20 [26] for next-to-leading (NLO) PDF parametrizations at renormalization scale,  $\mu^2 = 4 \text{ GeV}^2$ .

Within the quark model, the Roper has been identified predominantly as a  $qqq$  state augmented by a meson cloud [21], but the quark model fails to predict the low-mass Roper seen in the experiments. Hybrid baryon, i.e. a  $qqqg$  with nontrivial gluonic structure [22, 23] and a  $qqqq\bar{q}$  like structure [24, 25] have been suggested in an attempt to explain the Roper resonance.

With the rise of the deep inelastic scattering (DIS) experiments, which can provide us a better picture of the internal structure of hadrons, the interest in investigating the nucleon more closely is growing, the goal being to understand the behavior of partons, as quarks and gluons are called collectively, inside hadrons. One way to probe the internal

structure of hadrons is to examine the parton distribution function (PDF) which is the probability density of finding the corresponding parton with a longitudinal momentum fraction  $x$  in a hadron.

There are long-standing efforts to conduct the global analyses [27, 28, 29, 30, 31] of the data from the available DIS and the related hard scattering processes to explore the nature of the PDFs. In Figure 1.1, the phenomenological PDFs in the nucleon from global fits to experimental data, JAM20 [26] is shown. High energy experiments such as the Higgs boson production [32] and jet production [33] at the Large Hadron Collider (LHC), and the  $J/\psi$  photo production [34] at Jefferson Lab are means of determining the gluon PDFs. Future colliders, such as the Electron-Ion Collider (EIC) [35, 36, 37], which is to be built at the Brookhaven National Lab, and the Electron-Ion Collider in China (EicC) [38], are expected to make a significant impact on the precision of the gluon PDFs. While the precision of the extracted gluon distribution,  $g(x)$  has been improved over the last decade, several issues remain unresolved; for example, the suppression of the PDF in the momentum fraction region  $0.1 < x < 0.4$  when ATLAS and CMS jet data are included [28] and how to obtain a more precise determination of  $g(x)$  are subjects of ongoing efforts.

The interactions among the partons are governed by the electromagnetic, the weak, and the strong forces. As the electromagnetic and the weak interactions are perturbative around the accessible energy and distance scale, the theoretical formulations of these interactions are perturbative in nature, given by the  $SU(2) \otimes U(1)$  electroweak theory. For the strong force, however; the mathematical treatment becomes complicated as this interaction is non-perturbative.

The initial formulation of a quantum field theory for the strong interactions was done by Yang and Mills [39] by replacing the abelian symmetry of quantum electrodynamics (QED) with a non-abelian group. Necessary modifications were added to formulate a Lagrangian with both the gauge fields and quark fields; this becomes quantum chromody-

namics (QCD). The physics community became interested when the asymptotic freedom of QCD was discovered by David Politzer [40], and independently by David Gross and Frank Wilczek [41]. The strong interaction is asymptotically free in the sense that the coupling of strong interaction increases significantly at large distances and drops at short distances. Only a non-abelian gauge theory can let the effective coupling between quarks go to zero at zero distance, making quarks asymptotically free within hadrons.

In analytical calculations employing QCD, ultra-violet (UV) divergences appear. These divergences are absent in physical quantities and need to be removed. The process of removing these UV divergences is known as renormalization. QCD is a renormalizable theory making it a suitable candidate to describe strong interactions. QCD needs to be a  $SU(3)$  gauge theory to incorporate the properties of quarks and gluons. This additional degree of freedom is known as the color-charge. The Lagrangian of QCD is given by

$$\mathcal{L} = \sum_q \bar{\psi}_q^\alpha (i\not{D}_{\alpha\beta} - m_q\delta_{\alpha\beta}) \psi_q^\beta - \frac{1}{4}[G_a^{\mu\nu} G_{\mu\nu}^a]. \quad (1.1)$$

Here, the sum is over the different flavors of quarks,  $\psi_q$  is the quark field for the quark of flavor,  $q$ ,  $D_{\alpha\beta}^\mu = \partial^\mu\delta_{\alpha\beta} - ig t_{\alpha\beta}^c A_c^\mu$  is the gauge covariant derivative in the  $SU(3)$  symmetry group,  $G_{\mu\nu}^a = \partial_\mu A_\nu^a - \partial_\nu A_\mu^a - gf^{abc} A_{\mu b} A_{\nu c}$  is the field-strength tensor,  $t^c$  are the generating matrices,  $f^{abc}$  are the structure constants for  $SU(3)$  symmetry group,  $\alpha, \beta$  are the color indices,  $a, b, c$  are the indices of the  $SU(3)$  generators, and  $\mu, \nu$  are the spacetime indices. The non-abelian  $SU(3)$  symmetry allows the massless strong force-carrying bosons, the gluons, to interact with each other, in contrast to the  $U(1)$  theory of QED.

In nature, only color-neutral particles are found to exist freely; no observation of any particle with net color-charge has been made to date. In hadrons, quarks always form color-singlet states. This property of strong interactions is known as color confinement. Confinement is not analytically proved in QCD; it is an assumption based on the related

observations and experiments.

Because of the non-perturbative nature of QCD at the hadronic scale, an analytical calculation of the PDFs is not possible. One way to circumvent this problem is to perform the calculation with the lattice regularized QCD [42] where the spacetime locations of the fields are restricted to be on the sites or the links between the sites of a four-dimensional lattice with the discretization acting as the regulator. Lattice QCD is the only first principles determination of QCD in the non-perturbative regime.

In this dissertation, two manifestations of gluon degrees of freedom in the nucleon are explored. The first concerns the evidence for “hybrid” baryons, where gluon degrees of freedom are manifest. The results of this lattice calculation are published in [43]. The second concerns the role of gluons in the structure of the ground state nucleon through the calculation of the gluon PDF. The results of this lattice calculation are published in [44]. This dissertation is organized as follows. Chapter 2 discusses the parton model, and its successes and limitations. In chapter 3, the lattice regularized QCD and the techniques of performing the PDF calculations on the lattice are presented. Chapter 4 details the methodologies implemented on the relevant lattices and the associated parameters. In chapter 5, the spectral analyses of the delta and the nucleon are presented. In chapter 6, the gluon PDF in the nucleon is extracted from the lattice calculation. Chapter 7 presents some concluding remarks.

# CHAPTER 2

## Parton Model and Light-cone PDF

Multiple attempts were made to model the strong interaction before the formulation of QCD. We can look at some of these approaches which give an intuitive picture of the strong interactions before discussing QCD. The parton model is one of these approaches.

### 2.1 Parton Model

The parton model was formulated by Feynman [45] and formalized by Bjorken and Paschos [46] to understand the deep inelastic scattering (DIS) where a lepton,  $l$  is scattered on a hadron,  $N$ , producing one or more different hadrons. The lepton can be an electron, muon, or neutrino and the hadron can be a nucleon or a heavier nucleus. The process can be expressed as:

$$l + N(P) \rightarrow l' + X . \tag{2.1}$$

Here, the incoming lepton's momentum is  $l^\mu$ , the incoming hadron's momentum is  $P^\mu$ , the outgoing lepton's momentum is  $l'^\mu$  and  $X$  denotes the final hadronic state. This is

an inclusive process in that only the outgoing lepton is detected. The process can be an electron beam colliding against a proton beam, like in the HERA accelerator at the DESY laboratory or the future EIC, or an electron beam focused into a container of liquid hydrogen, like at the Jefferson Laboratory.

A hadron, such as a proton, has a size of around 1 fm. So, in the hadron's rest frame, the constituents of the hadron interact with each other on a time scale of order 1 fm/c. This motivated Feynman to approximate that when the spacelike momentum transfer,  $q^\mu = l^\mu - l'^\mu$  is large in the short-distance electron-constituent collision, the interactions that bind the constituents into a hadron can be neglected.

In the parton model, Feynman proposed that in the DIS, the photon coming from the lepton couples to a single constituent of the target hadron, and the strong interactions among the constituents of the hadron during the collision can be neglected. Generally, in the calculation, it is convenient to use the Breit frame, where the hadron's momentum is in the  $+z$  direction and the virtual photon's momentum is in the  $-z$  direction. So, in this frame, the struck quark gets its 3-momentum exactly reversed. It is also preferred to use the light-front coordinates [47]. If the Lorentz coordinates of a vector  $a$  are  $a^0, a^1, a^2, a^3$ , then the light-front coordinates of  $a$  are defined as:

$$\begin{aligned} a^+ &= \left( \frac{1}{\sqrt{2}} \right) (a^0 + a^3), \\ a^- &= \left( \frac{1}{\sqrt{2}} \right) (a^0 - a^3), \end{aligned} \tag{2.2}$$

The other two coordinates,  $a^1$  and  $a^2$  remain the same. Let us consider a parton of the momentum  $k$  inside its parent hadron with the momentum  $P$ , and apply a large boost to the hadron. Then, in the light-front coordinate, with the  $+z$  axis in the direction of the hadron, the plus component of the parton's momentum,  $k^+$  is bigger than the other components of the momentum. The fractional momentum of the parton, a boost invariant

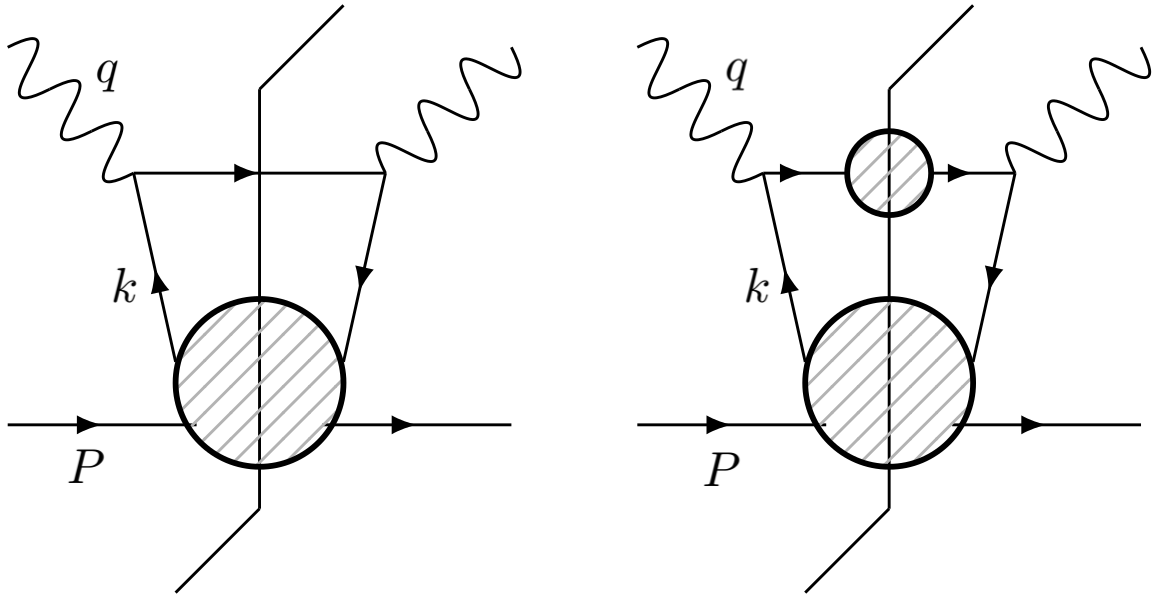


FIG. 2.1: The handbag diagram (left), the parton model in the field theory for the quark distribution (right).

quantity, is defined by  $x = k^+/P^+$

The parton model asserts that the inclusive DIS cross section should be approximated as the incoherent scattering of the leptons on the quasi-free partons. For a large momentum transfer, the incoming and outgoing partons can be approximated as massless free particles and the transverse momentum of the incoming parton can be neglected. The outgoing parton has high energy and can be approximated as a free particle. Though the strong interaction is neglected, the lowest-order electromagnetic interaction is taken into account.

Let us assume that the hadron consists of some number of partons and the fractional plus momenta are  $x_1, x_2, \dots$ , which sums to unity:  $\sum x_i = 1$ . In the parton model, it is postulated that there is a number distribution of the partons  $j$ , in the hadron  $h$ ,  $f_{j/h}(x)$  such that  $f_{j/h}(x) dx$  is the expectation of the number of the partons of flavor  $j$  with the fractional momentum  $x$  to  $x + dx$ . This  $f_{j/h}(x)$  is the parton density or distribution function of the parton  $j$  in the hadron  $h$ .

When the struck parton scatters off the virtual photon which is coming from the lep-

ton, the struck parton goes into the final state, undergoing the hadronization interactions which convert it to observable hadrons. The parton model makes the assumption that the transverse distribution of the hadrons under fragmentation is small, and that the essential physics is described by the partonic degrees of freedom. The struck parton momentum,  $k$  has a large plus component, and relatively small minus and transverse components as the calculation is done in the Breit frame. The final state interactions rearrange the content of the final state but do not greatly affect the probability that scattering has occurred. As a result, the final state interactions cancel to a first approximation in the inclusive cross section. Parton scattering in DIS after the cancellation of the hadronization and the final state interactions of the partons can be represented by the handbag diagram in Figure 2.1 (left diagram). Let  $d\sigma_{lj}^{partonic}$  be the differential cross section for the lepton-parton scattering. According to the parton model, for multiple flavors of partons involved in the process, the inclusive DIS cross section is

$$d\sigma = \sum_j \int dx f_{j/h}(x) d\sigma_{lj}^{partonic}. \quad (2.3)$$

This formula relates the cross section of a hadronic target to the cross section of a calculable partonic one. Now, the Lorentz-invariant inclusive DIS cross section can be written as

$$\frac{\pi e^4}{2s} \sum_X \delta^{(4)}(p_X - P - q) \left| \langle l' | j_\lambda^{lept} | l \rangle \frac{1}{q^2} \langle X, \text{out} | j^\lambda | P \rangle \right|^2 = \frac{2\alpha^2}{sQ^4} L_{\mu\nu} W^{\mu\nu}. \quad (2.4)$$

Here,  $s$  is the center-of-mass energy,  $\alpha$  is the fine-structure constant, the sum over  $X$  denotes the Lorentz-invariant sum and integral over all the hadronic final states  $|X\rangle$ ,  $j_\lambda^{lept}$  and  $j^\lambda$  are the currents for the leptonic and the hadronic fields respectively,  $L_{\mu\nu}$  is the leptonic tensor,  $W^{\mu\nu}$  is the hadronic tensor, virtuality of the photon is  $Q^2 = -q^2$ , and  $x$  is equal to the Bjorken variable,  $x_B = -\frac{q^2}{2P \cdot q}$  in the parton model approximation. Now, translating one of the currents from the origin to a location  $z$ , and using the completeness

relation of the hadronic final states,  $\sum_X |X\rangle \langle X| = 1$ , the hadronic tensor can be expressed as

$$W^{\mu\nu} = \frac{1}{4\pi} \int d^4z e^{iq \cdot z} \langle P, S | j^\mu(z) j^\nu(0) | P, S \rangle. \quad (2.5)$$

Here,  $S^\mu$  is the incoming hadron's spin vector. Eq. (2.5) holds only if the hadronic final states form a complete set, i.e. all the hadronic final states need to be considered in the theoretical calculation. This is the reason why the DIS experiment needs to be inclusive so that all possible outgoing hadronic states are taken into account.

Now, in the DIS for a large momentum transfer,  $Q^2$ , the plus component of the momentum is much bigger than the other components in both the struck parton and the incoming hadron. So, the squared center-of-mass energy can be written as:  $(xP + q)^2 \simeq 2xP \cdot q$  up to the power-law corrections, and the parton model approximation for  $W^{\mu\nu}$  is

$$W_{\text{PM}}^{\mu\nu} = \sum_j \int \frac{dx}{x} f_{j/h}(x) C_{j, \text{partonic}}^{\mu\nu}. \quad (2.6)$$

Here,  $C_{j, \text{partonic}}^{\mu\nu}$  is like  $W^{\mu\nu}$ , but is computed on a free massless parton  $j$  and momentum,  $k^\mu = (xP^+, 0, \mathbf{0}_T)$  in the light-front coordinate, neglecting all the interactions, and  $f_{j/h}(x)$  is the non-perturbative, long-distance parton distribution.

## 2.2 Successes and Limitations

A prediction of the parton model is that at a fixed Bjorken variable,  $x_B$ , and a large  $Q$ , the structure functions are independent of  $Q$ , the momentum transferred between the lepton and the hadron [48]. This is called Bjorken scaling. Experimentally, it was first observed in the well-known SLAC-MIT experiment on the DIS, carried out at the Stanford Linear Accelerator Center. It was found that for the proton, Bjorken scaling is

approximately true at moderate  $x$ , between 0.1 to 0.5. This region is relevant to a model where a substantial amount of the momentum of the proton is carried by three valence quarks, with a typical  $x$  around  $1/3$ .

The parton model does not require the partons to be completely free massless particles. In this model, the partons are approximately free and are used to estimate only the short-distance cross section. The parton model gives correct results for a super-renormalizable model theory without the gauge fields. When the gauge field is added to the theory, i.e. the interaction between quarks is considered, the parton model starts to break down. Bjorken scaling is also violated after allowing for strong interactions.

## 2.3 Field-theoretic Implementation

The parton model can be expressed in the language of field-theory. Using the light-front coordinates in the Breit frame,  $f_{j/h}(x)$  can be defined, for a DIS process as,

$$f_{j/h}(x) = \int \frac{dk^- d^2\mathbf{k}_T}{(2\pi)^4} \text{Tr} \frac{\gamma^+}{2} L_j(k, P). \quad (2.7)$$

Here,  $\mathbf{k}_T$  is the transverse momentum of the parton where the parton momentum can be expressed in light-front coordinate as  $k^\mu = (xP^+, k^-, \mathbf{k}_T)$ ,  $\gamma^+$  is the projection of the Dirac matrix trace in the “plus” direction,  $L_j(k, P)$  represents the lower subgraph in Figure 2.1 (right diagram), and the traces are taken over both the color and the Dirac indices. The normalization factor here, in the light-front quantization, allows us to interpret  $f_{j/h}(x)$  as the unpolarized parton distribution function or the number density of the quark of the flavor  $j$ . This PDF can be expressed as a matrix element of a bilocal operator,

$$f_{j/h}(x) = \int \frac{dz^-}{2\pi} e^{-ixP^+z^-} \left\langle P | \bar{\psi}_j(0, z^-, \mathbf{0}_T) \frac{\gamma^+}{2} \psi_j(0) | P \right\rangle_c. \quad (2.8)$$

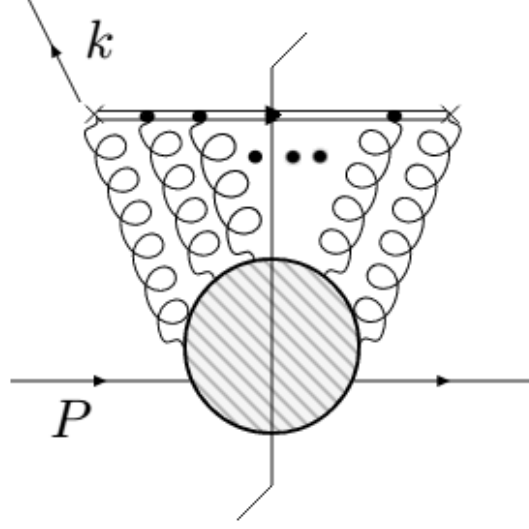


FIG. 2.2: The gauge invariant diagram for the unpolarized gluon distribution, where the double line is for the Wilson line.

Here, in the matrix element, only the contribution from the quark fields connected to the target state  $|P\rangle$  are to be included, which is indicated by the subscript  $c$ . The field,  $\psi_j(0)$  represents the extraction of a quark by the hard scattering, and,  $z^-$  is the Fourier conjugate to the opposite light-front component  $k^+$  in the momentum space. The hard scattering corresponds to the DIS on a free quark target, i.e., the process  $\gamma^* + q \rightarrow q$  with the quarks on-shell and of zero momentum.

To make the quark PDF gauge invariant, a Wilson line exactly along the lightlike line joining the fields needs to be included. So, the PDF becomes,

$$f_{(0)j/h}(x) = \int \frac{dz^-}{2\pi} e^{-ixP^+z^-} \left\langle P \left| \bar{\psi}_j^{(0)}(0, z^-, \mathbf{0}_T) W(z^-, 0) \frac{\gamma^+}{2} \psi_j^{(0)}(0) \right| P \right\rangle_c, \quad (2.9)$$

where,

$$W(z^-, 0) = \mathcal{P} \left\{ e^{-igo \int_0^{z^-} dy^- A_{(0)\alpha}^+(0, y^-, \mathbf{0}_T) t_\alpha} \right\}. \quad (2.10)$$

Here,  $W(z^-, 0)$  is the Wilson line between the fields, the symbol,  $\mathcal{P}$  means that the integral

is path ordered, and  $t_\alpha$  are the generating matrices for the gauge group in the fundamental representation. This is the bare quark PDF, as the fields used in the definition are bare fields. To get the full PDF, renormalization needs to be done.

The unpolarized gluon PDF can be defined by joining two field-strength tensors by a Wilson line.

$$f_{(0)g}(x) = \int \frac{dz^-}{2\pi x P^+} e^{-ixP^+z^-} \left\langle P \left| G_{(0)\alpha}^{+\rho}(0, z^-, \mathbf{0}_T) W_A(z^-, 0)_{\alpha\beta} G_{(0)\beta}^{+\rho}(0) \right| P \right\rangle_c. \quad (2.11)$$

Here,  $W_A$  denotes the Wilson line in the adjoint representation, and traces over the color indices are assumed. Like the quark PDF, the gluon PDF needs to be renormalized to obtain the correct and final definition of the PDFs. Figure 2.2 contains the gauge invariant diagram for the unpolarized gluon distribution. The double line is the Wilson line, and the short line at the top represents the flow of the external momentum at the parton density vertex.

# CHAPTER 3

## Lattice QCD

At high energy, the strong interaction has a weak coupling, which enables us to apply the perturbation theory successfully in the calculation. But, at low energy, as the coupling becomes strong, the perturbation theory breaks down, and the need for solving QCD non-perturbatively becomes apparent. To solve QCD non-perturbatively, Wilson [42] proposed to replace the spacetime with a lattice of regularly spaced points. A functional integral can be used over the fields on a lattice to approximate Euclidean Green's function. The fields exist either on the sites or on the links between the sites. The lattice sites are separated by the lattice spacing  $a$ . The lattice spacing might be different in the space dimensions and different in the temporal dimension, constituting the anisotropic lattice, or might be the same in all the four dimensions, constituting an isotropic lattice. Such a theory can have a well-defined strong coupling limit and opens up the possibility of computing the properties of a highly nontrivial quantum field theory numerically.

## 3.1 Clover Fermion Action

### 3.1.1 Naive Fermion Action

QCD is formulated by requiring invariance under the local rotations among the color indices of the quarks. To implement this rotation, an independent complex  $3 \times 3$  matrix is chosen at each spacetime point. These matrices belong to the special unitary group,  $SU(3)$ , meaning each of these matrices has the determinant equal to 1 and its conjugate transpose is equal to its inverse.

On the lattice, the same formulation is used. The lattice version of the free fermion action, without any gauge field, is

$$S_F^0[\psi, \bar{\psi}] = a^4 \sum_{n \in \Lambda} \bar{\psi}(n) \left( \sum_{\mu=1}^4 \gamma_\mu \frac{\psi(n + \hat{\mu}) - \psi(n - \hat{\mu})}{2a} + m_q \psi(n) \right). \quad (3.1)$$

Here,  $\Lambda$  is the set of all the lattice sites,  $n$  being a lattice site,  $\mu$  indicates the direction on the lattices,  $\psi(n)$  is the fermion field on the lattice, and  $m_q$  is a constant. Under a gauge transformation  $\Omega(n)$  in  $SU(3)$ , the quark and antiquark fields transform as:

$$\begin{aligned} \psi(n) &\rightarrow \psi'(n) = \Omega(n) \psi(n), \\ \bar{\psi}(n) &\rightarrow \bar{\psi}'(n) = \bar{\psi}(n) \Omega^\dagger(n). \end{aligned} \quad (3.2)$$

The lattice mass term is invariant under this transformation. The quark bilinears comprising the first term transform as,

$$\begin{aligned} \bar{\psi}(n) \psi(n + \hat{\mu}) &\rightarrow \bar{\psi}'(n) \psi'(n + \hat{\mu}) \\ &= \bar{\psi}(n) \Omega^\dagger(n) \Omega(n + \hat{\mu}) \psi(n + \hat{\mu}), \end{aligned} \quad (3.3)$$

which is not gauge invariant. To make this term gauge invariant, a field,  $U_\mu(n)$  with a

directional index  $\mu$  can be introduced as an element of the  $SU(3)$  group with the transformation defined as,

$$U_\mu(n) \rightarrow U'_\mu(n) = \Omega(n) U_\mu(n) \Omega^\dagger(n + \hat{\mu}). \quad (3.4)$$

This field,  $U_\mu(n)$ , can be related to the gauge field. A gauge-invariant term can be constructed from the quark fields and  $U_\mu(n)$ ,

$$\begin{aligned} \bar{\psi}'(n) U'_\mu(n) \psi'(n + \hat{\mu}) &= \bar{\psi}(n) \Omega^\dagger(n) U'_\mu(n) \Omega(n + \hat{\mu}) \psi(n + \hat{\mu}) \\ &= \bar{\psi}(n) U_\mu(n) \psi(n + \hat{\mu}). \end{aligned} \quad (3.5)$$

This new field  $U_\mu(n)$  is associated with the link of the lattice and referred to as link variable, living on the link which connects the sites,  $n$  and  $n + \hat{\mu}$ . The link variable,  $U_{-\mu}(n)$  points from  $n$  to  $n - \hat{\mu}$ , and defined as

$$U_{-\mu}(n) \equiv U_\mu^\dagger(n - \hat{\mu}). \quad (3.6)$$

The gauge transformation property of the link variable in the negative direction is,

$$U_{-\mu}(n) \rightarrow U'_{-\mu}(n) = \Omega(n) U_{-\mu}(n) \Omega^\dagger(n - \hat{\mu}). \quad (3.7)$$

Using the link variables, Eq. (3.1) can be generalized into the gauge-invariant naive fermion action

$$S_F[\psi, \bar{\psi}, U] = a^4 \sum_{n \in \Lambda} \bar{\psi}(n) \left( \sum_{\mu=1}^4 \gamma_\mu \frac{U_\mu(n) \psi(n + \hat{\mu}) - U_{-\mu}(n) \psi(n - \hat{\mu})}{2a} + m_q \psi(n) \right). \quad (3.8)$$

Now, Eq. (3.8) can be written in terms of the naive Dirac operator on the lattice,

$$S_F[\psi, \bar{\psi}, U] = a^4 \sum_{n, m \in \Lambda} \sum_{c, d, \alpha, \beta} \left( \bar{\psi}(n)_{\alpha c} D(n|m)_{\alpha c, \beta d} \psi(m)_{\beta d} \right), \quad (3.9)$$

where

$$D(n|m)_{\alpha c, \beta d} = \sum_{\mu=1}^4 (\gamma_{\mu})_{\alpha\beta} \frac{U_{\mu}(n)_{cd} \delta_{n+\hat{\mu}, m} - U_{-\mu}(n)_{cd} \delta_{n-\hat{\mu}, m}}{2a} + m_q \delta_{\alpha\beta} \delta_{cd} \delta_{nm} \Big). \quad (3.10)$$

### 3.1.2 Wilson Fermion

The inverse of the lattice Dirac operator is called the quark propagator. For simple cases like the free fermion, the quark propagator is better realized in momentum space. For the case of the free lattice fermion, where  $U_{\mu}(n) = \mathbb{1}$ , the Fourier transform of the lattice Dirac operator becomes

$$\begin{aligned} \tilde{D}(p|q) &= \frac{1}{|\Lambda|} \sum_{n \in \Lambda} e^{-i(p-q) \cdot na} \left( \sum_{\mu=1}^4 \gamma_{\mu} \frac{e^{iq_{\mu}a} - e^{-iq_{\mu}a}}{2a} + m_q \mathbb{1} \right) \\ &= \delta(p-q) \tilde{D}(p). \end{aligned} \quad (3.11)$$

Here,  $\tilde{D}(p)$  is

$$\tilde{D}(p) = m_q \mathbb{1} + \frac{i}{a} \sum_{\mu=1}^4 \gamma_{\mu} \sin(p_{\mu}a). \quad (3.12)$$

Thus, the momentum space quark propagator is

$$\tilde{D}(p)^{-1} = \frac{m_q \mathbb{1} - i a^{-1} \sum_{\mu} \gamma_{\mu} \sin(p_{\mu}a)}{m_q^2 + a^{-2} \sum_{\mu} \sin(p_{\mu}a)^2}. \quad (3.13)$$

In the case of a massless fermion,  $m_q = 0$ , the naive quark propagator has the physical pole at  $p = (0, 0, 0, 0)$ ,

$$\begin{aligned} \tilde{D}(p)^{-1} \Big|_{m_q=0} &= \frac{-i a^{-1} \sum_{\mu} \gamma_{\mu} \sin(p_{\mu}a)}{a^{-2} \sum_{\mu} \sin(p_{\mu}a)^2} \\ &\xrightarrow{a \rightarrow 0} \frac{-i \sum_{\mu} \gamma_{\mu} p_{\mu}}{p^2}. \end{aligned} \quad (3.14)$$

On the lattice, however, this propagator has an additional 15 poles. The poles are at

$$p = (0, 0, 0, 0), \left(\frac{\pi}{a}, 0, 0, 0\right), \left(0, \frac{\pi}{a}, 0, 0\right), \dots, \left(\frac{\pi}{a}, \frac{\pi}{a}, \frac{\pi}{a}, \frac{\pi}{a}\right). \quad (3.15)$$

The 15 unphysical poles are called doublers. Wilson suggested a way to remove these unwanted poles by adding an extra term to the momentum space Dirac operator,

$$\tilde{D}(p) = m_q \mathbb{1} + \frac{i}{a} \sum_{\mu=1}^4 \gamma_{\mu} \sin(p_{\mu} a) + \mathbb{1} \frac{1}{a} \sum_{\mu=1}^4 (1 - \cos(p_{\mu} a)). \quad (3.16)$$

The third term, the Wilson term, vanishes for  $p_{\mu} = 0$ , but provides an additional  $\frac{2}{a}$  contribution for  $p_{\mu} = \frac{\pi}{a}$ . This additional term combines with the mass term. In the continuum limit,  $a \rightarrow 0$ , the doublers become heavy and decouple from the theory. When the Wilson term is added, the unwanted poles are removed, and the only pole remaining is the physical one. The Dirac operator incorporating the Wilson term can be expressed as

$$D^{(f)}(n|m)_{\alpha c, \beta d} = \left(m_q^{(f)} + \frac{4}{a}\right) \delta_{\alpha\beta} \delta_{cd} \delta_{nm} - \frac{1}{2a} \sum_{\mu=\pm 1}^{\pm 4} (\mathbb{1} - \gamma_{\mu})_{\alpha\beta} U_{\mu}(n)_{cd} \delta_{n+\hat{\mu}, m}. \quad (3.17)$$

Here,  $\gamma_{-\mu} = -\gamma_{\mu}$ , where  $\mu = 1, 2, 3, 4$ , and the index  $f$  stands for the flavors of the quarks. The fermion action for QCD which reproduces the continuum action up to  $\mathcal{O}(a)$ , with  $N_f$  flavors becomes

$$S_F[\psi, \bar{\psi}, U] = \sum_{f=1}^{N_f} a^4 \sum_{n, m \in \Lambda} \bar{\psi}^{(f)}(n) D^{(f)}(n|m) \psi^{(f)}(m). \quad (3.18)$$

### 3.1.3 Wilson Gauge Action

The link variables can be related to the gauge fields of the continuum formulation. The gauge transformation property of the link variables in Eq. (3.4) is similar to the

transformation property of the gauge transporter in the continuum. The gauge transporter is the path ordered exponential integral of the gauge field,  $A_\mu$  along some curve,  $\mathcal{C}_{xy}$  connecting two points,  $x$  and  $y$ ,

$$G(x, y) = \mathcal{P} \exp \left( i \int_{\mathcal{C}_{xy}} A \cdot ds \right), \quad (3.19)$$

which transform under the gauge transformation as

$$G(x, y) \rightarrow \Omega(x) G(x, y) \Omega^\dagger(y). \quad (3.20)$$

This transformation property is as same as the one for the link variable. So, the link variable,  $U_\mu(n)$  can be interpreted as the lattice version of the gauge transporter and can be expressed in terms of the lattice gauge fields,  $A_\mu(n)$ ,

$$U_\mu(n) = e^{i a A_\mu(n)}. \quad (3.21)$$

The lattice gauge action can be constructed from the link variable, but the action needs to be gauge invariant. One way to achieve this is to take the product of the link variables in a closed loop on the lattice and take the trace. For the gluon action, it is sufficient to use the shortest, nontrivial closed loop on the lattice, known as the plaquette,  $U_{\mu,\nu}(n)$ , where

$$U_{\mu,\nu}(n) = U_\mu(n) U_\nu(n + \hat{\mu}) U_\mu^\dagger(n + \hat{\nu}) U_\nu^\dagger(n). \quad (3.22)$$

The graphical representation of the plaquette is shown in Figure 3.1. The Wilson gauge action [42] can be expressed as the sum over all the plaquettes on the lattice, with each plaquette counted with only one orientation,

$$S_G[U] = \frac{2}{g_s^2} \sum_{n \in \Lambda} \sum_{\mu < \nu} \text{Re tr}[\mathbf{1} - U_{\mu,\nu}(n)] \quad (3.23)$$

To check whether, in the  $a \rightarrow 0$  limit, this action approaches the continuum form,

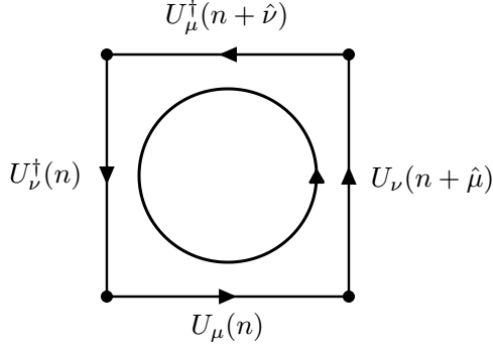


FIG. 3.1: The four link variables which build up the plaquette,  $U_{\mu,\nu}(n)$ .

$$S_G[A] = \frac{1}{2g_s^2} \int d^4x \operatorname{tr}[F_{\mu\nu}(x) F_{\mu\nu}(x)], \quad (3.24)$$

where  $F_{\mu\nu}(x)$  is the field strength tensor, the plaquette is expanded using the Baker-Campbell-Hausdorff formula and Taylor expansion, and it can be written as

$$\begin{aligned} U_{\mu,\nu} &= \exp(i a^2 (\partial_\mu A_\nu(n) - \partial_\nu A_\mu(n) + i[A_\mu(n), A_\nu(n)]) + \mathcal{O}(a^3)) \\ &= \exp(i a^2 F_{\mu\nu}(n) + \mathcal{O}(a^3)). \end{aligned} \quad (3.25)$$

Here,  $[A, B] \equiv AB - BA$ . Expanding the exponential, the Wilson gauge action can be expressed as

$$S_G[U] = \frac{a^4}{2g_s^2} \sum_{n \in \Lambda} \sum_{\mu, \nu} \operatorname{tr}[F_{\mu\nu}^2(n)] + \mathcal{O}(a^2). \quad (3.26)$$

In the limit  $a \rightarrow 0$  Eq. (3.26) gives Eq. (3.24) up to  $\mathcal{O}(a^2)$ .

### 3.1.4 Symanzik Improvement

In order to reduce the discretization effects, the lattice action needs to be modified. Correction terms with all the symmetries associated with the theory are identified using the continuum language. Discretized versions of these correction terms are added to the

lattice action with suitable coefficients to remove or reduce discretization uncertainties at a given order in  $a$ . This approach to improving the theory is known as the Symanzik improvement program [49, 50]. For the fermion action with Wilson's Dirac operator, the leading continuum correction term,  $L^{(1)}(y)$  can be written as a linear combination of the five possible dimension-5 operators,

$$\begin{aligned}
L_1^{(1)}(y) &= \bar{\psi}(y) \sigma_{\mu\nu} F_{\mu\nu}(y) \psi(y), \\
L_2^{(1)}(y) &= \bar{\psi}(y) \vec{D}_\mu(y) \vec{D}_\mu(y) \psi(y) + \bar{\psi}(y) \overleftarrow{D}_\mu(y) \overleftarrow{D}_\mu(y) \psi(y), \\
L_3^{(1)}(y) &= m_q \text{tr}[F_{\mu\nu}(y) F_{\mu\nu}(y)], \\
L_4^{(1)}(y) &= m_q \left( \bar{\psi}(y) \gamma_\mu \vec{D}_\mu(y) \psi(y) - \bar{\psi}(y) \gamma_\mu \overleftarrow{D}_\mu(y) \psi(y) \right), \\
L_5^{(1)}(y) &= m_q^2 \bar{\psi}(y) \psi(y).
\end{aligned} \tag{3.27}$$

Here,  $\sigma_{\mu\nu} \equiv [\gamma_\mu, \gamma_\nu]/2i$ , and  $D_\mu$  is the Dirac operator. Using the field equation  $(\gamma_\mu D_\mu + m_q) \psi = 0$ , the following relations between the operators can be derived,

$$\begin{aligned}
L_1^{(1)} - L_2^{(1)} + 2L_5^{(1)} &= 0, \\
L_4^{(1)} + 2L_5^{(1)} &= 0,
\end{aligned} \tag{3.28}$$

which can be used to eliminate the terms  $L_2^{(1)}(y)$  and  $L_4^{(1)}(y)$ . These relations hold beyond tree level [51]. Terms of the form  $L_3^{(1)}(y)$  and  $L_5^{(1)}(y)$  already exist in the action, and therefore correspond to a redefinition of their coefficients in the action. So, the Pauli term,  $L_1^{(1)}(y)$  alone gives the  $\mathcal{O}(a)$  improvement of the Wilson lattice action, the improved action being [52]

$$S_I = S_{\text{Wilson}} + c_{\text{SW}} a^5 \sum_{n \in \Lambda} \sum_{\mu < \nu} \bar{\psi}(n) \frac{1}{2} \sigma_{\mu\nu} \hat{F}_{\mu\nu}(n) \psi(n). \tag{3.29}$$

The real coefficient  $c_{\text{SW}}$  is referred to as the Sheikholeslami-Wohlert coefficient, which is determined non-perturbatively for the exact cancellation of the discretization effects. Here,

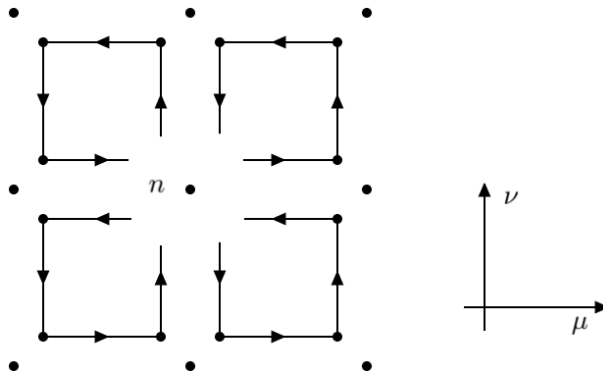


FIG. 3.2: Graphical representation of the sum,  $Q_{\mu\nu}(n)$  of the plaquettes in the  $\mu - \nu$  plane.

$\hat{F}_{\mu\nu}(n)$  is the lattice form of the field strength tensor. One choice of calculating  $\hat{F}_{\mu\nu}(n)$  is to take the combination of the plaquettes so that,

$$\hat{F}_{\mu\nu}(n) = \frac{-i}{8a^2} (Q_{\mu\nu}(n) - Q_{\nu\mu}(n)) , \quad (3.30)$$

where  $Q_{\mu\nu}(n)$  is the sum of the plaquettes  $U_{\mu,\nu}(n)$  in the  $\mu - \nu$  plane such that all the positive and negative combinations of  $\mu$  and  $\nu$  are taken. The graphical representation of  $Q_{\mu\nu}(n)$  is shown in Figure 3.2.

$$Q_{\mu\nu}(n) = U_{\mu,\nu}(n) + U_{\nu,-\mu}(n) + U_{-\mu,-\nu}(n) + U_{-\nu,\mu}(n) . \quad (3.31)$$

On the lattice, this structure has the shape of a clover leaf. This is why the last term in Eq. (3.29) is sometimes referred to as the clover term.

## 3.2 Importance Sampling and Lattice QCD

In the lattice gauge theory, as the spacetime is discretized, the Euclidean  $SO(4)$  rotational symmetry is violated, but the gauge invariance is kept in place. In the continuum limit where the lattice spacing  $a \rightarrow 0$  limit is taken, the four-dimensional Euclidean symmetry is recovered. In lattice QCD, the nonzero lattice spacing  $a$ , acts as a UV regulator.

As the calculation on the lattice takes place in the Euclidean space, the Feynman path-integral is Wick rotated, setting  $t_M = -it_E$ , where  $t_M$  is time in the Minkowskian space and  $t_E$  is time in the Euclidean space.

For a pure  $SU(3)$  gauge theory, the vacuum expectation value of an observable,  $\mathcal{O}$  on the lattice is formally given by the functional integral

$$\langle \mathcal{O} \rangle = \frac{1}{Z} \int \mathcal{D}[U] e^{-S_G[U]} \mathcal{O}[U], \quad (3.32)$$

where  $Z = \int \mathcal{D}[U] e^{-S_G[U]}$ ,  $S_G[U]$  is the pure  $SU(3)$  gauge action, and  $U$  is the gauge configuration on the lattice.

If the gauge configurations are chosen randomly, a precise result can not be expected in a reasonable calculation time. Instead, importance sampling is implemented, where each gauge configuration gets a weight of  $e^{-S_G}$ . In Euclidean space, the action,  $S_G$  becomes real, so the weight factor can be treated as a probability distribution. This technique is known as the importance sampling Monte Carlo method. Now, Eq. (3.32) can be rewritten as

$$\langle \mathcal{O} \rangle = \frac{\int \mathcal{D}[U] e^{-S_G[U]} \mathcal{O}[U]}{\int \mathcal{D}[U] e^{-S_G[U]}}. \quad (3.33)$$

If the gauge configurations are randomly sampled with the normalized probability distribution, also known as the Gibbs measure [53],

$$dP(U) = \frac{e^{-S_G[U]} \mathcal{D}[U]}{\int \mathcal{D}[U] e^{-S_G[U]}}, \quad (3.34)$$

the expectation value of the observable,  $\mathcal{O}$  is approximated in the importance sampling Monte Carlo integration by an average over  $N_u$  number of gauge configurations,

$$\langle \mathcal{O} \rangle = \lim_{N_u \rightarrow \infty} \frac{1}{N_u} \sum_{u=1}^{N_u} \mathcal{O}[U_u]. \quad (3.35)$$

The statistical error of the result will be proportional to  $1/\sqrt{N_u}$  and the exact value will be obtained for  $N_u \rightarrow \infty$ , thus providing complete control over the statistical error.

In order to generate the gauge configurations  $U_u$  following Eq. (3.34), the homogeneous Markov process is used. One can start from some arbitrary configuration and then construct a stochastic sequence of configurations that eventually follows an equilibrium distribution,  $P(U)$ , i.e.

$$U_0 \longrightarrow U_1 \longrightarrow U_2 \longrightarrow \dots \quad (3.36)$$

In this Markov chain configuration,  $U_u$  is generated subsequently. The index  $n$  labels the configurations in the order they appear in the chain; it is often referred to as the computer time. The change of a gauge configuration to a new one is called an update or a Monte Carlo step.

A Markov process is characterized by a conditional transition probability,  $T(U_u|U_{u-1})$  to get  $U_u$  if starting from  $U_{u-1}$ . This probability depends only on the configuration  $U_u$  and the previous configuration  $U_{u-1}$  but not on the index  $u$ . The transition probability follows the relations,

$$0 \leq T(U_u|U_{u-1}) \leq 1, \quad \sum_{U_u} T(U_u|U_{u-1}) = 1. \quad (3.37)$$

The inequality tells the range of a probability. The sum states that the total probability of jumping from a configuration  $U_{u-1}$  to any target configuration  $U_u$  is equal to 1. There is another important restriction for  $T(U_u|U_{u-1})$ . Once the system is in equilibrium, the Markov process cannot have sinks or sources of probability. Thus the probability to hop into a configuration  $U_u$  at the step  $U_{u-1} \longrightarrow U_u$  has to be equal to the probability for

hopping out of  $U_u$  at this step. The corresponding detailed balance equation reads as

$$\sum_{U_{u-1}} T(U_u|U_{u-1})P(U_{u-1}) = \sum_{U_{u-1}} T(U_{u-1}|U_u)P(U_u). \quad (3.38)$$

Here,  $P(U_u)$  is the probability of the system being in the configuration,  $U_u$ . Now, using the normalization property of Eq. (3.37) it is found that,

$$\sum_{U_{u-1}} T(U_u|U_{u-1})P(U_{u-1}) = P(U_u), \quad (3.39)$$

indicating that the equilibrium distribution  $P(U_{u-1})$  is a fixed point of the Markov process. Once the equilibrium distribution is obtained, the system stays there upon applying  $T$ .

To obtain the correct results, the Markov chain must be able to access all the configurations. If the transition matrix  $T(U_u|U_{u-1})$  is strictly positive for all pairs,  $U_{u-1}$  and  $U_u$ , then the process is aperiodic and every configuration can be eventually reached. This property is called strong ergodicity. This means that the entire phase space of the gauge configurations will eventually be sampled and by increasing the number of configurations, the expectation value of the calculated observable will systemically improve. In practice, the calculation of the observables according to Eq. (3.35) starts after a sufficient number of equilibrating Monte Carlo steps, when the distribution of the considered configurations is already close enough to the equilibrium distribution.

There is a sufficient condition for the solution of the balance equation Eq. (3.38),

$$T(U_u|U_{u-1})P(U_{u-1}) = T(U_{u-1}|U_u)P(U_u). \quad (3.40)$$

This sufficient condition is known as the detailed balance condition. Although other solutions are known, most algorithms use the detailed balance condition. One of the common implementations of the Monte Carlo algorithm with the detailed balance condition is the

Metropolis algorithm.

In the Metropolis algorithm, to advance the Markov chain from a configuration,  $U_{u-1}$  to a new configuration,  $U_u$ , first a candidate configuration,  $U_u$  is chosen according to a priori selection probability  $T_0(U_u|U_{u-1})$ . Then the candidate configuration is accepted as the new configuration with the acceptance probability,

$$T_A(U_u|U_{u-1}) = \min \left( 1, \frac{T_0(U_{u-1}|U_u) P(U_u)}{T_0(U_u|U_{u-1}) P(U_{u-1})} \right). \quad (3.41)$$

Here,  $P(U_u) \propto e^{-S_G[U_u]}$ . If the suggested change is not accepted, the unchanged configuration is considered again in the Markov chain, another candidate configuration is chosen again and the procedure is repeated. It is straightforward to see that the total transition probability  $T = T_0 T_A$  fulfills the detailed balance condition due to the positivity of all factors and the symmetry of the min operation. When fermions are included in the calculation, the action is modified by including the fermionic determinants in the distribution weight for the gauge configurations, but the basic principle remains the same.

For a proper comparison with quantities from the experimental results, a continuum limit  $a \rightarrow 0$ , and an infinite volume limit  $L \rightarrow \infty$ , are necessary. In practice, one cannot perform a calculation in these extreme limits, instead, extrapolations are made. The error from these extrapolations can be systematically improved by increasing the computational cost and lowering the value of  $a$ , and raising the value of  $L$ . Unlike the other methods for calculating the QCD observables, lattice QCD is the only known method with this sort of systematically controllable error, making it a vital tool for studying the strong interactions.

### 3.3 PDF on the Lattice

Lattice QCD has been very successful in calculating the bulk hadronic properties such as the masses and the charges [54]. Determination of the position and the momentum distributions of the partons inside a hadron is of particular theoretical interest to directly explore the non-perturbative sector of QCD from first principles. Since the non-perturbative information about hadron structure is encoded in the PDFs, they are natural candidates for a lattice QCD calculation.

There have been several proposals for the extraction of  $x$ -dependent hadron structure from lattice QCD calculations, such as the path-integral formulation of the deep-inelastic scattering hadronic tensor [55], the operator product expansion [56], quasi-PDFs [57, 58], pseudo-PDFs [59], and lattice cross-sections [60, 61]. PDFs can be calculated from the matrix elements of bilocal operators separated along the light-cone. As lattice QCD is formulated on the Euclidean space, it can have only one point on the light-cone, making the PDF impossible to evaluate directly. However, lattice calculation can be performed for small  $z^2$ , and then some method can be implemented to reach the  $z^2 = 0$  limit.

The starting idea is to take the equal-time, spacelike interval  $z$ , which was put forward by [62] and emphasized by [57], introducing the quasi-PDF framework that initiated numerous lattice studies on the PDFs. This method calculates the matrix elements associated with equal-time and purely spacelike field separations with hadron states at nonzero momentum,  $p_z$ . The corresponding quasi-PDFs can be matched to the light-cone PDFs when the hadron momentum is large, by applying the Large Momentum Effective Theory (LaMET) [58]. For recent reviews, the readers are referred to Refs [63, 64] and the references therein.

The matrix element relevant to the PDF can be written as a function of the Ioffe-time [65]  $(p \cdot z) \equiv -\nu$ , which is a dimensionless quantity that describes the amount

of time the DIS probe interacts with the hadron, in units of the inverse hadron mass. This matrix element,  $\mathcal{M}(\nu, z^2)$  is known as the Ioffe-time pseudo-distribution [59], which is a generalization of the light-cone Ioffe-time distribution [66] (ITD),  $\mathcal{I}(\nu, \mu^2)$  onto the spacelike intervals  $z^2$ .

Now,  $\mathcal{I}(\nu, \mu^2)$  is the Fourier transform of the light-cone PDF  $f(x, \mu^2)$ , with the Ioffe-time,  $\nu$  being the Fourier-conjugate of the parton momentum fraction variable,  $x$ .

$$\mathcal{I}(\nu, \mu^2) = \int_{-1}^1 dx e^{ix\nu} f(x, \mu^2). \quad (3.42)$$

Similarly, the Fourier transform in  $\nu$  of the pseudo-ITD  $\mathcal{M}(\nu, z^2)$  gives the pseudo-PDF,  $\mathcal{P}(x, z^2)$  [59, 67, 68, 69, 70].

$$\mathcal{P}(x, z^2) = \frac{1}{2\pi} \int_{-\infty}^{\infty} d\nu e^{-ix\nu} \mathcal{M}(\nu, z^2). \quad (3.43)$$

As the pseudo-ITD is a Lorentz-invariant function, the pseudo-PDF is also Lorentz-invariant, the variable,  $x$ , being Lorentz-invariant. As  $x$  does not depend on a specific frame choice, an infinite momentum frame is not needed to define  $x$ . The pseudo-PDF,  $\mathcal{P}(x, z^2)$  is the most natural generalization of the light-cone PDF,  $f(x, \mu^2)$  onto spacelike intervals. For  $f(x, \mu^2)$ , the usual interpretation of the scale  $\mu$  is that  $\frac{1}{\mu}$  characterizes the distances at which the hadron structure is probed. For nonzero spacelike separation, the scale  $z$  in  $\mathcal{P}(x, z^2)$  is literally the distance at which the hadron structure is probed.

The  $z$ -dependence of the pseudo-ITD  $\mathcal{M}(\nu, z^2)$  comes from both the product  $\nu$  and  $z^2$ . The  $\nu$ -dependence of  $\mathcal{M}(\nu, z^2)$  translates into the  $x$ -dependence of  $\mathcal{P}(x, z^2)$ . The remaining  $z^2$ -dependence of  $\mathcal{M}(\nu, z^2)$  specifies how the  $x$ -shape of  $\mathcal{P}(x, z^2)$  changes with the change of the probing distance,  $z$ . The dependence on the probing distance may be interpreted in terms of the distribution of the parton's transverse momentum [59].

As  $\nu$  and  $z^2$  are Lorentz invariants, the pseudo-ITD  $\mathcal{M}(\nu, z^2)$  is the same univer-

sal function of them, no matter how  $\nu$  and  $z^2$  were obtained from specific choices of  $z$  and  $p$ . In particular, taking  $z$  on the light-front,  $z = \{z_+ = 0, z_-, z_\perp\}$ , and a longitudinal  $p = \{p_+, p_-, 0_\perp\}$  gives  $\mathcal{M}(\nu, z_\perp^2)$ , where  $\nu = -(p_+ z_-)$ . Here, the  $\nu$ -dependence of  $\mathcal{M}(\nu, z_\perp^2)$  determines the  $x$ -distribution of the longitudinal “plus”-component of the parton momentum, while its  $z_\perp^2$ -dependence determines the distribution of its transverse momentum  $k_\perp$ . So, two different physical phenomena are associated with the two arguments of the pseudo-ITD,  $\mathcal{M}(\nu, z^2)$ .

In renormalizable theories, the pseudo-PDF has a logarithmic divergence at small  $z^2$  which corresponds to the Dokshitzer–Gribov–Lipatov–Altarelli–Parisi (DGLAP) evolution of the PDF. The pseudo-PDF and the pseudo-ITD can be factorized into the PDF and perturbatively calculable kernels, similar to the factorization framework for experimental cross-sections. There have been a number of lattice calculations implementing the pseudo-PDF method [71, 72, 73, 74, 75, 76]. There has also been another promising approach based on the factorization in the coordinate space and the analysis of the Ioffe-time dependence. This approach, the lattice cross sections [60, 61] has also been implemented on the lattice [77, 78] successfully.

There have been significant achievements in lattice QCD calculations of  $x$ -dependent hadron structure: the nucleon valence quark distribution using pseudo-PDFs [79], the calculation of the pion valence distribution using the lattice cross section, quasi-PDF and pseudo-PDF frameworks [77, 78, 80, 81, 82], the kaon PDF calculation using the quasi-PDF formalism [83], the nucleon unpolarized and helicity distributions within the quasi-PDF formalism [84, 85, 86], the unpolarized and helicity GPD calculation of the proton [87], and a quasi-TMD calculation in the pion [88]. However, there are fewer lattice calculations of gluon distribution functions than of quark distributions. Lattice calculations include the gluon momentum fraction [89, 90], the gluon contribution to the nucleon spin [91], gluon gravitational form factors of the nucleon and the pion [92]. Recently, there have

been attempts to calculate gluon PDFs in the nucleon and the pion [93, 94, 95].

The calculation of the gluon PDF presented here follows the reduced pseudo-ITD approach, where the matrix elements of the operators with a spacelike separation are calculated, and the multiplicative UV renormalizing factors are canceled by taking a double ratio [73]. This double ratio, also known as reduced pseudo-ITD, removes the Wilson-line related divergences, as well as various other systematic errors. To determine the gluon parton distribution from the reduced pseudo-ITD, the QCD short distance factorization (SDF) is used where the small  $z$  separation limit is taken.

# CHAPTER 4

## Computational Details

To extract information from a system composed of hadrons,  $n$ -point correlators need to be calculated. The simplest  $n$ -point correlator is the two-point function which is constructed by applying the creation operator at the source time slice and the annihilation operator at the sink time slice. Operators built directly from the fields in the lattice lagrangian have significant overlap with a large tower of states, and extracting information about any particular state of the spectrum is difficult. The way to solve this problem is to build the operators from smeared fields, where some linear operator is applied first to the quark degree of freedom on the appropriate time slice before the creation operator is formed. A good smearing method should have the properties of being numerically accessible, doing a good job of projecting onto the lowest energy states, and enabling easy evaluation of the correlator functions involving a broad set of operators. Smearing should preserve as many symmetries of the system as possible while effectively removing the presence of the short-range modes, which make an insignificant contribution to the low-energy correlation function.

## 4.1 Distillation

Distillation [96] is a quark-smearing technique that can be described as a low-rank approximation to the Jacobi smearing kernel [97]. The Jacobi smearing algorithm is a gauge-covariant smearing scheme where a lattice approximation to the three-dimensional gauge-covariant Laplacian is constructed and applied iteratively to the field. This acts as a long-wavelength filter on the modes constituting the quark field.

In the Jacobi smearing method, the lattice Laplacian is identified as the simplest representation of the second-order three-dimensional differential operator,

$$-\nabla_{xy}^2(t) = 6\delta_{xy} - \sum_{j=1}^3 \left( \tilde{U}_j(x, t) \delta_{x+\hat{j}, y} + \tilde{U}_j^\dagger(x - \hat{j}, t) \delta_{x-\hat{j}, y} \right). \quad (4.1)$$

where  $\tilde{U}$  is constructed from a covariant gauge-field-smearing algorithm [98]. From the lattice Laplacian, the Jacobi smearing kernel [97] can be written as

$$J_{\sigma, n_\sigma}(t) = \left( 1 + \frac{\sigma \nabla^2(t)}{n_\sigma} \right)^{n_\sigma}. \quad (4.2)$$

For large  $n_\sigma$ , this approximates the exponential of  $\sigma \nabla^2$ ,

$$\lim_{n_\sigma \rightarrow \infty} J_{\sigma, n_\sigma}(t) = \exp(\sigma \nabla^2(t)). \quad (4.3)$$

This means that the higher eigenmodes are exponentially suppressed, indicating that the majority of the contribution is coming from only a small number of the lowest-magnitude modes. As a result, the smearing kernel can be approximated by forming an eigenvector representation, truncated to the lowest-magnitude modes. The distillation [96] technique is formulated using these lowest modes of the Jacobi kernel. The distillation operator at

time slice,  $t$  is constructed as

$$\square_{xy}(t) = \sum_{k=1}^{N_D} \nu_x^{(k)}(t) \nu_y^{(k)\dagger}(t) \equiv V_D(t) V_D^\dagger(t), \quad (4.4)$$

where  $V_D(t)$  is a  $(N_c \times N_x \times N_y \times N_z) \times N_D$  matrix, with  $N_c$  the dimension of the color space and  $N_x, N_y, N_z$  the extents of the lattice in three spatial directions. The  $k^{\text{th}}$  column of  $V_D(t)$ ,  $\nu_x^{(k)}(t)$  is the  $k^{\text{th}}$  eigenvector of  $\nabla^2$ , evaluated on the background of the spatial gauge fields at time slice  $t$ , once the eigenvectors have been sorted by the ascending order of the eigenvalues, and  $N_D$  is the dimension of the distillation space.

The distillation operator is applied onto each quark field to achieve the smearing. The smeared annihilation operator for baryons with isospin- $\frac{1}{2}$  can be written as

$$\mathcal{O}(t) = \epsilon^{abc} S_{\alpha\beta\gamma} (\Gamma_1 \square d)_\alpha^a (\Gamma_2 \square u)_\beta^b (\Gamma_3 \square u)_\gamma^c (t). \quad (4.5)$$

Here, the color indices,  $a, b, c$  of the quark fields acted upon by the displacement operators,  $\Gamma_1, \Gamma_2, \Gamma_3$  respectively, are contracted with the antisymmetric tensor, and repeated spin indices,  $\alpha, \beta, \gamma$  are summed. After integrating over the quark fields, the two-point correlator becomes [96]

$$\begin{aligned} \langle \mathcal{O}_i(t_m) \bar{\mathcal{O}}_j(t_n) \rangle &= \Phi_{i,\alpha\beta\gamma}^{(pqr)}(t_m) \times \left[ \mathfrak{P}_{\alpha\bar{\alpha}}^{p\bar{p}}(t_m, t_n) \mathfrak{P}_{\beta\bar{\beta}}^{q\bar{q}}(t_m, t_n) \mathfrak{P}_{\gamma\bar{\gamma}}^{r\bar{r}}(t_m, t_n) \right. \\ &\quad \left. - \mathfrak{P}_{\alpha\bar{\alpha}}^{p\bar{p}}(t_m, t_n) \mathfrak{P}_{\beta\bar{\gamma}}^{q\bar{r}}(t_m, t_n) \mathfrak{P}_{\gamma\bar{\beta}}^{r\bar{q}}(t_m, t_n) \right] \times \Phi_{j,\bar{\alpha}\bar{\beta}\bar{\gamma}}^{(\bar{p}\bar{q}\bar{r})^*}(t_n), \end{aligned} \quad (4.6)$$

where

$$\Phi_{i,\alpha\beta\gamma}^{(pqr)}(t) = \epsilon^{abc} S_{i,\alpha\beta\gamma} \left( \Gamma_{1i} \nu^{(p)} \right)^a \left( \Gamma_{2i} \nu^{(q)} \right)^b \left( \Gamma_{3i} \nu^{(r)} \right)^c (t), \quad (4.7)$$

and

$$\mathfrak{P}_{\alpha\bar{\alpha}}^{p\bar{p}}(t_m, t_n) = \nu^{(p)\dagger}(t_m) D_{\alpha\bar{\alpha}}^{-1}(t_m, t_n) \nu^{(\bar{p})}(t_n). \quad (4.8)$$

Here,  $\Phi(t)$  and  $\mathfrak{P}(t_m, t_n)$  are referred to as *elementals* and *perambulators*, respectively;  $D$  is the lattice Dirac operator;  $\alpha, \bar{\alpha}, \beta, \bar{\beta}, \gamma, \bar{\gamma}$  are the spin indices. The  $\Phi_i(t)$  encodes the structure of the interpolating operator and has a well-defined momentum, while  $\mathfrak{P}(t_m, t_n)$  encodes the propagation of the quarks, and does not have any explicit momentum projection. Elementals can be decomposed into terms that act only within the coordinate and color space, like  $\Gamma$ , and those that act only within the spin space, like  $S_{\alpha\beta\gamma}$ .

Distillation is adopted for two reasons. First, the computationally demanding parallel transporters of the theory, the perambulators, depend only on the gauge field, and not on the interpolators. Therefore, the perambulators are calculated on an ensemble of gauge fields once, and then they are reused for an extended basis of interpolators, thus reducing the computational cost to a great extent. This extended basis of interpolators is the key to performing a successful summed generalized eigenvalue problem (sGEVP) analysis [99], enabling one to attain a clear signal for the ground state nucleon.

Second, distillation admits a momentum projection both at the source interpolating operator and at the sink interpolating operator, in contrast to the more usually adopted methods. Thus for the computation of the gluonic three-point functions, momentum projection is imposed at all three time slices, ensuring the most complete possible sampling of the lattice. Moreover, the low-lying spectra of the nucleon and the delta can be faithfully captured with a relatively small number of distillation eigenvectors [43], thus lowering the cost of the calculation further. The expectation is that  $N_D$  should scale as the physical volume, and the cost of computing the corresponding correlation functions scales as  $N_D^4$  for the case of baryons. In this calculation,  $N_D = 64$  eigenvectors are employed. The efficacy of distillation for the calculation of nucleon charges was demonstrated in Ref. [100], and subsequently extended to the case of the nucleon in motion [101]. Recently, the unpolarized gluon PDF [44] and quark PDF [102] in the nucleon have been computed using the same ensemble within the distillation framework.

## 4.2 Momentum Smearing

To access a wide range of Ioffe-times for the calculation of the gluon PDF, the hadron must be boosted to many spatial momenta. On the lattice, the spatial momentum is discretized and expressed as

$$p = \frac{2\pi l}{aL}. \quad (4.9)$$

Here,  $L$  is the spatial extent of the lattice, and  $l$  is an integer number. Now, at the higher momenta, the interpolating operators do not have significant overlap onto the lowest-lying states in motion. As a result, the higher-momenta calculations accumulate large statistical uncertainties. To solve this problem, the overlaps of the interpolators onto the lowest-lying states in motion need to be increased, which is done by applying momentum smearing [103]. In the gluon PDF calculation, the procedure introduced in [101] is followed. A phase is added to the distillation eigenvectors for the higher momenta preserving the translational invariance, which is essential for the projection onto the states of definite momenta. The “phased” distillation eigenvector becomes,

$$\tilde{\nu}_x^{(k)}(\vec{z}, t) = e^{i\vec{\zeta} \cdot \vec{z}} \nu_x^{(k)}(\vec{z}, t). \quad (4.10)$$

To perform the calculation at higher lattice momenta, it is sufficient to modify the distillation eigenvectors according to Eq. (4.10) which calculates phased distillation eigenvectors. The perambulators and the elementals need to be recalculated with these phased distillation eigenvectors.

### 4.3 Lattice Details

The lattice calculations are performed on isotropic ensembles with  $(2 + 1)$  dynamical flavors of the clover Wilson fermions with the stout-link smearing [98] of the gauge fields and a tree-level tadpole-improved Symanzik gauge action, generated by the JLab/W&M collaboration [104]. The unpolarized gluon PDF calculation is done on the ensemble *a094m358* with the approximate lattice spacing,  $a \sim 0.094$  fm and pion mass,  $M_\pi \sim 358$  MeV. The baryon spectra calculation is performed on the same *a094m358* ensemble, along with another ensemble, *a094m278*, with the same lattice spacing,  $a \sim 0.094$  fm with pion mass,  $M_\pi \sim 278$  MeV. These ensembles were previously used in other lattice calculations such as [102, 75, 101, 77]. The Rational Hybrid Monte Carlo (RHMC) algorithm [105] is used to carry out the updates on both the ensembles. One iteration of four-dimensional stout-smearing with the weight,  $\rho = 0.125$  for the staples is used in the fermion action. After stout-smearing, the tadpole-improved tree-level Sheikholeslami-Wohlert coefficient,  $c_{SW}$  becomes very close to the non-perturbative value. This is confirmed using the Schrodinger functional method for determining the clover coefficient non-perturbatively [104]. For both the ensembles, the tuning of the strange quark mass is done by first setting the quantity,  $(2 M_{K^+}^2 - M_{\pi^0}^2)/M_{\Omega^-}^2$  equal to its physical value 0.1678. This quantity is independent of the light quark masses to the lowest order in  $\chi$ PT, depending only on the strange quark mass [106]. So, it can be tuned in the  $SU(3)$  symmetric limit. The resulting value of the strange quark mass is then kept fixed as the light quark masses are decreased in the  $(2 + 1)$  flavor theory to their physical values.

For the ensemble *a094m358*, the calculation is performed over 349 gauge configurations, and for *a094m278*, over 259 gauge configurations. For both the ensembles, each configuration is separated from the next configuration by 10 Hybrid Monte Carlo (HMC) trajectories. The two light quark flavors,  $u$  and  $d$  are taken to be degenerate and the

lattice spacing is determined using the  $w_0$  scale [107]. The parameters of the ensembles are summarized in Table 4.1.

To achieve the best possible sampling of the lattice, calculations are performed by considering each of the 64 time slices as the temporal sources of the relevant two-point correlators on each lattice, and on each gauge configuration, and the average is taken over the temporal sources. The distillation eigenvector space is set to  $N_D = 64$  for both of the ensembles.

In the gluon PDF calculation, application of the phasing is needed on the relevant lattice for  $p$ , where  $l > 3$  in Eq. (4.9). Choosing

$$\vec{\zeta} = 2 \cdot \frac{2\pi}{L} \hat{z}, \quad (4.11)$$

gives the momentum smearing needed for boosts up to  $p = 6 \times \frac{2\pi}{aL}$ .

ID	$a$ (fm)	$M_\pi$ (MeV)	$L^3 \times N_t$	$N_{\text{cfg}}$	$N_{\text{srcs}}$
<i>a094m358</i>	0.094(1)	358(3)	$32^3 \times 64$	349	64
<i>a094m278</i>	0.094(1)	278(4)	$32^3 \times 64$	259	64

TABLE 4.1: The parameters of the ensembles where the scale is obtained using the  $w_0$  scale [107],  $N_{\text{cfg}}$  is the number of the gauge configurations, and  $N_{\text{srcs}}$  is the number of the temporal sources.

# CHAPTER 5

## Positive-parity Nucleon and Delta Spectra

The starting point for a study of the excited state spectrum from lattice QCD is the extraction of the discrete, low-lying energy levels on the Euclidean lattice where lattice QCD is formulated. The most straightforward, albeit naïve, approach is to identify those energy levels with the single- or multi-particle states in the spectrum. Whilst the resulting energy spectrum should be independent of the basis of the interpolating operators employed, it has the potential instead to be highly sensitive to that basis. Thus the first attempts to compute the spectrum employed the baryon interpolating operators with a straightforward three-quark structure, mirroring the valence structure [108, 109, 110, 111, 112, 113, 114, 115, 116, 117]. The focus of this calculation is on the higher states in the spectrum. Considerable insight into the excited baryon spectrum of QCD has been obtained, most notably, the extracted spectrum is found to be at least as rich as the quark model predicts. Indeed, the ordering of the states was found to be in agreement with the predictions of the constituent quark model. However, such a model fails to find the low-

mass Roper seen in the experiments. The aim of the baryon spectra calculations herein is to investigate whether the counting of states and the suggestion of hybrid baryon states is robust by performing calculations of the low-lying positive-parity nucleon and delta spectra with gauge and fermion actions, lattice spacings and pion masses different than those of Ref. [1].

## 5.1 Baryon Interpolators

Since the focus here is the low-lying positive-parity spectrum, a basis of interpolating operators is chosen such that the interpolators have the dominant overlaps with those states. There have been earlier attempts to construct a basis of baryon interpolating operators incorporating the angular structure, respecting the cubic symmetry of the lattice, and being able to access the higher spins in the spectrum [118, 119]. Here, a different approach is adapted for the operator construction proposed in [8, 1]. First, a basis of operators is derived in the continuum, with well-defined continuum spin quantum numbers, and then the operators are subduced onto the lattice.

The interpolating operators follow a continuum construction, and are expressed as a product of terms describing the flavor structure, the Dirac spin, and the orbital angular momentum implemented through derivatives,

$$\left( B_{\Sigma_F} \otimes (S^{P_S})_{\Sigma_S}^n \otimes D_{L, \Sigma_D}^{[d]} \right)^J,$$

where B, S and D denote the flavor, the Dirac spin and the derivative structure respectively, and  $\Sigma_F, \Sigma_S, \Sigma_D$  are the corresponding permutation symmetries. The resulting operators are projected through suitable Clebsch-Gordon coefficients to the total spin J; the label  $n$  distinguishes different combinations that have the same spin structure,  $P_S$  is the parity

while  $d$  is the order of the gauge-covariant derivative applied to the quark fields. The combination of the fields gives objects transforming under rotations with the angular momentum,  $L$ .

As baryons are color-singlet objects, the constituent three valence quarks form totally antisymmetric combinations of the color indices. Furthermore, the baryon interpolating operators have to be antisymmetric under the exchange of any pair of quarks, which is automatically satisfied since they are constructed from anti-commuting Grassmann fields. Thus, the remaining quark labels, namely those of the flavor, the spin, and the spatial structure, have to be in totally symmetric combinations.

Baryon operators can be constructed in a local, color-singlet manner capturing the lowest-lying states. In distillation, the quark fields  $\psi(x)$  are replaced by the quasi-local, smeared fields  $\square\psi(x)$ . This does not change the symmetry property of the interpolating operators, making the lowest-lying states accessible after smearing. To access higher spins in the spectrum, the gauge covariant derivatives are to be included in the construction of the interpolating operators [8] in such a way that the operators have nonzero orbital angular momentum between the quarks, making them nonlocal in nature.

The basis employed comprises the non-relativistic [1] interpolating operators constructed from the upper components, in a suitable  $\gamma$  representation of the Dirac spinors, with up to two covariant derivatives, allowing for operators with up to two units of orbital angular momenta. Additional operators are also included that contain the commutator of two covariant derivatives acting on the same quark field, corresponding to the chromomagnetic components of the gluonic field-strength tensor and denoted by  $D_{L=1,M}^{[2]}$ . It is these operators, which vanish for a unit gauge configuration, that are referred to as the “hybrid” operators. If any of these operators have a dominant overlap onto a state, that state is considered hybrid in nature, signifying nontrivial contribution from gluons.

The lattice regulator explicitly breaks the continuum rotational symmetry, resulting

in the associated symmetry group being reduced to the double-cover octahedral group,  $O_h^D$  for baryons. There are six irreducible representations (irreps.) available in  $O_h^D$ . As this calculation focuses on the positive-parity states, only the operators subduced [8] onto the lattice irreps.  $H_g, G_{1g}$  and  $G_{2g}$ , where the subscript  $g$  denotes positive parity, are considered. For the total angular momentum  $J = \frac{5}{2}$  and higher, the continuum operators are subduced onto multiple irreps., as detailed in Table 5.1. The operators used in the calculation for carrying out the spectral analyses of the nucleon and the delta for different spin- $J$  are listed here using spectroscopic notation,  $X^{2S+1}L_\pi J^P$  where  $X$  is the nucleon,  $N$  or the delta,  $\Delta$ ;  $S$  is the Dirac spin;  $L = S, P, D, \dots$  is the combined angular momentum of the derivatives;  $\pi = S, M$  or  $A$  is the permutation symmetry of the derivatives;  $J$  is the total angular momentum, and  $P$  is the parity. The correlators constructed using these operators receive contributions in the forward direction only from the positive-parity states.

J	irrep. (dimension)	Interpolators ( $\Delta$ )	Interpolators ( $N$ )
$\frac{1}{2}$	$G_{1g}(2)$	$\Delta^2 S_M \frac{1}{2}^+, \Delta^4 D_S \frac{1}{2}^+,$ $\Delta^2 P_M^* \frac{1}{2}^+$	$N^2 S_S \frac{1}{2}^+, N^2 S'_S \frac{1}{2}^+,$ $N^2 S_M \frac{1}{2}^+, N^4 D_M \frac{1}{2}^+,$ $N^2 P_A \frac{1}{2}^+, N^4 P_M^* \frac{1}{2}^+,$ $N^2 P_M^* \frac{1}{2}^+$
$\frac{3}{2}$	$H_g(4)$	$\Delta^4 S_S \frac{3}{2}^+, \Delta^4 S'_S \frac{3}{2}^+,$ $\Delta^4 D_S \frac{3}{2}^+, \Delta^2 D_M \frac{3}{2}^+,$ $\Delta^2 P_M^* \frac{3}{2}^+$	$N^4 S_M \frac{3}{2}^+, N^2 D_S \frac{3}{2}^+,$ $N^4 D_M \frac{3}{2}^+, N^2 D_M \frac{3}{2}^+,$ $N^2 P_A \frac{3}{2}^+, N^4 P_M^* \frac{3}{2}^+,$ $N^2 P_M^* \frac{3}{2}^+$
$\frac{5}{2}$	$G_{2g}(2) \oplus H_g(4)$	$\Delta^4 D_S \frac{5}{2}^+, \Delta^2 D_M \frac{5}{2}^+$	$N^2 D_S \frac{5}{2}^+, N^4 D_M \frac{5}{2}^+,$ $N^2 D_M \frac{5}{2}^+, N^4 P_M^* \frac{5}{2}^+$
$\frac{7}{2}$	$G_{1g}(2) \oplus G_{2g}(2)$ $\oplus H_g(4)$	$\Delta^4 D_S \frac{7}{2}^+$	$N^4 D_M \frac{7}{2}^+$

TABLE 5.1: The  $\Delta$  and  $N$  interpolating operators used in the calculation, written in spectroscopic notation together with their subductions onto the irreps. of the cubic group. The interpolators denoted by asterisk (\*) are hybrid in nature. The interpolator,  $N^2 S'_S \frac{1}{2}^+$  is considered as the radial excitation of the interpolator,  $N^2 S_S \frac{1}{2}^+$  as the only difference between them is that the former has derivatives of order 2 acting on the quark fields, and the later does not. A similar type of interpolator with radial excitation is also included in the spectral analysis of the  $\Delta$  for  $J = \frac{3}{2}$ .

## 5.2 Variational Method

The baryon spectrum can be extracted from the matrices of the two-point correlators where each two-point correlator is constructed by applying the baryon creation and annihilation operators at the source and the sink respectively,

$$C_{ij}(t) = \langle 0 | \mathcal{O}_i(t) \overline{\mathcal{O}}_j(0) | 0 \rangle, \quad (5.1)$$

where, without loss of generality, the source is taken at time slice 0 and the sink at time slice  $t$ . Here,  $i, j$  label the operators in a given representation of the cubic group. Inserting a complete set of eigenstates of the Hamiltonian, the two-point correlator can be written as

$$C_{ij}(t) = \sum_{\mathbf{n}} \frac{1}{2E_{\mathbf{n}}} \langle 0 | \mathcal{O}_i | \mathbf{n} \rangle \langle \mathbf{n} | \overline{\mathcal{O}}_j | 0 \rangle e^{-E_{\mathbf{n}}t}, \quad (5.2)$$

where the sum is over all the states that have the same quantum numbers as the interpolating operators  $\mathcal{O}_{i,j}$  and  $E_{\mathbf{n}}$  is the energy of the state. In a finite volume, this yields a discrete set of energies.

A variety of approaches have been developed to obtain the energies and operator overlaps for the excited baryon spectrum [97, 113]. The variational method employs the technique of finding the best linear combination of the operators within a given symmetry channel for each state in the spectrum. This method is implemented in this calculation following Ref. [120, 8, 1]. The variational method starts by solving the generalized eigenvalue equation for the two-point correlator matrix,

$$C(t) u_{\mathbf{n}} = \lambda_{\mathbf{n}}(t, t_0) C(t_0) u_{\mathbf{n}}, \quad (5.3)$$

where  $u_{\mathbf{n}}$  are the generalized eigenvectors which satisfy the orthonormality condition

$u_{\mathbf{n}}^\dagger C(t_0) u_{\mathbf{n}'} = \delta_{\mathbf{n}\mathbf{n}'}$ , and give the optimal interpolator for the state as  $\sum_i u_{\mathbf{n}}^i \overline{\mathcal{O}}_i$ . The generalized eigenvalues, also known as the principal correlators,  $\lambda_{\mathbf{n}}(t, t_0)$  behave as

$$\lambda_{\mathbf{n}}(t, t_0) = e^{-E_{\mathbf{n}}(t-t_0)} \left[ 1 + \mathcal{O}(e^{-\delta E(t-t_0)}) \right]. \quad (5.4)$$

Here  $E_{\mathbf{n}}$  is the energy of the state labeled by  $\mathbf{n}$ , and  $\delta E$  represents the contributions from the other states. The subsequent results are derived from the two-state fits to the principal correlators of this form, described below. Furthermore,  $C_{ij}(t)$  can be decomposed into the form

$$C_{ij}(t) = \sum_{\mathbf{n}} \frac{Z_i^{\mathbf{n}*} Z_j^{\mathbf{n}}}{2E_{\mathbf{n}}} e^{-E_{\mathbf{n}}t}. \quad (5.5)$$

Here,  $t$  is assumed to be much smaller than the temporal extent of the lattice, allowing one to ignore the contributions from the opposite-parity states arising from the other time ordering on the periodic lattice. The overlap factor  $Z_i^{\mathbf{n}} = \langle 0 | O_i | \mathbf{n} \rangle$  can be written as

$$Z_i^{\mathbf{n}} = (U_g^{-1})_i^{\mathbf{n}} \sqrt{2E_{\mathbf{n}}} \exp\left(\frac{E_{\mathbf{n}}t_0}{2}\right), \quad (5.6)$$

where the matrix,  $U_g$  is formed using the generalized eigenvectors  $u_{\mathbf{n}}$  as its columns. The overlaps can thereby be obtained from the solution of the generalized eigenvector matrix.

The eigenvectors should be time-independent, but in practice, Eq. (5.3) is solved for the eigenvalues,  $\lambda_{\mathbf{n}}$ , and the eigenvectors,  $u_{\mathbf{n}}$ , independently on each time slice,  $t$ , allowing them to vary with  $t$ . As the baryon spectra have a high level of degeneracy, ordering the states by the size of their eigenvalues at each time slice might not always give the right ordering. The ordering of the states might change among the Jackknife samples or between different time slices, resulting in additional noise to the calculation. Instead, a reference time slice is chosen on which the reference eigenvectors are defined as  $u_{\mathbf{n}}^{\text{ref}} \equiv u_{\mathbf{n}}(t_{\text{ref}})$ , and the eigenvectors on the other time slices are compared by finding the maximum value of

$u_{\mathbf{n}'}^{\text{ref}\dagger} C(t_0) u_{\mathbf{n}}$  which associates a state  $\mathbf{n}$  with a reference state  $\mathbf{n}'$ . This procedure prevents the principal correlators or the eigenvectors associated with a certain state from becoming associated with another state, as functions of  $t$ .

The orthogonality of the generalized eigenvectors on the metric  $C(t_0)$  is a good approximation to the true orthogonality in the continuum with an infinite number of states and operators. On the lattice where the calculation is done with a finite number of interpolators, this approximation is a good one if the two-point correlator at  $t_0$  is dominated by the lightest states. The orthogonality approximation can be improved by taking a large value of  $t_0$ , as, at a large time slice, the higher excited states decay exponentially. But, at larger time slices, the two-point correlators become increasingly noisy and the noise can enter into the solution of the generalized eigenvalue problem through  $C(t_0)$ . The procedure to choose an optimal value of  $t_0$  implemented in this calculation is to define a goodness-of-fit quantity which compares the input data with a reconstructed version of the data calculated from the fitted parameters using Eq. (5.4), (5.5) and (5.6). The goodness-of-fit quantity used in this calculation is defined as [120],

$$\chi^2 = \frac{1}{\frac{1}{2}N_m(N_m + 1)(t_{\text{max}} - t_0) - \frac{1}{2}N_m(N_m + 3)} \times \sum_{i,j \geq i} \sum_{t,t'=t_0+1}^{t_{\text{max}}} (C_{ij}(t) - C_{ij}^{\text{rec.}}(t)) \mathbb{C}_{ij}^{-1}(t,t') (C_{ij}(t') - C_{ij}^{\text{rec.}}(t')). \quad (5.7)$$

where  $N_m$  is the dimension of the two-point correlator matrix,  $C_{ij}^{\text{rec.}}$  is the reconstructed two-point correlators from the fitted parameters, and  $\mathbb{C}$  is the data correlation matrix for the correlator  $C_{ij}$  computed with the jackknife statistics. The goodness-of-fit quantity is normalised by the number of degrees of freedom which is defined as the number of observables less the number of parameters in the fit. In the first line of Eq. (5.7), the first term of the denominator gives the total number of observables, and the second term can be rewritten as  $\frac{1}{2}N_m(N_m + 1) + N_m$ . Now, from Eq. (5.6) and (5.6), it can be seen that

the second term in the denominator of Eq. (5.7) gives the number of parameters in the fit as  $\frac{1}{2}N_m(N_m + 1)$  is the number of fitting parameters in the matrix  $U_g$ , and there are also  $N_m$  number of fitting parameters,  $E_n$  in the expression of  $Z_i^n$ . Thus, Eq. (5.7) calculates  $\chi^2$  for each degree of freedom.

For a fixed  $t_0$ , the overlap factors are calculated for each time slice, and the time slice,  $t_Z > t_0$  is found for which the operator overlap factors give the minimum  $\chi^2$ . Since the operator overlaps are reasonably flat, the variation of  $\chi^2$  with respect to  $t_Z$  is mild. The same procedure is repeated for different  $t_0$ , and the optimum value of  $t_0$  is chosen by minimizing  $\chi^2$ . If  $t_0$  is taken too small, the reconstruction of the two-point correlators for  $t > t_0$  would be poor. The reconstruction keeps getting better with the increase of  $t_0$  until statistical noise prevents further improvement.

### 5.3 Fitting Procedure

After solving Eq. (5.3) for a range of  $t_0$ , the resulting principal correlators are fitted to the two-exponential form [8] for each  $t_0$  to extract the baryon energy spectra:

$$\lambda_n(t, t_0) = (1 - A_n) e^{-E_n(t-t_0)} + A_n e^{-E'_n(t-t_0)}. \quad (5.8)$$

Here,  $E_n$  gives the energy of the state while  $E'_n$  and  $A_n$  are other fit parameters. As the orthogonality condition at  $t_0$  is an approximation, there are contributions from other states leaking into the principal correlators. The second exponential isolates most of the effect of these other states.

The fitting range is such that, for each principal correlator, only the time slices are included for which the noise-to-signal ratio is less than 0.05; in practice, this restricts the largest value of  $t$  included in the fits to be around 8. Furthermore, only the correlators

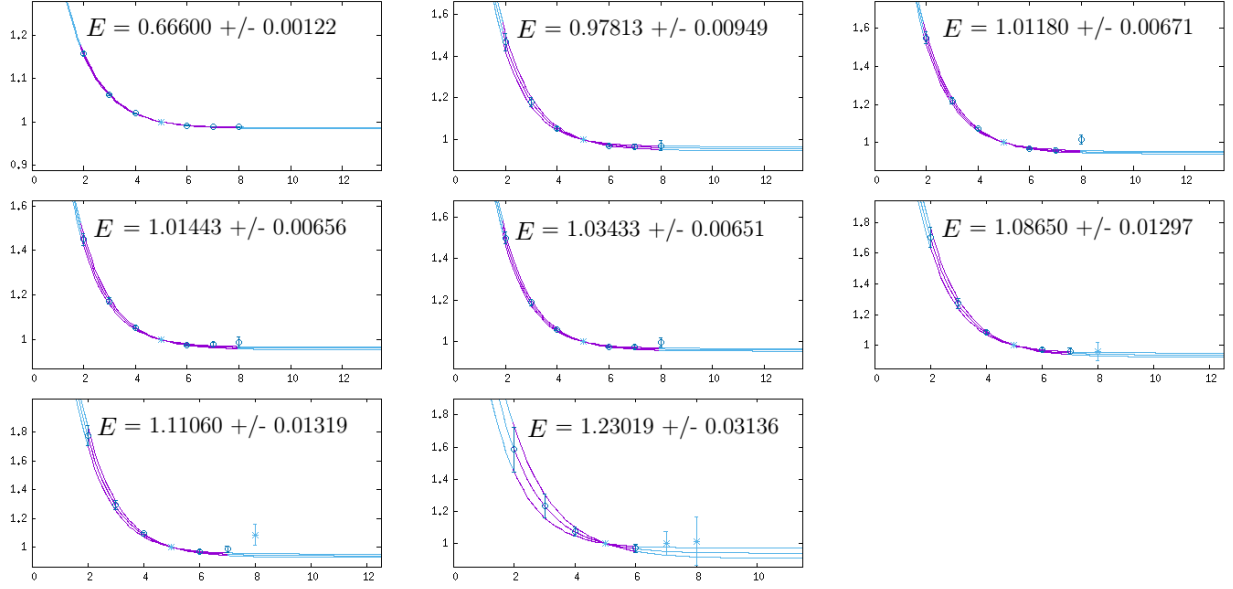


FIG. 5.1: Fits to the principal correlators for the low-lying positive-parity spectrum of the  $H_g$  irrep. of the  $\Delta$  on the ensemble  $a094m358$ , using  $t_0 = 5$ . The plots show  $\lambda_n(t, t_0) \cdot e^{E_n(t-t_0)}$  data on the y axes and the lattice time slices on the x axes; the curves are two-exponential fits as described in the text. In each panel, the energy corresponding to the leading exponential state is labeled by  $E$  and given in lattice units.

with the source-sink separation greater than two lattice units are included in the analysis to avoid possible contact terms. For each  $t_0$ , each fit to the principal correlator is based on an acceptable  $\chi^2/\text{dof}$ . The coefficient  $A_n$  is required to be less than around 0.1. It is found in the analysis that for large  $t_0$ , all the parameters,  $E'_n$  are larger than any energy of the spectra,  $E_n$  for a certain symmetry channel. For smaller  $t_0$ , this observation is not always true indicating that there are not enough states to hold the orthogonality condition properly at these  $t_0$ . As at large  $t_0$ ,  $A_n$  is smaller and  $E'_n$  is larger, the contribution from the second exponential falls more rapidly with the increase of the source-sink separation. The overlap factors of Eq. (5.6) are also calculated using the eigenvectors at a reference time slice,  $t_Z$ .

In Figure 5.1, fits to the leading the principal correlators for the  $H_g$  irrep. of the  $\Delta$  are shown. In these plots, the principal correlators are divided by the dominant time-

dependence due to state  $\mathbf{n}$ , making it easier to examine the contributions from other states. For each panel, the curves are the reconstructions from the fitted parameters with the purple region indicating the data points included in the fit. If a single exponential were to dominate the fit, it means that the contributions from other states are contributing to the fitting procedure and a constant value of unity for all time slices would be plotted. But in all the panels in Figure 5.1, exponential falls are observed, indicating that the contributions from other states are captured in the second exponent quite well. The approach of the plateaux close to unity at large time slices is indicative of the small value of  $A_{\mathbf{n}}$  in the fits. As anticipated, the uncertainties on the leading energy increase as the energy increases.

## 5.4 Spin Identification

The breaking of the rotational symmetry induced by the discretization onto the lattice renders the determination of the spin corresponding to the different energy levels within the irreps. less than straightforward. In the case of the glueball spectrum in pure Yang-Mills theory [121], the identification of the spins was accomplished by the identification of the degeneracies across different lattice irreps in the approach to the continuum limit. This requires the generation of the ensembles at several lattice spacings, a formidable task once quark degrees of freedom are included, and further requires statistical precision far beyond that attainable with a reasonable computational cost to delineate the overlapping energies within the spectrum. There is a need for a spin identification method that uses data obtained from only a single lattice spacing, albeit one sufficiently fine that it preserves the rotational symmetry to a sufficient degree at the hadronic scale.

Here the method introduced in Ref. [17], and applied for the baryon spectrum in Refs. [8, 1] is used whereby the operator overlap factors are used to identify the spin of a state. It relies on the observation that each operator used in the calculation carries an

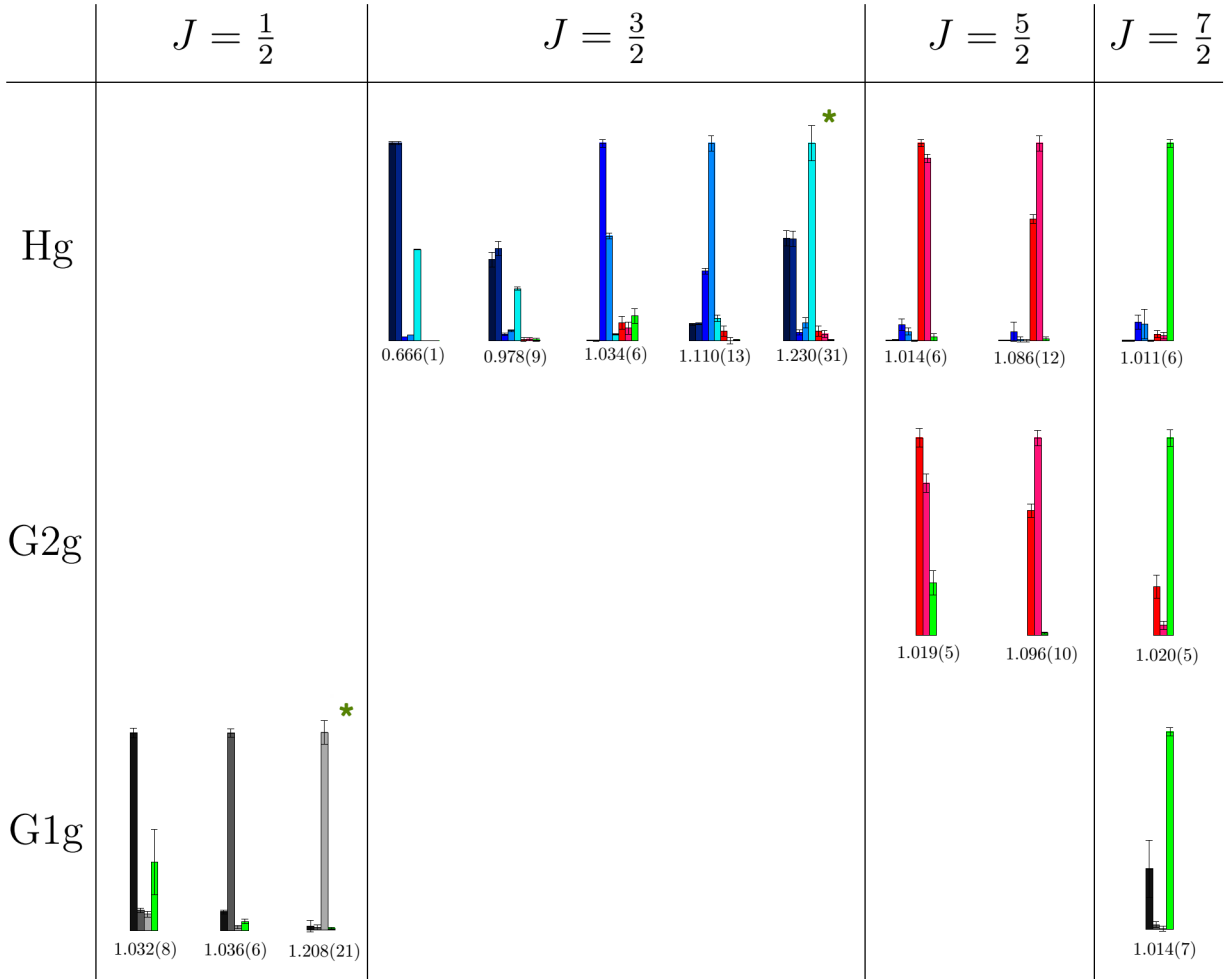
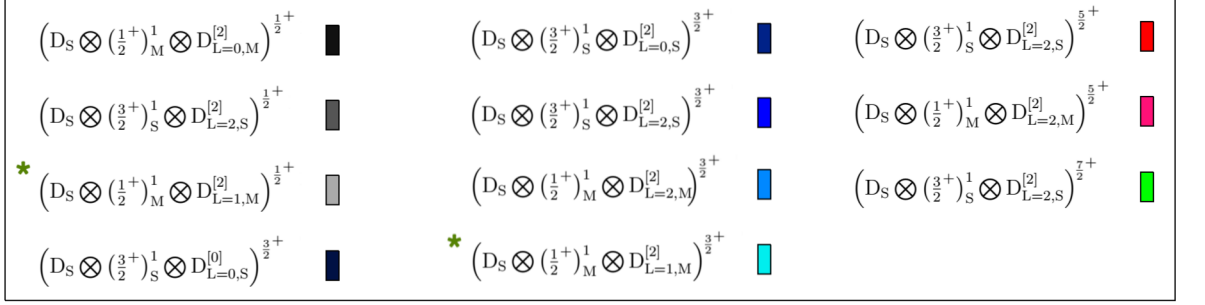


FIG. 5.2: Histogram plot of the operator overlaps,  $Z$  for the  $\Delta$  on the  $a094m358$  ensemble, normalized such that, for a given operator, the largest overlap across all the states is unity. The overlaps are obtained from a variational analysis across all the operators within a given lattice irrep, irrespective of the continuum spin from which they are derived. The histogram plot of each state is accompanied by its energy in lattice units. The asterisks denote the hybrid-type operators, and the energy levels identified with them.

essence of the continuum spin of the operator from which it is subduced, and therefore, it is expected that an operator subduced from, say angular momentum  $J$ , has large overlaps only with states of the same continuum angular momentum  $J$ . Positive-parity states corresponding to the continuum angular momentum  $J = \frac{5}{2}$  and  $J = \frac{7}{2}$  will appear in the spectrum of the  $H_g$  and  $G_{2g}$  irreps, and of the  $H_g$ ,  $G_{1g}$  and  $G_{2g}$  irreps respectively, and it is expected that the overlaps would be dominated by the operators subduced from the same continuum operators across those irreps. This is indeed what is observed, as can be seen in Figure 5.2 for the  $\Delta$  spectrum, where the overlaps are obtained from a variational analysis using all the operators within a given lattice irrep. Further, it is found that the resulting energies are degenerate, with, for states of spin  $\frac{5}{2}$  and  $\frac{7}{2}$ , the energies obtained in the  $H_g$  irrep. being within 1% of the values obtained in the  $G_{1g}$  irrep. and, for the case of spin  $\frac{7}{2}$ ,  $G_{1g}$  and  $G_{2g}$  irreps.

Rather than applying the variational method to a basis comprising all the operators within a lattice irrep., a method which employs a more restricted basis of the operators comprising those within an irrep. derived from a given continuum,  $J$ , is applied. In Figure 5.3, the  $\Delta$  spectrum obtained by analyzing all the operators within a given lattice irrep. is compared with that where the variational method is applied in each lattice irrep. only to those operators derived from a given continuum spin. The comparison reveals that there are no significant differences between these two spectra, prompting one to analyze the operators of each angular momentum separately as this requires calculating the two-point correlators using a smaller basis of operators at one time. Since the computational cost of computing the full correlation matrix goes as the square of the operator basis, this reduces the computational cost significantly.

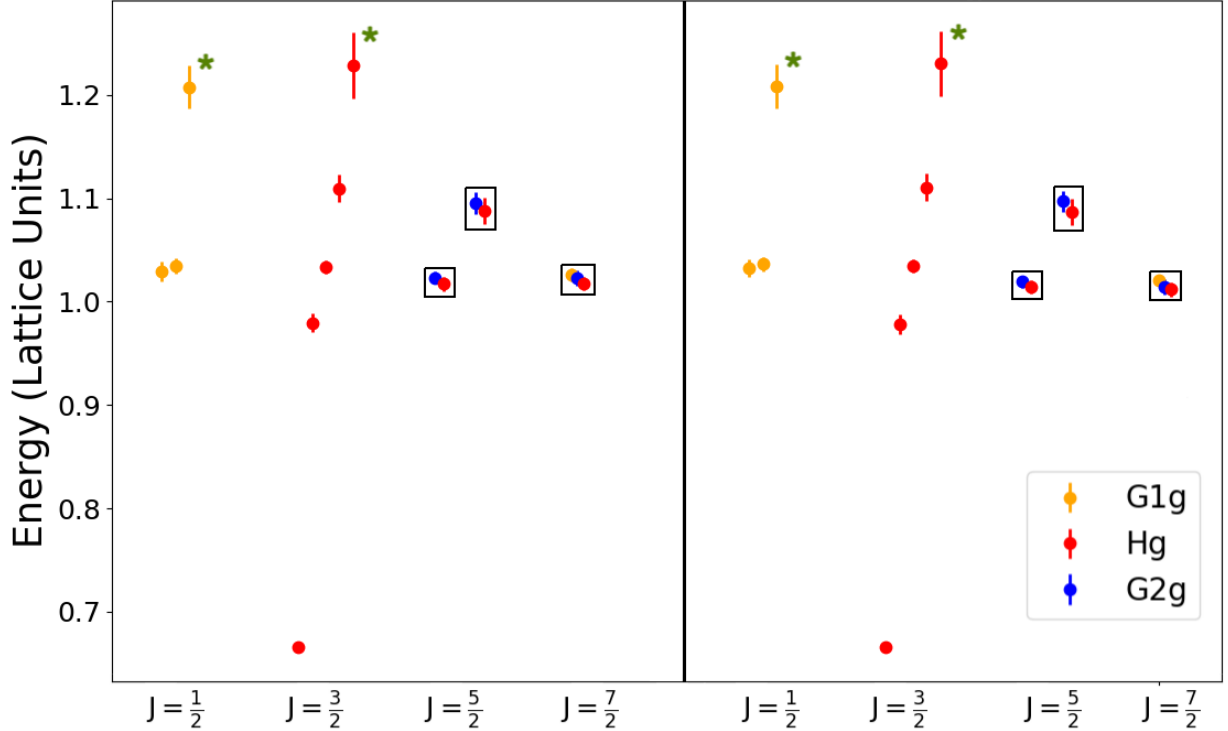


FIG. 5.3: Comparison of the low-lying  $\Delta$  spectra on the  $a094m358$  ensemble between fitting only those operators within an irrep. derived from the continuum operators of a given angular momentum (left), and fitting all the operators within a lattice irrep., irrespective of their continuum antecedents (right). For the states identified as spin  $\frac{5}{2}$  and  $\frac{7}{2}$ , the boxes contain the energy levels obtained after the subduction onto the different lattice irreps. Energy levels identified as those of hybrid states are denoted by the green asterisks.

## 5.5 Stability under variation of Distillation Space

The previous studies of the low-lying baryon spectrum using the implementation of distillation employed  $N_D = 56$  distillation eigenvectors, on a  $16^3$  spatial lattice with  $a \simeq 0.123$  fm [8]. With the expected scaling of the number of eigenvectors with physical volume, it is suggested that as many as 230 eigenvectors might be needed to capture the same physics on the ensembles employed here, with in excess of three times the physical spatial volume compared to the previous calculations [1]. In this study, the perambulators and the baryon elementals are generated encoding the operators for  $N_D = 64$  distillation eigenvectors, and the sensitivity of the extracted spectra to the variation of  $N_D$  is examined.

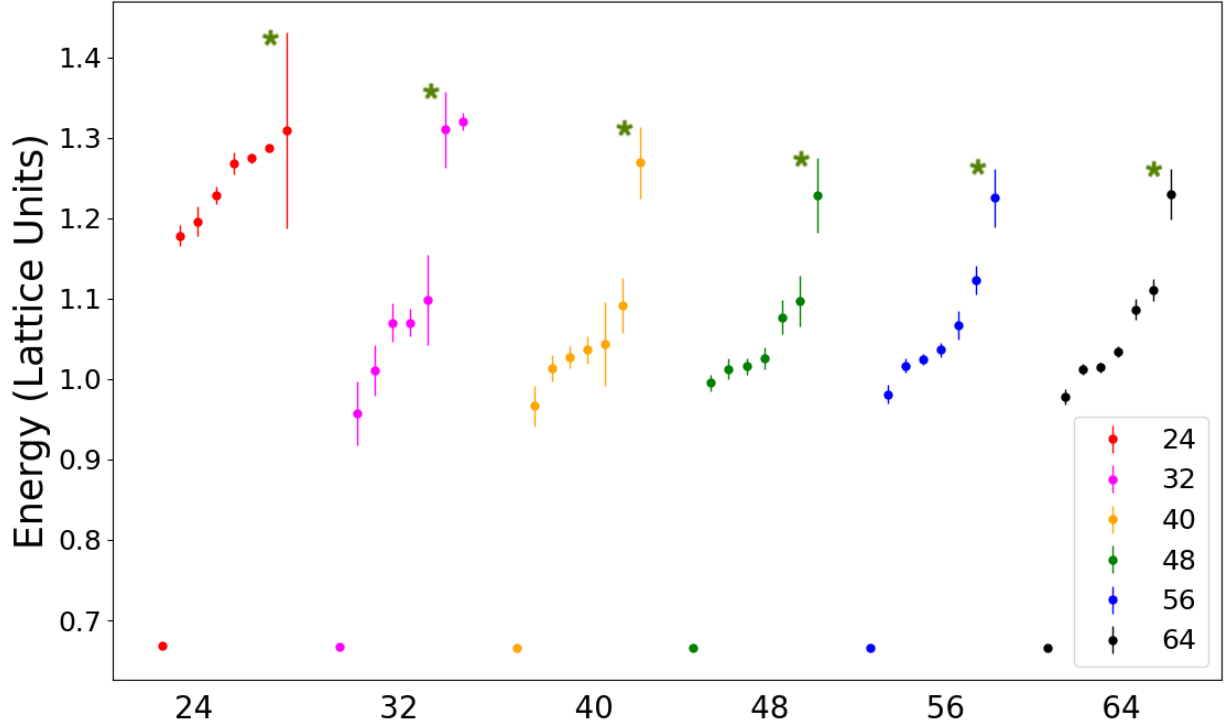


FIG. 5.4: The dependence of the  $\Delta$  spectrum in the  $H_g$  irrep. on the number of distillation eigenvectors,  $N_D$  for the ensemble  $a094m358$  of Table 4.1. The states identified as hybrid baryons are indicated by the green asterisks.

A study of the various charges of the  $N$ , both for a state at rest [100], and nonzero spatial momentum [101], performed on the same lattices as those employed here, suggests that the ground state properties can indeed be resolved with this number of eigenvectors. However, ascertaining the sensitivity of the results for the spectrum and the overlaps of the excited states is an important prerequisite for subsequent discussions.

In Figure 5.4, the lowest energy levels in the positive-parity  $H_g$  irreducible representation of the  $\Delta$  are shown as the number of distillation eigenvectors is reduced down to  $N_D = 24$ . While the ground state can indeed reliably be extracted with only a minimal number of eigenvectors, the lowest five states that are obtained with acceptable uncertainties are consistent only between the  $N_D = 56$  and  $N_D = 64$  determinations. Since a major aim of this work is establishing evidence for the properties of the extracted states, as ev-

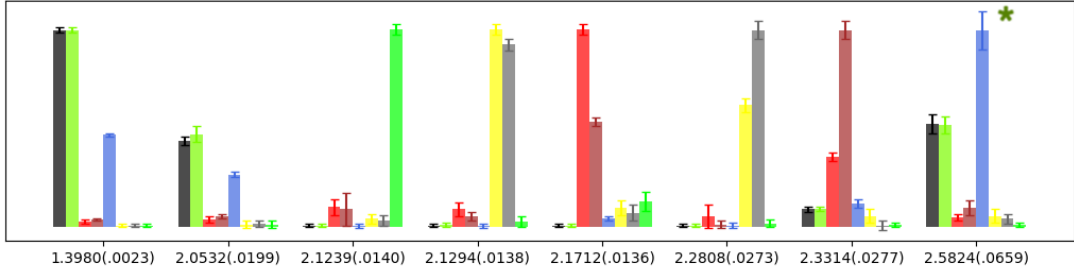
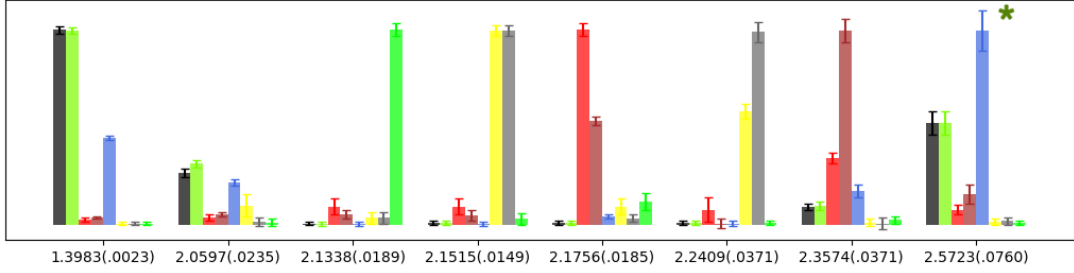
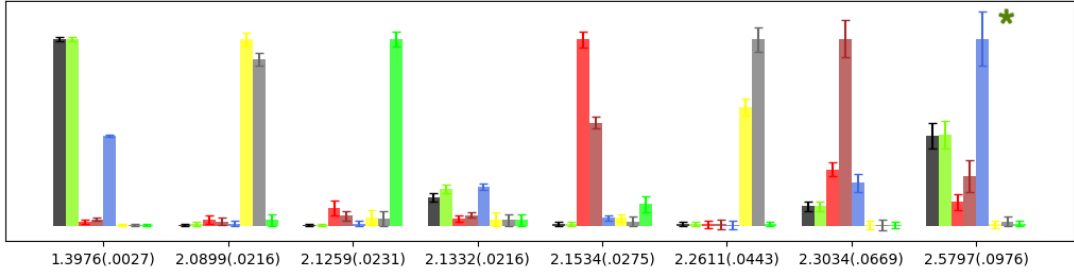
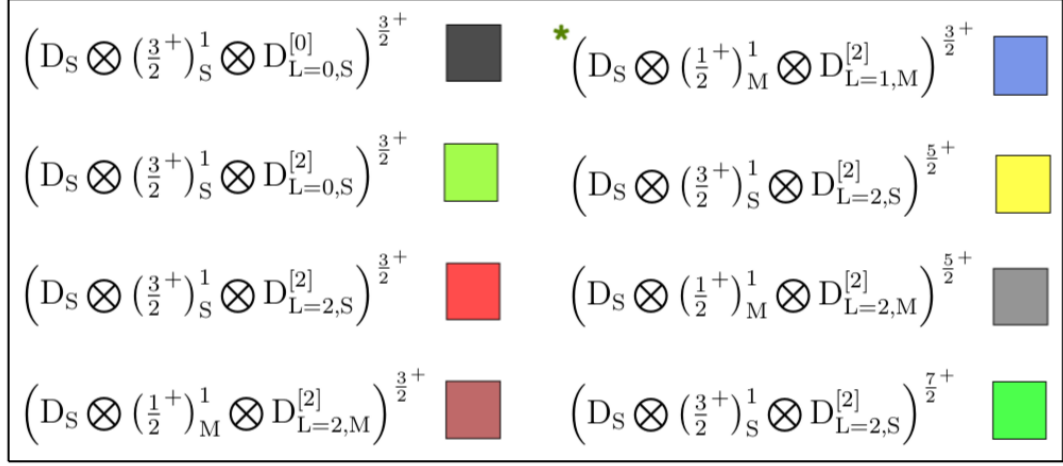


FIG. 5.5: The top, the middle, and the bottom panels show the overlaps of the different operators within the  $H_g$  irreducible representation of the  $\Delta$  using the  $a094m358$  ensemble for  $N_D = 48, 56$  and  $64$ , respectively. The energies of the states are given in units of GeV. The asterisks denote hybrid-type operators and the energy levels associated with them.

identified through the operator overlaps, the certainty of whether these features are robust under the rank of the distillation space is needed. In Figure 5.5, the operator overlaps corresponding to the energies in Figure 5.4 are shown. As for the case of the energies, the overlaps, and in particular, the dominant operators corresponding to each state, show stability between  $N_D = 56$  and  $N_D = 64$ , but with some qualitative differences, notably in the ordering of the states, for  $N_D = 48$ . Therefore,  $N_D = 64$  is used in the remainder of this calculation.

## 5.6 Delta and Nucleon Spectra

The low-lying positive-parity spectra of the  $\Delta$  and the  $N$  for both the  $a094m278$  and the  $a094m358$  ensembles using this fitting procedure are shown in Figures 5.6 and 5.7, respectively. For the spin  $\frac{5}{2}$  and spin  $\frac{7}{2}$  energy levels, the splittings between the values obtained in the  $H_g$  and the  $G_{2g}$ , and in the  $H_g$ , the  $G_{2g}$  and the  $G_{1g}$  irreps, respectively, are remarkably small, reflecting the  $\mathcal{O}(a^2)$  breaking of the rotational symmetry, and the smaller spatial lattice spacing than that used in comparable studies using an anisotropic lattice. As expected, the quality of the spectrum is somewhat worse at the lighter value of the quark mass, and the spin identification procedure is less convincing for the highest states in the  $N$  spectrum. The qualitative properties of the spectrum, and in particular the counting of the states, is consistent with that obtained on the anisotropic lattices at a coarser value of the spatial lattice spacing, but at a considerably finer value of the temporal lattice spacing. Notably, the calculation does not exhibit the low-lying Roper resonance, in accord with calculations using the anisotropic action, and indeed most calculations using a Wilson-type action. A reliable extraction of the Roper resonance will require the calculation of the momentum-dependent scattering amplitudes in the manner of Lüscher's finite volume method [122] and its extensions. A prerequisite for this is likely the incorporation of

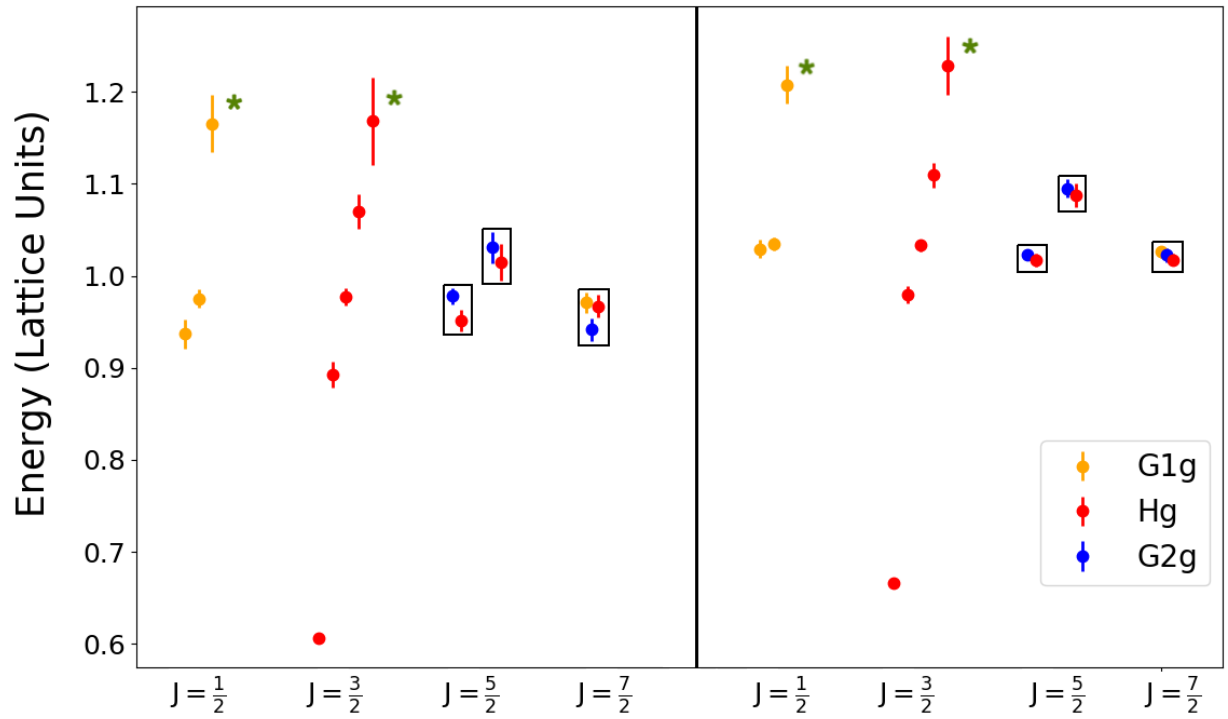


FIG. 5.6: The low-lying positive-parity  $\Delta$  spectrum in lattice units on the  $a094m278$  (left) and the  $a094m358$  (right) ensembles, using the fitting procedure described in the text. For the states identified as spin  $\frac{5}{2}$  and  $\frac{7}{2}$ , the boxes contain the energy levels obtained after the subduction onto the different lattice irreps. Energy levels identified as those of hybrid baryons are denoted by the green asterisks.

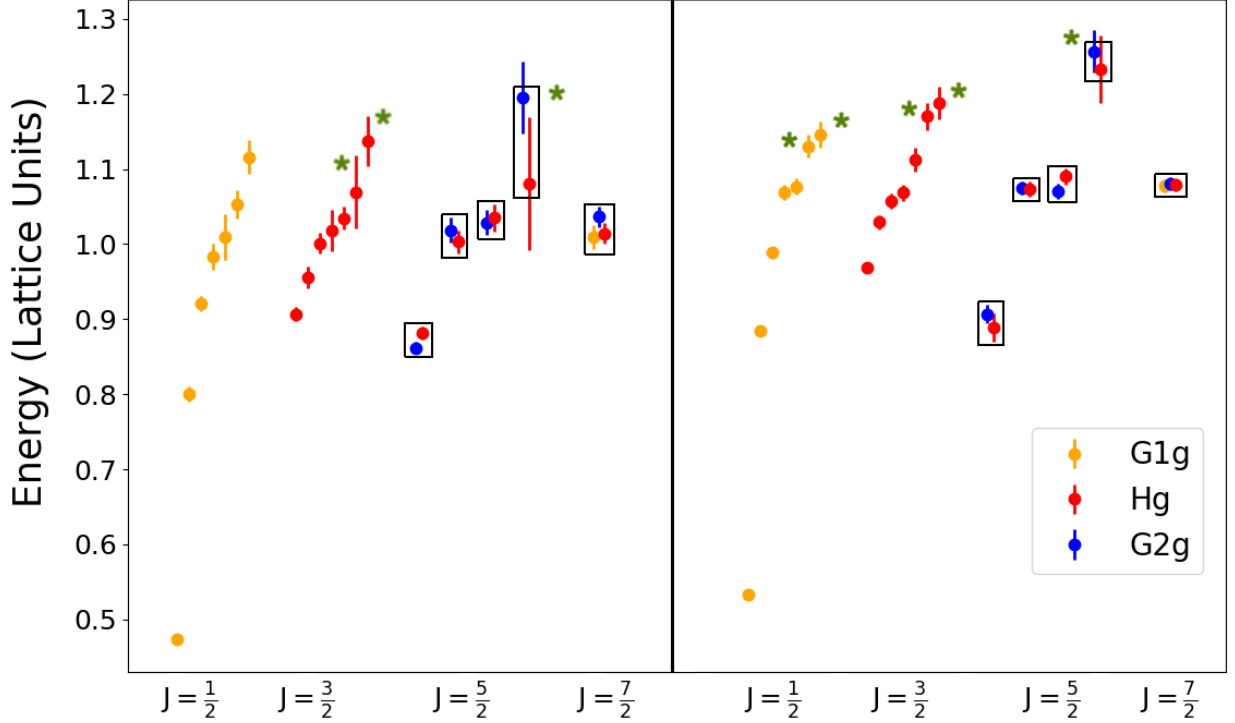


FIG. 5.7: The low-lying positive-parity  $N$  spectrum in lattice units on the  $a094m278$  (left) and the  $a094m358$  (right) ensembles, using the fitting procedure described in the text. For the states identified as spin  $\frac{5}{2}$  and  $\frac{7}{2}$ , the boxes contain the energy levels obtained after the subduction onto the different lattice irreps. Energy levels identified as those of hybrid baryons are denoted by the green asterisks.

multi-hadron operators.

### 5.6.1 Hybrid States

In contrast to the case of the meson spectrum, “exotic” baryons cannot be distinguished through their quantum numbers. Therefore, the identification of baryons as “hybrid” in nature inevitably involves a degree of interpretation. Here, the hybrid states are identified as those whose overlap, defined through Eq. (5.6), is dominated by the hybrid-type operators, which would vanish in absence of gauge fields [1]. For the case of the  $\Delta$ , this identification is very apparent, as can be seen in Figure 5.2 for the  $a094m358$  ensemble, where one hybrid state is found in the  $J = \frac{1}{2}$  channel and one in  $J = \frac{3}{2}$  channel. For the  $N$

spectrum on the  $a094m358$  ensemble, there is clear evidence for the hybrid-baryon states through the nature of their overlaps, where two states in the  $J = \frac{1}{2}$  channel, two states in the  $J = \frac{3}{2}$  channel, and one state in the  $J = \frac{5}{2}$  channel are found to be hybrid in nature. On the  $a094m278$  ensemble, the identification and multiplicities of the hybrid baryons follow those of the  $a094m358$  ensemble except for the  $J = \frac{1}{2}$  channel in the  $N$  spectrum, where there is no obvious candidate for a hybrid baryon using the criterion of the operator overlaps. In spite of this, the multiplicity in both the  $\Delta$  and the  $N$  spectrum confirm the findings in the earlier studies using an anisotropic lattice [1], with a multiplicity of states at least as rich as the quark model, and the presence of the additional states that appear to be hybrid in nature. A complete treatment of the spectra requires the determination of the momentum-dependent amplitudes following the method first introduced by Lüscher [122], and implemented in a number of lattice calculations [123, 124, 125]. In practice, this approach necessitates the inclusion of multi-hadron operators.

## 5.7 Comparison with Previous Work

The results are now compared with those of previous work, and in particular, the previous calculation of the low-lying positive-parity baryon spectrum obtained on the heavier of the two anisotropic clover lattices employed in Ref. [1]. To facilitate this comparison, the excitation energies are considered with respect to the ground state nucleon energy, in units of the  $\Omega$  mass, a quantity that is somewhat insensitive to the light-quark masses. In Figures 5.8 and 5.9, the comparison among these lattices for the  $J = \frac{1}{2}$  and  $J = \frac{3}{2}$  channels for the  $\Delta$  and the  $N$  are shown respectively. Also shown are the lowest-lying non-interacting two-particle energy levels.

A notable feature of most of the states for both the  $\Delta$  and the  $N$  is that the splitting with respect to the ground state nucleon energy shows only a weak dependence on the

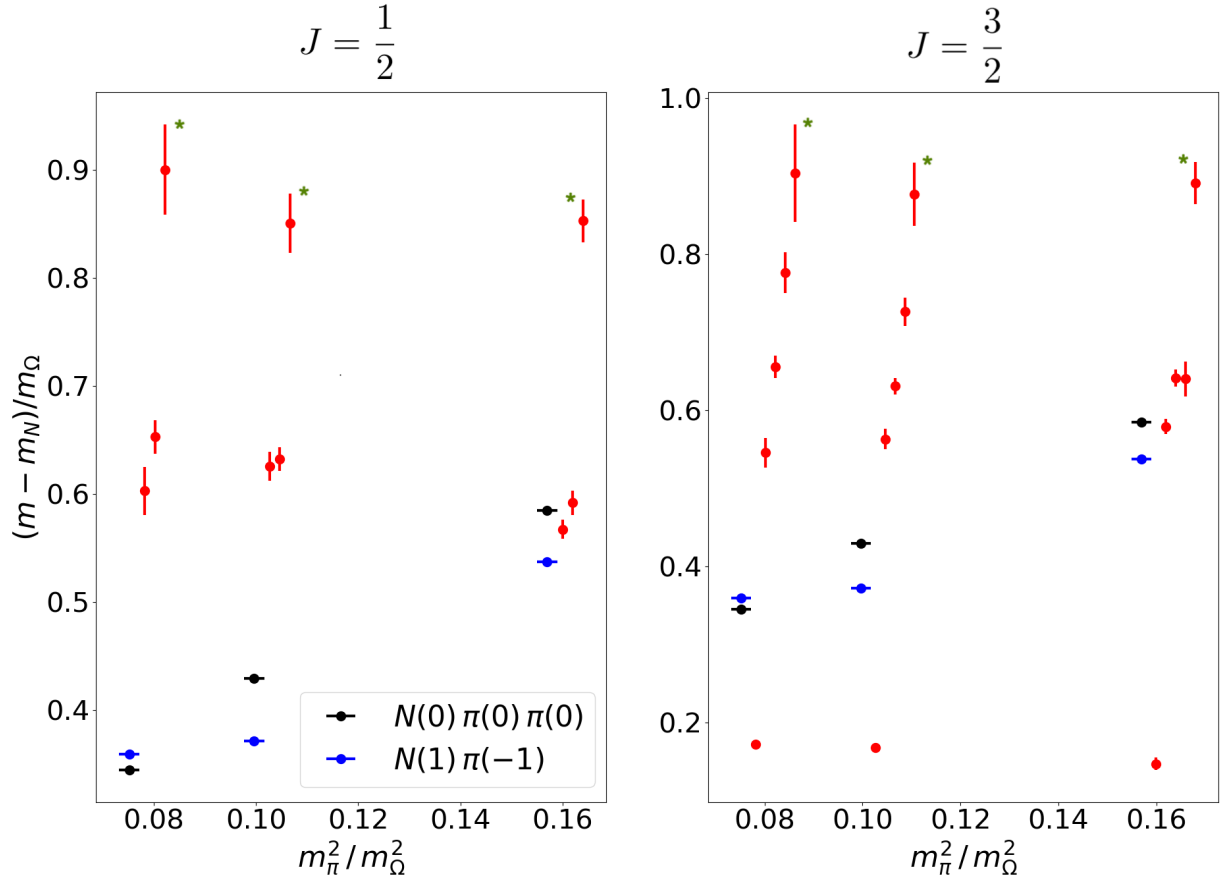


FIG. 5.8: The left and right panels show the excitation energies for the  $\Delta$  with respect to the ground state nucleon on each of the lattices studied here, vs.  $m_\pi^2$ , together with the corresponding result from Ref. [1], for the  $J = \frac{1}{2}$  and the  $J = \frac{3}{2}$  channels respectively. The excitation energies at the right-most side in both the panels are from Ref. [1]. The  $\Omega$  mass is used to set the scale. The higher excited states are displaced for clarity. The multi-hadron energy thresholds,  $N(0)\pi(0)\pi(0)$  and  $N(1)\pi(-1)$  are identified by horizontal dashes, where  $N$  and  $\pi$  are denoted by their spatial momenta as their arguments, in units of  $\frac{2\pi}{aL}$ , where  $L$  is the spatial extent of the lattice, and  $a$  is the lattice spacing.

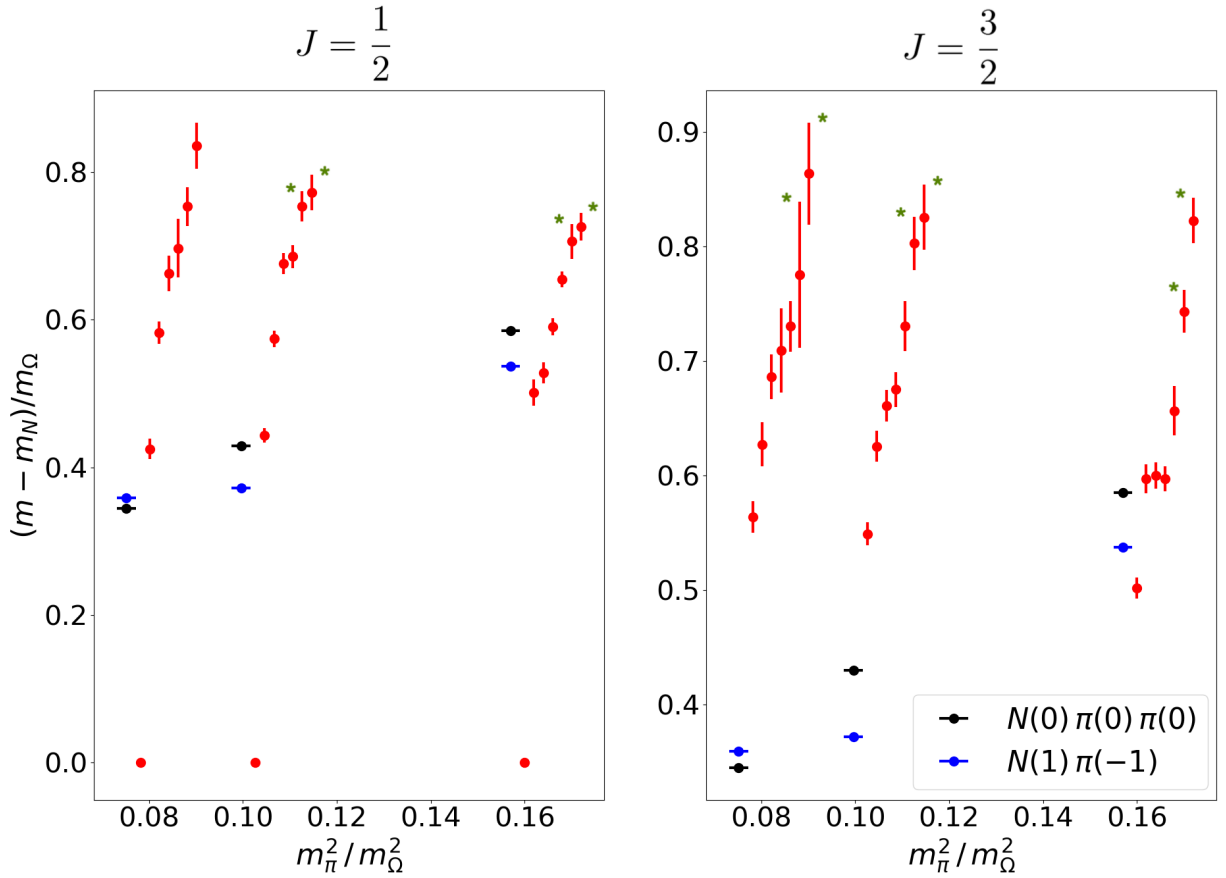


FIG. 5.9: The left and right panels show the excitation energies for the  $N$  with respect to the ground state nucleon on each of the lattices studied here, vs.  $m_\pi^2$ , together with the corresponding result from Ref. [1], for the  $J = \frac{1}{2}$  and the  $J = \frac{3}{2}$  channels respectively. The excitation energies at the right-most side in both the panels are from Ref. [1]. The  $\Omega$  mass is used to set the scale. The higher excited states are displaced for clarity. The multi-hadron energy thresholds,  $N(0)\pi(0)\pi(0)$  and  $N(1)\pi(-1)$  are identified by horizontal dashes, where  $N$  and  $\pi$  are denoted by their spatial momenta as their arguments, in units of  $\frac{2\pi}{aL}$ , where  $L$  is the spatial extent of the lattice, and  $a$  is the lattice spacing.

quark masses, while the energies of the non-interacting two-particle states exhibit a far stronger dependence. This suggests that predominantly the “single-hadron” states are observed rather than the multi-hadron states, and this leads to the assertion that the three-quark operators used in this study couple only weakly to the multi-hadron states. These observations are more prominent for the hybrid baryons whose energies, with respect to the ground state nucleon energy, remain more or less the same irrespective of the quark masses. However, there is one qualification to this observation, namely that the first excited state energy seen in the  $N^{\frac{1}{2}}$  channel exhibits a stronger dependence on the light-quark masses, and is indeed consistent with that of  $N(0)\pi(0)\pi(0)$  and  $N(1)\pi(-1)$  multi-hadron states, where  $N$  and  $\pi$  are denoted by their spatial momenta as their arguments, in units of  $\frac{2\pi}{aL}$ , where  $L$  is the spatial extent of the lattice, and  $a$  is the lattice spacing. The behavior of the  $N^{\frac{1}{2}}$  channel emphasises the need to apply the full panoply of the Lüscher’s finite volume method [122] as one proceeds to lower values of the light-quark masses.

A focus of this study is whether the identification of the hybrid baryons is robust. In Figures 5.10 and 5.11, the overlap distributions of the dominant operators for each of the states of all the three ensembles for  $J = \frac{3}{2}$  in the case of the  $\Delta$ , and for  $J = \frac{1}{2}$  in the case of the  $N$  are shown. For the  $\Delta$ , the hybrid baryon in each of the ensembles has almost identical overlap distribution across the operators, with the hybrid operator having the predominant overlap. The ground states also have a comparable distribution across the three ensembles, though the work here includes an additional operator whose orbital structure is of the form  $D_{L=0,S}^{[2]}$  that can be interpreted as an operator of additional width with respect to the  $S$ -type orbital,  $D_{L=0,S}^{[0]}$ , and therefore of the same orbital structure.

For the case of the  $N$ , the identification and ordering of the hybrid baryons is comparable between the heavier  $a094m358$  ensemble and the anisotropic ensemble, but for the lighter  $a094m278$  ensemble, that identification is less obvious in spite of having significant overlaps from the hybrid operators. As in the case of the  $\Delta$ , there is consistency in the

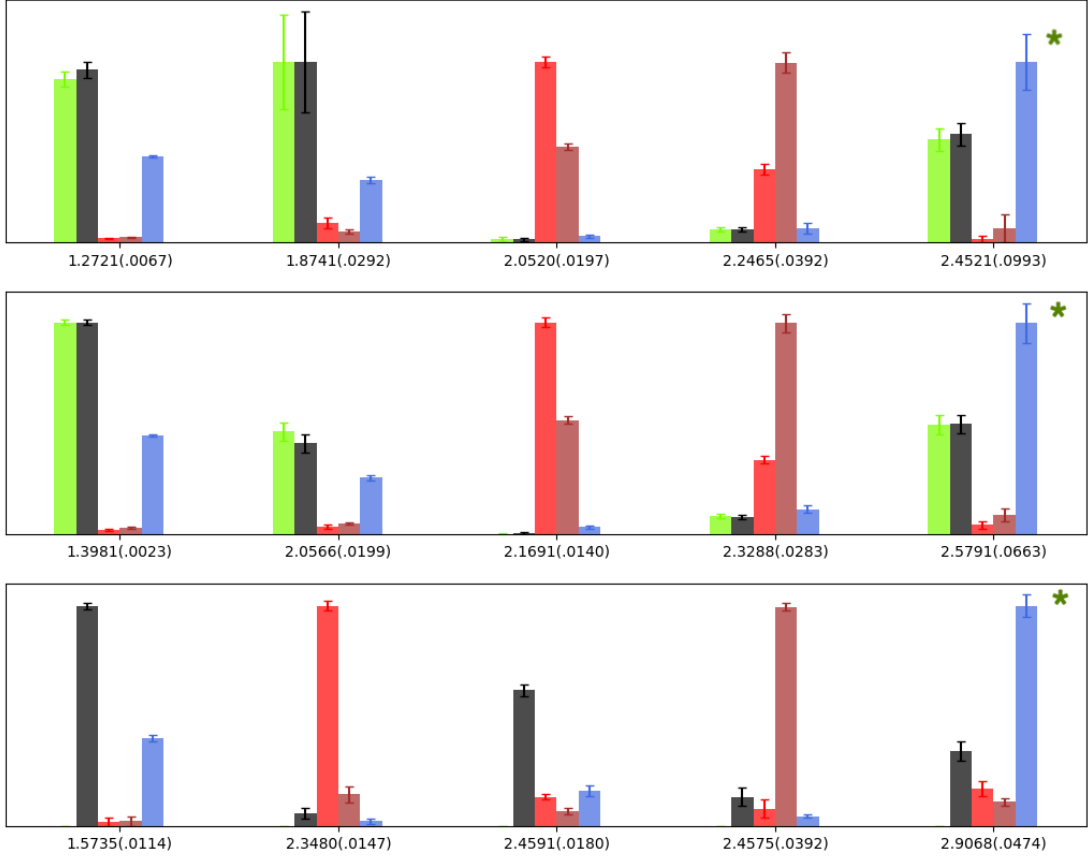
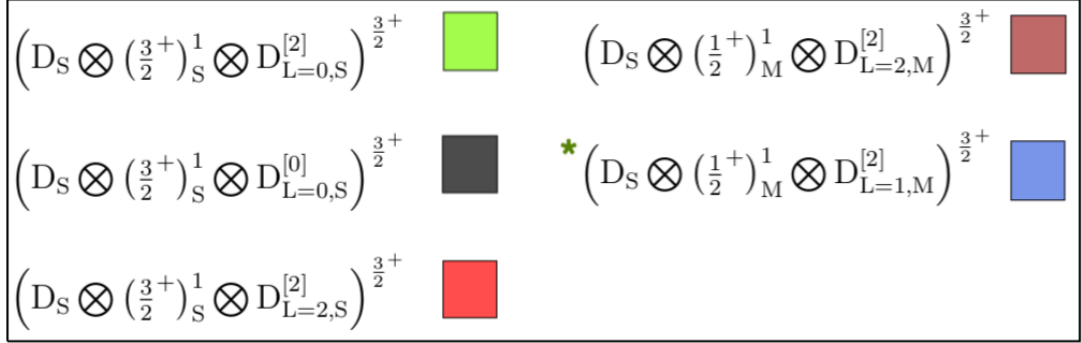


FIG. 5.10: The top, the middle, and the bottom panels show the overlaps of the different operators within the channel  $J = \frac{3}{2}$  of the  $\Delta$  for the ensembles  $a094m278$ ,  $a094m358$  and from [1] respectively. The energies of the states are given in the units of GeV. The green asterisks denote the hybrid-type operators, and the energy levels identified with them.

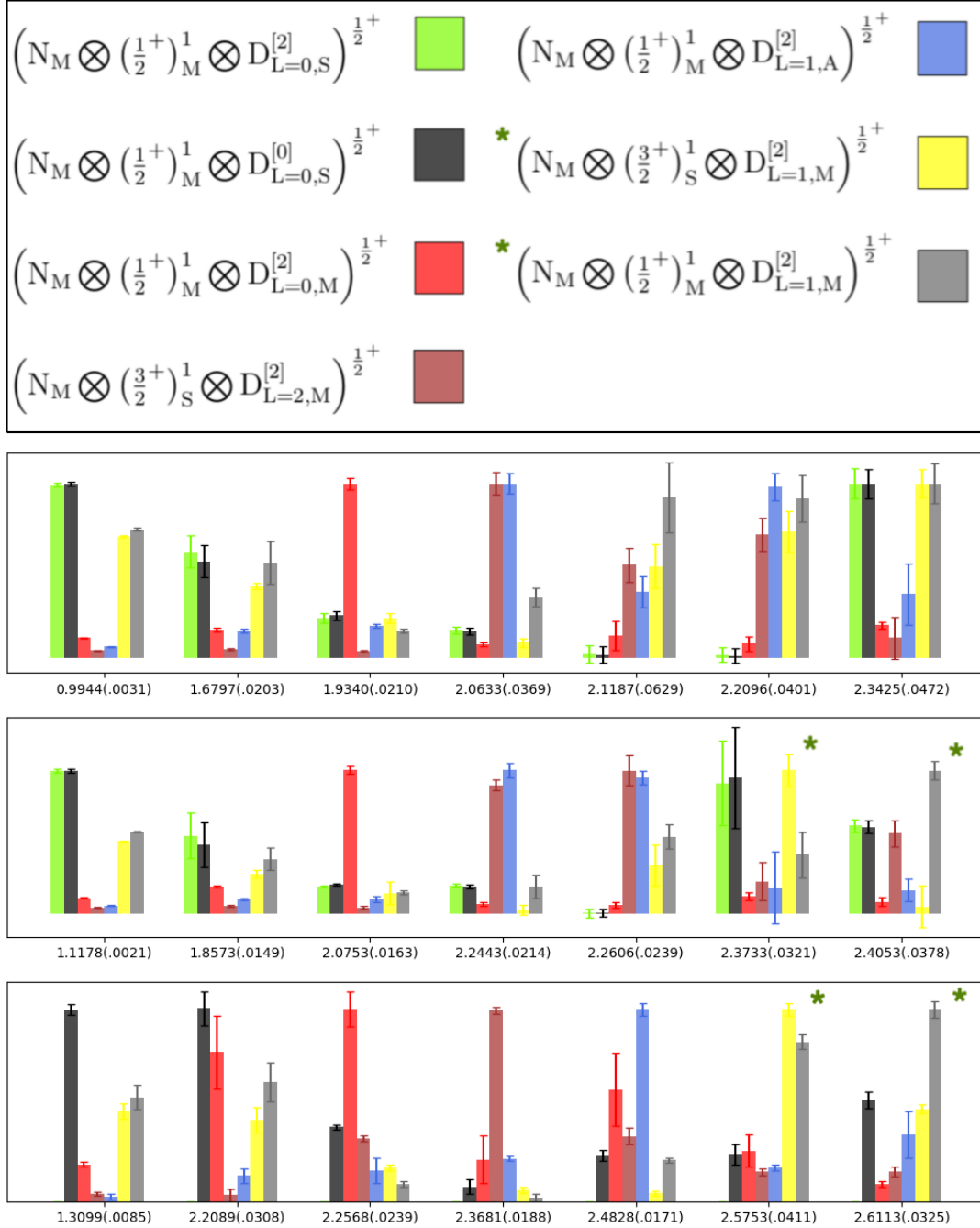


FIG. 5.11: The top, the middle, and the bottom panels show the overlaps of the different operators within the channel  $J = \frac{1}{2}$  of the  $N$  for the ensembles  $a094m278$ ,  $a094m358$  and from [1] respectively. The energies of the states are given in the units of GeV. The green asterisks denote the hybrid-type operators, and the energy levels identified with them.

overlaps for the ground state and the first two excited states across all three ensembles.

The technique of identifying hybrid baryons in the lattice calculations performed on the ensembles  $a094m358$  and  $a094m278$ , and in [1] involves obtaining operator overlap distributions which largely depend on the operators themselves. In the lattice calculations performed in this project, the hybrid baryons are found to be consistent with [1] despite having different pion masses, action, and lattice spacing. This confirms that the hybrid-type states are indeed key features of the  $\Delta$  and  $N$  spectra on the lattice. For the ensemble  $a094m278$ , the  $N$  spectra do not show clear identifications of hybrid baryons. This reiterates the necessity of the treatment of  $N$  spectra on lattices with lighter pion mass to a greater extent, involving momentum-dependent amplitudes.

# CHAPTER 6

## Gluon PDF Calculation

### 6.1 Theoretical Background

#### 6.1.1 Matrix Elements

To access the unpolarized gluon PDF, the required matrix elements are constructed for the spin-averaged nucleon with the operators composed of two gluonic fields connected by a Wilson line. The general form of the matrix elements is

$$M_{\mu\alpha;\lambda\beta}(z, p) \equiv \langle p | G_{\mu\alpha}(z) W[z, 0] G_{\lambda\beta}(0) | p \rangle. \quad (6.1)$$

Here,  $z_\mu$  is the separation between the gluonic fields,  $p_\mu$  is the 4-momentum of the nucleon,  $W[z, 0]$  is the standard straight-line Wilson line in the adjoint representation,

$$W[a, b] = \mathcal{P} \exp \left\{ i g_s \int_0^1 d\eta (a - b)^\mu \tilde{A}_\mu(\eta a + (1 - \eta)b) \right\}, \quad (6.2)$$

where  $\mathcal{P}$  indicates that the integral is path ordered. The matrix elements can be decomposed into the invariant amplitudes,  $\mathcal{M}_{pp}$ ,  $\mathcal{M}_{zz}$ ,  $\mathcal{M}_{zp}$ ,  $\mathcal{M}_{pz}$ ,  $\mathcal{M}_{ppzz}$  and  $\mathcal{M}_{gg}$  using the four-vectors,  $p_\mu$  and  $z_\mu$ , and the metric tensor  $g_{\mu\nu}$  [70],

$$\begin{aligned}
M_{\mu\alpha;\lambda\beta}(z, p) &= (g_{\mu\lambda}p_\alpha p_\beta - g_{\mu\beta}p_\alpha p_\lambda - g_{\alpha\lambda}p_\mu p_\beta + g_{\alpha\beta}p_\mu p_\lambda) \mathcal{M}_{pp} \\
&+ (g_{\mu\lambda}z_\alpha z_\beta - g_{\mu\beta}z_\alpha z_\lambda - g_{\alpha\lambda}z_\mu z_\beta + g_{\alpha\beta}z_\mu z_\lambda) \mathcal{M}_{zz} \\
&+ (g_{\mu\lambda}z_\alpha p_\beta - g_{\mu\beta}z_\alpha p_\lambda - g_{\alpha\lambda}z_\mu p_\beta + g_{\alpha\beta}z_\mu p_\lambda) \mathcal{M}_{zp} \\
&+ (g_{\mu\lambda}p_\alpha z_\beta - g_{\mu\beta}p_\alpha z_\lambda - g_{\alpha\lambda}p_\mu z_\beta + g_{\alpha\beta}p_\mu z_\lambda) \mathcal{M}_{pz} \\
&+ (p_\mu z_\alpha - p_\alpha z_\mu) (p_\lambda z_\beta - p_\beta z_\lambda) \mathcal{M}_{ppzz} + (g_{\mu\lambda}g_{\alpha\beta} - g_{\mu\beta}g_{\alpha\lambda}) \mathcal{M}_{gg}. \quad (6.3)
\end{aligned}$$

The light-cone gluon distribution is obtained from

$$g^{\alpha\beta} M_{+\alpha;\beta+}(z_-, p) = -2p_+^2 \mathcal{M}_{pp}(\nu, 0), \quad (6.4)$$

where  $z$  is taken in the light-cone “minus” direction,  $z = z_-$ , and  $p^+$  is the momentum in the light-cone “plus” direction. The PDF is determined by the  $\mathcal{M}_{pp}$  amplitude,

$$-\mathcal{M}_{pp}(\nu, 0) = \frac{1}{2} \int_{-1}^1 dx e^{-ix\nu} x g(x). \quad (6.5)$$

The density of the momentum carried by the gluons,  $\mathcal{G}(x) = x g(x)$  is the natural quantity in this definition of the gluon PDF, rather than  $g(x)$ . The field-strength tensor  $G_{\mu\alpha}$  is antisymmetric with respect to its indices and  $g_{--} = 0$ , so the left-hand side of Eq. (6.4) reduces to a summation over the transverse indices  $i, j = x, y$ ; perpendicular to the direction of the separation between the two gluonic fields. The matrix element  $M_{ti;it}$  decomposes into the invariant amplitudes [70]

$$M_{ti;it} = 2p_0^2 \mathcal{M}_{pp} + 2\mathcal{M}_{gg}, \quad (6.6)$$

where  $\mathcal{M}_{gg}$  is a contamination term which can be removed using the matrix element [70]

$$M_{ji;ij} = \langle p | G_{ji}(z) W[z, 0] G_{ij}(0) | p \rangle = -2\mathcal{M}_{gg}. \quad (6.7)$$

Thus, the proper combination of the matrix elements to extract the twist-2 invariant amplitude  $\mathcal{M}_{pp}$  is

$$M_{ti;it} + M_{ji;ij} = 2p_0^2 \mathcal{M}_{pp}. \quad (6.8)$$

For the spatially separated fields, the gauge link operator has extra ultraviolet divergences not present for the light-like-separated fields. The combination of the matrix elements  $M_{ti;it}$  is multiplicatively renormalizable [126] and, because of the antisymmetry of the gluonic fields, the combination  $M_{ji;ij}$  can be written as

$$M_{ji;ij} = 2 \langle p | G_{yx}(z) W[z, 0] G_{xy}(0) | p \rangle, \quad (6.9)$$

which contains only one set of indices  $\{\mu\alpha; \lambda\beta\}$ , making explicit the fact that this matrix element is multiplicatively renormalizable too [127]. Furthermore, both  $M_{ti;it}$  and  $M_{ji;ij}$  have the same one-loop UV anomalous dimension [70], making the whole combination in Eq. (6.8) multiplicatively renormalizable at the one-loop level, at least.

### 6.1.2 Reduced Matrix Elements

The extended gluonic operator has additional link-related ultraviolet (UV) divergences which are multiplicatively renormalizable [128, 129, 130]. These UV divergences can be canceled by taking the appropriate ratios. The combination of the matrix elements from Eq. (6.8) is denoted by  $\mathcal{M}(\nu, z^2)$  for the rest of this discussion. The ratio [71] of this

combination to its rest-frame value is taken, keeping the field separation the same. This ratio cancels out the  $\nu$ -independent UV factor  $Z(z^2/a^2)$ , making the ratio UV-finite. The kinematic factors remaining in the ratio can be removed by taking the ratio of the nonzero field-separated to the zero field-separated matrix elements, at fixed Ioffe-time, in both the numerator and the denominator [73]. The resulting reduced matrix element, the reduced pseudo-ITD, can be written as

$$\mathfrak{M}(\nu, z^2) = \left( \frac{\mathcal{M}(\nu, z^2)}{\mathcal{M}(\nu, 0)|_{z=0}} \right) / \left( \frac{\mathcal{M}(0, z^2)|_{p=0}}{\mathcal{M}(0, 0)|_{p=0, z=0}} \right). \quad (6.10)$$

By taking the ratio, the  $z^2$ -dependent, but  $\nu$ -independent, non-perturbative factors that  $\mathcal{M}(\nu, z^2)$  may contain are also eliminated. The residual polynomial ‘‘higher twist’’ dependence on  $z^2$ , if visible, should be explicitly fitted to separate it from the twist-2 contribution.

### 6.1.3 Position-space Matching

The reduced pseudo-ITD has a logarithmic  $z^2$  dependence. The reduced pseudo-ITD,  $\mathfrak{M}(\nu, z^2)$ , is related to the gluon and singlet quark light-cone ITD,  $\mathcal{I}_g(\nu, \mu^2)$  and  $\mathcal{I}_S(\nu, \mu^2)$  in the  $\overline{\text{MS}}$  scheme through the short distance factorization relationship with  $z^2$  as the hard scale. Here,  $\mathcal{I}_g(\nu, \mu^2)$  is related to the gluon PDF,  $g(x, \mu^2)$ , by

$$\mathcal{I}_g(\nu, \mu^2) = \frac{1}{2} \int_{-1}^1 dx e^{ix\nu} x g(x, \mu^2). \quad (6.11)$$

The product  $x g(x, \mu^2)$  is an even function of  $x$ , so the real part of  $\mathcal{I}_g(\nu, \mu^2)$  is given by the cosine transform of  $x g(x, \mu^2)$ , while its imaginary part vanishes. Neglecting the higher twist terms  $\mathcal{M}_{zz}$ ,  $\mathcal{M}_{zp}$ ,  $\mathcal{M}_{pz}$ ,  $\mathcal{M}_{ppzz}$ , and keeping just the  $\mathcal{M}_{pp}$  term, the one-loop

matching relation becomes [70, 131]

$$\begin{aligned} \mathfrak{M}(\nu, z^2) = & \frac{\mathcal{I}_g(\nu, \mu^2)}{\mathcal{I}_g(0, \mu^2)} - \frac{\alpha_s N_c}{2\pi} \int_0^1 du \frac{\mathcal{I}_g(u\nu, \mu^2)}{\mathcal{I}_g(0, \mu^2)} \\ & \times \left\{ \ln\left(\frac{z^2 \mu^2 e^{2\gamma_E}}{4}\right) B_{gg}(u) + 4 \left[ \frac{u + \ln(\bar{u})}{\bar{u}} \right]_+ + \frac{2}{3} [1 - u^3]_+ \right\} \\ & - \frac{\alpha_s C_F}{2\pi} \ln\left(\frac{z^2 \mu^2 e^{2\gamma_E}}{4}\right) \int_0^1 dw \frac{\mathcal{I}_S(w\nu, \mu^2)}{\mathcal{I}_g(0, \mu^2)} \mathfrak{B}_{gq}(w). \end{aligned} \quad (6.12)$$

The singlet quark Ioffe-time distribution  $\mathcal{I}_S(\nu, \mu^2)$  is related to the singlet quark distribution, summed over the quark flavors. The Altarelli-Parisi kernel,  $B_{gg}(u)$ , is given by

$$B_{gg}(u) = 2 \left[ \frac{(1 - u\bar{u})^2}{1 - u} \right]_+, \quad (6.13)$$

and the quark-gluon mixing kernel is given by

$$\mathfrak{B}_{gq}(w) = \left[ 1 + (1 - w)^2 \right]_+, \quad (6.14)$$

where the plus-prescription is

$$\int_0^1 du \left[ f(u) \right]_+ g(u) = \int_0^1 du f(u) \left[ g(u) - g(1) \right], \quad (6.15)$$

and  $\bar{u} \equiv (1 - u)$ . Here,  $\gamma_E$  is the Euler–Mascheroni constant and  $C_F$  is the quadratic Casimir operator in the fundamental representation. Determining the singlet quark Ioffe-time distribution requires evaluation of the disconnected diagrams, which involves the computationally demanding calculation of the trace of the all-to-all quark propagator [132], but these are expected to contribute only a little to the matching. The quark-gluon mixing is neglected in this calculation, making the matching relation,

$$\begin{aligned}
\mathfrak{M}(\nu, z^2) &= \frac{\mathcal{I}_g(\nu, \mu^2)}{\mathcal{I}_g(0, \mu^2)} - \frac{\alpha_s N_c}{2\pi} \int_0^1 du \frac{\mathcal{I}_g(u\nu, \mu^2)}{\mathcal{I}_g(0, \mu^2)} \\
&\times \left\{ \ln \left( \frac{z^2 \mu^2 e^{2\gamma_E}}{4} \right) B_{gg}(u) + 4 \left[ \frac{u + \ln(\bar{u})}{\bar{u}} \right]_+ + \frac{2}{3} [1 - u^3]_+ \right\}.
\end{aligned} \tag{6.16}$$

This matching relation in Eq. (6.16) is utilized to extract the gluon light-cone ITD, and in turn the gluon PDF from the reduced pseudo-ITD.

## 6.2 Computational Framework

The lattice calculation of the unpolarized gluon PDF is performed on the ensemble *a094m358*. The calculation is performed on all the 64 temporal sources over 349 gauge configurations, where each configuration is separated from the next configuration by 10 HMC trajectories. The details of the ensemble, *a094m358* are tabulated in Table 4.1.

### 6.2.1 Gluonic Current Calculation

The gluonic currents, inserted into the nucleon to calculate the matrix elements, are not connected to the nucleon state by any quark propagator, so the currents are largely decoupled from the nucleon part of the calculation itself. As a result, on the lattice, the gluonic currents and the nucleon two-point correlators can be calculated separately. They are combined to obtain the three-point correlators from which the matrix elements are extracted. On the lattice, the gluonic current can be written with the Wilson line in the fundamental representation as

$$O(G_{\mu\alpha}, G_{\lambda\beta}, z) \equiv G_{\mu\alpha}(z) U(z, 0) G_{\lambda\beta}(0) U(0, z). \tag{6.17}$$

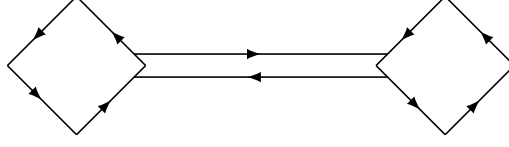


FIG. 6.1: Graphical representation of the gluonic current,  $O(G_{\mu\alpha}, G_{\lambda\beta}, z)$ . The rectangles on both the sides represent the field-strength tensors and the lines connecting them represent the Wilson lines on the lattice.

The field-strength tensor can be expressed in terms of the  $(1 \times 1)$  plaquette,  $U_{\mu,\nu}^{(1 \times 1)}$ , as [133]

$$\frac{-i}{2} \left[ U_{\mu,\nu}^{(1 \times 1)} - U_{\mu,\nu}^{(1 \times 1)\dagger} - \frac{1}{3} \text{Tr} \left( U_{\mu,\nu}^{(1 \times 1)} - U_{\mu,\nu}^{(1 \times 1)\dagger} \right) \right] = g_s a^2 \left[ G_{\mu\nu} + \mathcal{O}(a^2) + \mathcal{O}(g_s^2 a^2) \right], \quad (6.18)$$

where  $a$  is the lattice spacing,  $\beta = 6/g_s^2$  and  $U_{\mu,\nu}$  is given in Eq. (3.22). One-third of the trace is subtracted here to enforce the traceless property of the Gell-Mann matrices. The  $(1 \times 1)$  plaquette is defined as the product of the link variables forming a  $(1 \times 1)$  loop on the lattice. To reduce statistical fluctuations, the average of the four possible plaquettes that can be constructed by changing the signs of  $\mu$  and  $\nu$  is taken. A graphical representation of the gluonic current on the lattice is shown in Figure 6.1. The gluonic currents  $O(G_{ti}, G_{it}, z)$  and  $O(G_{ji}, G_{ij}, z)$  are combined to calculate  $\mathcal{M}_{pp}$ .

As the lattice calculation is performed in Euclidean space, and the PDF is to be extracted in Minkowskian space, it is imperative to check whether any sign change is to be accounted for when the conversion from the Euclidean to the Minkowskian space is done. Now, to contract the indices of the two field strength tensors  $G_{\mu\nu}$  of the gluonic current, one field strength tensor has to be in the covariant form and the other one in the contravariant form. In Euclidean space, these two forms are identical as the metric tensor in this space is a simple identity. But, in the Minkowskian space, the elements of

the covariant and the contravariant forms might differ in sign due to the nontrivial metric tensor in this space.

The field strength tensor is a rank-2 tensor, so it can be represented by a 2-D matrix. The covariant field strength tensor in the Minkowskian space can be written in the matrix form

$$[G_{\mu\nu}]_M = \begin{bmatrix} 0 & G_{tx} & G_{ty} & G_{tz} \\ G_{xt} & 0 & G_{xy} & G_{xz} \\ G_{yt} & G_{yx} & 0 & G_{yz} \\ G_{zt} & G_{zx} & G_{zy} & 0 \end{bmatrix}_M. \quad (6.19)$$

Here, the subscript,  $M$  stands for Minkowskian. Now, the contravariant field strength tensor in the Minkowskian space is

$$\begin{aligned} [G^{\mu\nu}]_M &= [g^{\mu\rho} G_{\rho\sigma} g^{\sigma\nu}]_M \\ &= \begin{bmatrix} 1 & 0 & 0 & 0 \\ 0 & -1 & 0 & 0 \\ 0 & 0 & -1 & 0 \\ 0 & 0 & 0 & -1 \end{bmatrix} \begin{bmatrix} 0 & G_{tx} & G_{ty} & G_{tz} \\ G_{xt} & 0 & G_{xy} & G_{xz} \\ G_{yt} & G_{yx} & 0 & G_{yz} \\ G_{zt} & G_{zx} & G_{zy} & 0 \end{bmatrix}_M \begin{bmatrix} 1 & 0 & 0 & 0 \\ 0 & -1 & 0 & 0 \\ 0 & 0 & -1 & 0 \\ 0 & 0 & 0 & -1 \end{bmatrix} \\ &= \begin{bmatrix} 1 & 0 & 0 & 0 \\ 0 & -1 & 0 & 0 \\ 0 & 0 & -1 & 0 \\ 0 & 0 & 0 & -1 \end{bmatrix} \begin{bmatrix} 0 & -G_{tx} & -G_{ty} & -G_{tz} \\ G_{xt} & 0 & -G_{xy} & -G_{xz} \\ G_{yt} & -G_{yx} & 0 & -G_{yz} \\ G_{zt} & -G_{zx} & -G_{zy} & 0 \end{bmatrix}, \quad (6.20) \end{aligned}$$

yielding

$$[G^{\mu\nu}]_M = \begin{bmatrix} 0 & G^{tx} & G^{ty} & G^{tz} \\ G^{xt} & 0 & G^{xy} & G^{xz} \\ G^{yt} & G^{yx} & 0 & G^{yz} \\ G^{zt} & G^{zx} & G^{zy} & 0 \end{bmatrix}_M = \begin{bmatrix} 0 & -G_{tx} & -G_{ty} & -G_{tz} \\ -G_{xt} & 0 & G_{xy} & G_{xz} \\ -G_{yt} & G_{yx} & 0 & G_{yz} \\ -G_{zt} & G_{zx} & G_{zy} & 0 \end{bmatrix}_M . \quad (6.21)$$

As a result, the sign changes between the covariant and the contravariant forms of the  $tx$  and  $ty$  components of the field strength tensor in the Minkowskian space. But for the  $xy$  component, the sign remains the same. The contractions of indices produce these relations between the Minkowskian and the Euclidean quantities:

$$\begin{aligned} [G_{tx}G^{xt}]_M &= (-1) [G_{tx}G_{xt}]_E , & [G_{ty}G^{yt}]_M &= (-1) [G_{ty}G_{yt}]_E , \\ [G_{xy}G^{yx}]_M &= [G_{xy}G_{yx}]_E . \end{aligned} \quad (6.22)$$

Here, the subscript  $E$  stands for the Euclidean quantities. As there are no differences between the covariant and the contravariant form of tensors in the Euclidean space, all the indices of the Euclidean quantities are placed as subscripts. These sign changes are incorporated in the gluonic current, making the total current

$$O_g(z) = G_{ji}(z) U(z, 0) G_{ij}(0) U(0, z) - G_{ti}(z) U(z, 0) G_{it}(0) U(0, z) . \quad (6.23)$$

## 6.2.2 Gradient Flow

The gauge fields are modified by the gradient flow [134, 135, 136] in this calculation to reduce the ultraviolet fluctuations and improve the signal-to-noise ratio for the gluon observables. To implement this technique, the flowed gauge field,  $B_\mu(\tau, x)$ , is defined by

following the procedure [134],

$$\begin{aligned}\dot{B}_\mu &= D_\nu G_{\nu\mu}, & D_\mu &= \partial_\mu + [B_\mu, \cdot], \\ G_{\mu\nu} &= \partial_\mu B_\nu - \partial_\nu B_\mu + [B_\mu, B_\nu],\end{aligned}\tag{6.24}$$

where the flowed gauge field is subjected to the boundary condition  $B_\mu(\tau = 0, x) = A_\mu(x)$ . Here  $\tau$  is the flow time and differentiation with respect to  $\tau$  is abbreviated by a dot. The flow equation of the gauge field is a diffusion equation and the evolution operator in the momentum space acts as a UV regulator for  $\tau > 0$ . As a result, the gradient flow exponentially suppresses the UV field fluctuations, which corresponds to smearing out the original degrees of freedom in the coordinate space. The operators constructed using the flowed gauge fields with the positive flow time are expected to recover the correct physics at flow times smaller than the hadronic scale.

On the lattice, the gradient flow is implemented by defining the flowed link variable,  $V_\mu(\tau, n)$  as [134]

$$\dot{V}_\mu(\tau, n) = -g_0^2 \{ \partial_{n,\mu} S(V_\mu(\tau, n)) \} V_\mu(\tau, n),\tag{6.25}$$

where  $g_0$  is the bare coupling,  $S(V_\mu(\tau, n))$  is the flowed action,  $V_\mu(\tau = 0, n)$  has the boundary condition of being equal to the link variable,  $U_\mu(n)$ , and  $\partial_{n,\mu}$  stands for the natural  $\mathfrak{su}(3)$ -valued differential operator with respect to  $V_\mu(\tau, n)$ .

The Lie algebra  $\mathfrak{su}(3)$  of  $SU(3)$  is identified with the linear space of all the anti-hermitian traceless  $3 \times 3$  matrices. With respect to a basis  $T^a$ ,  $a = 1, 2, \dots, 8$  of such matrices, the elements  $X \in \mathfrak{su}(3)$  are given by  $X = X^a T^a$  with real components  $X^a$ , while the repeated group indices are summed over. On the lattice, the link differential operators acting on a function,  $f(U)$  of the gauge field are

$$\partial_{n,\mu}^a f(U) = \left. \frac{d}{ds} f(e^{sX} U) \right|_{s=0}, \quad X(y, \nu) = \begin{cases} T^a, & \text{if } (y, \nu) = (n, \mu), \\ 0, & \text{otherwise.} \end{cases} \quad (6.26)$$

The combination,  $\partial_{n,\mu} f(U) = T^a \partial_{n,\mu}^a f(U)$  is basis-independent. The action,  $S(V_\mu(\tau, n))$  is a monotonically decreasing function of  $\tau$ , and the gradient flow corresponds to a continuous stout-link smearing procedure [98].

Unimproved Wilson flow is used to calculate the gluonic currents with the flow times from  $\tau = a^2$  to  $\tau = 3.8a^2$ . The double ratio of Eq. (6.10) is constructed using the flowed matrix elements, which further reduces the UV fluctuations and suppresses the flow time dependence. The residual  $\tau$ -dependence is removed by fitting the flowed reduced matrix elements to an appropriate functional form which, in turn, gives the reduced pseudo-ITD at the zero flow time.

### 6.2.3 Nucleon Two-point Correlator

To construct the nucleon two-point correlators that enter into the calculation of the gluon PDF, distillation [96] is used as the quark-smearing technique. In motion, to increase the overlap of the interpolating operators onto the low-lying states, momentum smearing [101] is applied.

For the nucleon at rest on the lattice, only interpolating operators within the irrep.  $G_{1g}$  need be considered, because the states with continuum spin  $\frac{1}{2}$ , such as the ground state nucleon, are subduced onto this irrep. At the nonzero spatial momenta, the  $O_h^D$  group breaks further into little groups that depend on the direction of the boost. Only boosts along the  $z$  direction are considered in this calculation, so the associated little group is the order-16 dicyclic group or  $\text{Dic}_4$ .

The construction of the operators for the states at rest is discussed in section 5.1.

The choice of the interpolators for the nucleon at rest are tabulated as the first row in Table 6.1, using the spectroscopic notation described in section 5.1. For the construction of the three-point correlators needed for the unpolarized gluon distributions, the sum of the spin =  $+\frac{1}{2}$  and spin =  $-\frac{1}{2}$  nucleon two-point correlators are taken.

For the case of the correlation functions at the nonzero spatial momentum, parity is no longer a good quantum number and the operators are classified according to their helicity. Therefore the operators corresponding both to higher spin, and to negative parity are included in the basis within the little group  $\text{Dic}_4$ . The direction of the momenta is also chosen to be in the same direction of the polarization to ensure longitudinal polarization. The unpolarized gluon PDF is accessed by taking the sum of helicity =  $+\frac{1}{2}$  and helicity =  $-\frac{1}{2}$  nucleon two-point correlators. The choice of the interpolators is tabulated as the second row in Table 6.1.

Spatial momentum	Interpolators
$p = 0$	$N^2S_S \frac{1}{2}^+$ , $N^2S_M \frac{1}{2}^+$ , $N^4D_M \frac{1}{2}^+$ , $N^2P_A \frac{1}{2}^+$ , $N^4P_M^* \frac{1}{2}^+$ , $N^2P_M^* \frac{1}{2}^+$
$p \neq 0$	$N^2P_M \frac{1}{2}^-$ , $N^2P_M \frac{3}{2}^-$ , $N^4P_M \frac{1}{2}^-$ , $N^4P_M \frac{3}{2}^-$ , $N^4P_M \frac{5}{2}^-$ , $N^2S_S \frac{1}{2}^+$ , $N^2S_M \frac{1}{2}^+$ , $N^2P_M^* \frac{1}{2}^+$ , $N^4P_M^* \frac{1}{2}^+$

TABLE 6.1: Nucleon interpolators used in the calculation to construct the two-point correlators. The interpolators with asterisk (\*) on them are hybrid in nature.

## 6.3 Variational Analysis

To check whether the two-point correlators give the expected results, the associated principal correlators are investigated and the energy spectra are extracted from them by performing variational analyses for the nucleon at rest in the  $G_{1g}$  channel and for all the boosted frames in the  $\text{Dic}_4$  little group with the interpolators in Table 6.1.

In the fitting procedure, the principal correlators are required to be dominated by the leading exponential. Thus, in each of the fits,  $t_0$  is chosen such that an acceptable  $\chi^2/\text{d.o.f.}$  is obtained, that the value of  $A_n$  is small, typically less than 0.1 for each principal correlator.

In Figure 6.2 and 6.3, fits to the leading principal correlators for the nucleon subduced onto the little group  $\text{Dic}_4$  for  $p = 2 \times \frac{2\pi}{aL} = 0.82$  GeV, and  $p = 6 \times \frac{2\pi}{aL} = 2.46$  GeV are shown respectively. For each panel, the blue band is the reconstruction from the fitted parameters. The approach of the plateaux close to unity at large times is indicative of the small value of  $A_n$  in the fits, and the small contribution of the other states to each principal correlator.

In Figure 6.4, the ground state nucleon energy extracted using the variational analysis is plotted with respect to the spatial momentum, together with the expectations from the continuum dispersion relation

$$E_0(p) = \sqrt{E_0^2(0) + |p|^2}. \quad (6.27)$$

Here, the black points are the states at the lower momenta where momentum smearing is not implemented, and the red points are the states where momentum smearing is implemented as described in section 4.2. All the states are in excellent agreement with the continuum dispersion relation, the solid green line suggesting that at the lower momenta, the interpolating operators have significant overlap onto the ground state of the nucleon.

At the higher momenta, adding a phase to the distillation eigenvectors with  $\zeta = 2\frac{2\pi}{L}$  results in a significant increase in the overlap of the interpolators onto the lowest-lying states in motion.

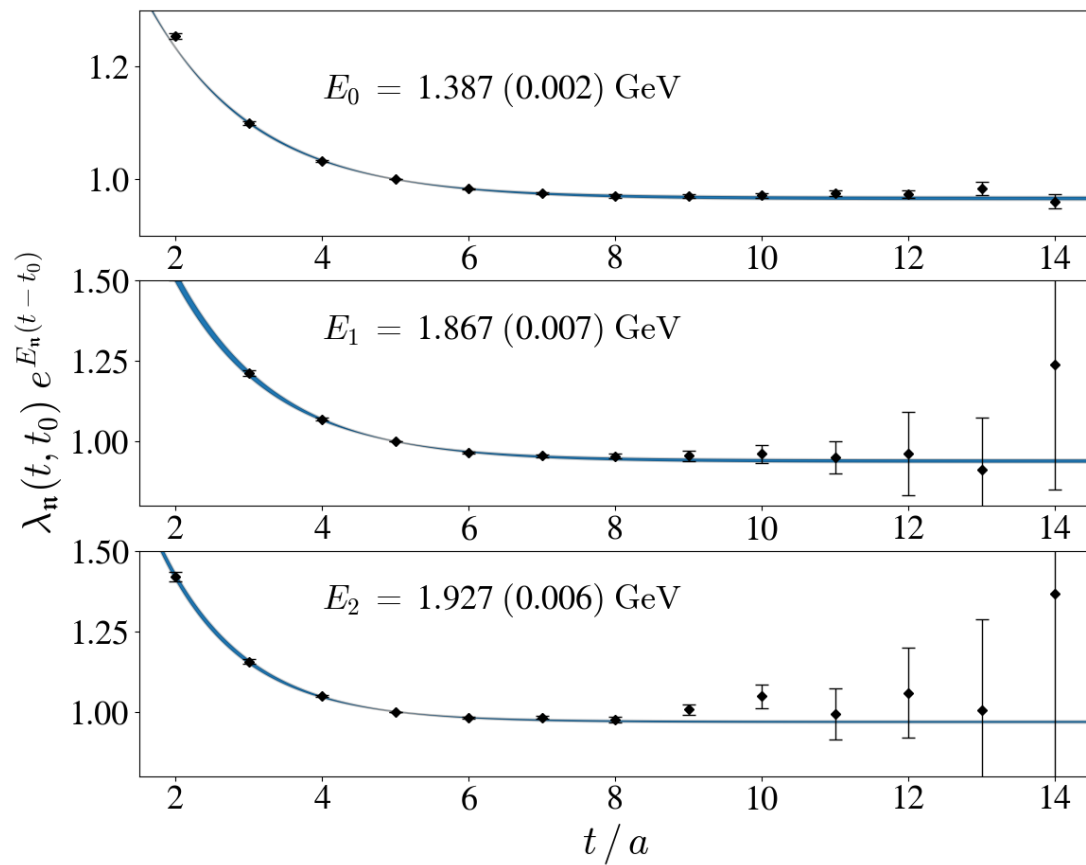


FIG. 6.2: Fits to the principal correlators for the nucleon with  $p = 2 \times \frac{2\pi}{aL} = 0.82$  GeV, subdued onto the little group,  $\text{Dic}_4$ , on the ensemble  $a094m358$ , for  $t_0 = 5$ . The plots show  $\lambda_n(t, t_0) e^{E_n(t-t_0)}$  data on the y axes and the lattice time slices on the x axes; the blue bands are the two-exponential fits as described in the text. The top, middle and bottom panels show the principal correlators for the ground state, the first excited state and the second excited state respectively. In each panel, the energy corresponding to the leading exponential state is labelled by  $E_n$ .

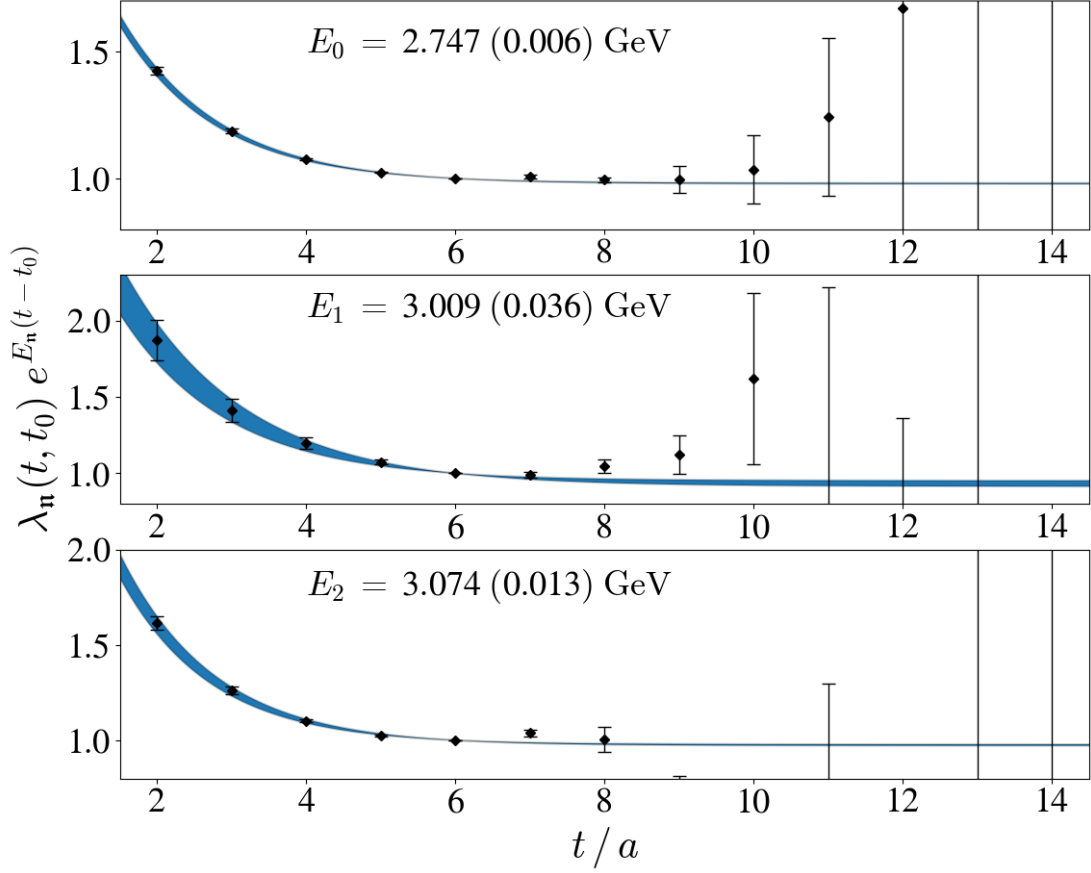


FIG. 6.3: Fits to the principal correlators for the nucleon with  $p = 6 \times \frac{2\pi}{aL} = 2.46 \text{ GeV}$ , subdued onto the little group,  $\text{Dic}_4$ , on the ensemble  $a094m358$ , for  $t_0 = 6$ . The plots show  $\lambda_n(t, t_0) e^{E_n(t-t_0)}$  data on the y axes and the lattice time slices on the x axes; the blue bands are the two-exponential fits as described in the text. The top, middle and bottom panels show the principal correlators for the ground state, the first excited state and the second excited state respectively. In each panel, the energy corresponding to the leading exponential state is labelled by  $E_n$ .

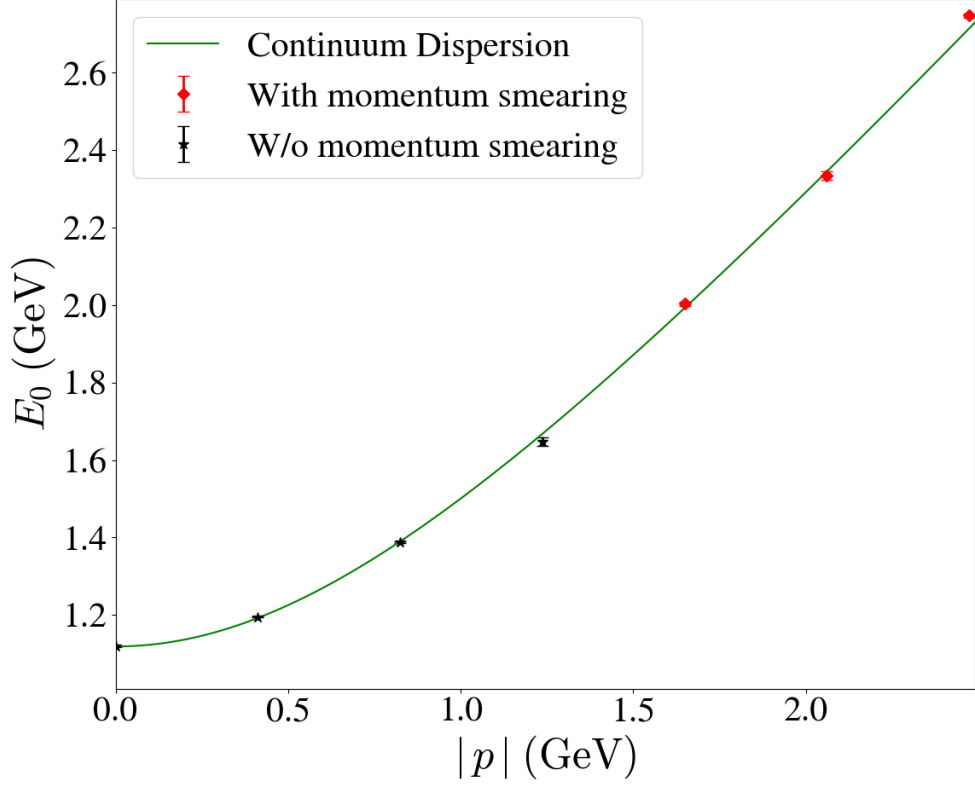


FIG. 6.4: The ground state nucleon dispersion relation on the ensemble  $a094m358$ , the solid green line being the continuum dispersion relation. Energies without phasing are in black and energies with phasing are in red.

## 6.4 Matrix Element Extraction

### 6.4.1 Three-point Correlator

The matrix elements are calculated by first computing the three-point correlators by inserting the gluonic currents between the source and the sink of the two-point correlators.

The three-point correlator can be expressed as

$$\langle C_{3pt}(t, t_g) \rangle = \langle 0 | \mathcal{T} \{ \mathcal{O}_N(t) O_g(t_g) \bar{\mathcal{O}}_N(0) \} | 0 \rangle, \quad (6.28)$$

where  $\overline{\mathcal{O}}_N$  and  $\mathcal{O}_N$  are the interpolators and  $t$  is the source-sink separation. The  $\langle \dots \rangle$  on the left indicates the ensemble average and  $\mathcal{T}\{\dots\}$  stands for the time-ordered product. The three-point correlator can be rewritten as

$$C_{3pt}(t, t_g) = \left( C_{2pt}(t) - \langle C_{2pt}(t) \rangle \right) \left( O_g(t_g) - \langle O_g(t_g) \rangle \right), \quad (6.29)$$

where  $C_{2pt}(t)$  is the nucleon two-point correlator with the source-sink separation  $t$  in lattice units and  $t_g$  is the time slice on which the gluonic current is inserted.

### 6.4.2 sGEVP Method

To extract the matrix elements from the three-point correlators, a combination of the summation method [137] and the GEVP [8] method, the sGEVP method [99, 138] is implemented. In this technique, the summed three-point correlators are constructed by summing over the three-point correlators that have the same source-sink separations, but the gluonic currents inserted at different time slices between the source and sink. To avoid contact contributions, the three-point correlators which have gluonic currents inserted at the source time slice or sink time slice themselves, are excluded. In this way, the summed three-point correlators are calculated for different interpolator combinations at the source and the sink:

$$C_{3pt}^s(t_{src}, t_{snk}) = \sum_{t_g=(t_{src}+1)}^{(t_{snk}-1)} C_{2pt}(t_{src}, t_{snk}) O_g(t_g). \quad (6.30)$$

Here,  $t_{src}$  and  $t_{snk}$  are the lattice time slices where the source and the sink are, respectively. The label “s” stands for summed. To illustrate the sGEVP method, let us

consider two sets of interpolators,

$$\begin{aligned}\mathcal{O}_i(t) &= \mathcal{O}_i^{(A)}(t), \quad i = 1, 2, \dots, N_n \\ \mathcal{O}_{i+N_n}(t) &= \mathcal{O}_i^{(B)}(t), \quad i = 1, 2, \dots, N_n.\end{aligned}\tag{6.31}$$

Let us define a small parameter  $\epsilon = \exp(-(E_{N_n+1} - E_{N_n})t_0)$  which becomes small for large  $t_0$ . Expanding the path integral to the first order in  $\epsilon$ , the combined  $2N_n \times 2N_n$  matrix of the two-point correlators from these interpolators can be written in the simple block structure

$$C(t, \epsilon) = \begin{bmatrix} C_{2pt}(t) & \epsilon C_{3pt}^s(t) \\ \epsilon C_{3pt}^{s\dagger}(t) & C_{2pt}(t) \end{bmatrix} + \mathcal{O}(\epsilon^2).\tag{6.32}$$

Here, by setting  $C^{(A)} = C^{(B)} = C_{2pt}$ , the  $2N_n \times 2N_n$  GEVP equation

$$C(t, \epsilon)\rho_n(t, t_0, \epsilon) = \lambda_n(t, t_0, \epsilon)C(t_0, \epsilon)\rho_n(t, t_0, \epsilon),\tag{6.33}$$

can be rewritten into its components

$$\left[ C_{2pt}(t) \pm \epsilon C_{3pt}^s(t) \right] u_n^\pm(t, t_0, \epsilon) = \lambda_n^\pm(t, t_0, \epsilon) \left[ C_{2pt}(t_0) \pm \epsilon C_{3pt}^s(t_0) \right] u_n^\pm(t, t_0, \epsilon),\tag{6.34}$$

where

$$\rho_n^\pm = \frac{1}{\sqrt{2}} \begin{pmatrix} u_n^\pm \\ \pm u_n^\pm \end{pmatrix}.\tag{6.35}$$

Taking the small  $\epsilon$  limit, the summed three-point correlators can be treated as a perturbation. By expanding the GEVP equation in  $\epsilon$ , the effective matrix element can be expressed as [99]

$$\mathcal{M}_{\text{nn}}^{\text{eff},s}(t, t_0) = -\partial_t \left\{ \frac{\left| \left( u_{\text{n}}, [C_{3pt}^s(t)\lambda_{\text{n}}^{-1}(t, t_0) - C_{3pt}^s(t_0)]u_{\text{n}} \right) \right|}{\left( u_{\text{n}}, C_{2pt}(t_0)u_{\text{n}} \right)} \right\}. \quad (6.36)$$

Here,

$$\left( u_{\text{n}}, C_{2pt}(t_0)u_{\text{n}} \right) \equiv u_{\text{n}}^\dagger \left( C_{2pt}(t_0)u_{\text{n}} \right). \quad (6.37)$$

In the small  $\epsilon$  limit,  $u_{\text{n}}$  and  $\lambda_{\text{n}}(t, t_0)$  become the generalized eigenvector and the principal correlator of the generalized eigenvalue problem for the two-point correlator matrix:

$$C_{2pt}(t) u_{\text{n}}(t, t_0) = \lambda_{\text{n}}(t, t_0) C_{2pt}(t_0) u_{\text{n}}(t, t_0). \quad (6.38)$$

The generalized eigenvector,  $u_{\text{n}}$ , satisfies the orthogonality condition

$$u_{\text{n}'}^\dagger(t, t_0) C_{2pt}(t_0) u_{\text{n}}(t, t_0) = \delta_{\text{nn}'}. \quad (6.39)$$

In the GEVP method, the two-point correlator matrix is rotated to be diagonal in the generalized eigenvector space, eliminating the excited state contributions significantly. In the sGEVP method, the summed three-point correlator matrix is rotated with the same angle by which the two-point correlator matrix is rotated to be diagonal. This rotation suppresses the excited state contributions in the summed three-point correlators too. As the orthogonality of the generalized eigenvectors are defined with respect to  $t = t_0$ , the ratio of the  $C_{3pt}(t)$  matrix to the principal correlator matrix,  $\lambda_{\text{n}}(t, t_0)$  is ill-defined at  $t = t_0$ . To avoid this issue,  $C_{3pt}(t_0)$  is subtracted from the ratio for all  $t$ .

From degenerate perturbation theory, it is known that the matrix element is the first derivative of the energy with respect to the perturbation taken in the  $\epsilon \rightarrow 0$  limit. The

effective energy is given in terms of the principal correlator [139],

$$E_n^{\text{eff}}(t, t_0, \epsilon) = -\partial_t \log(\lambda_n(t, t_0, \epsilon)). \quad (6.40)$$

So, the effective matrix element can be expressed as

$$\begin{aligned} \mathcal{M}_{\text{nn}}^{\text{eff},s}(t, t_0) &\equiv \left. \frac{d}{d\epsilon} E_n^{\text{eff}}(t, t_0, \epsilon) \right|_{\epsilon=0} \\ &= \mathcal{M}_{\text{nn}} + O(\Delta E_{N_n+1,n} t \exp(-\Delta E_{N_n+1,n} t)). \end{aligned} \quad (6.41)$$

Here,  $N_n$  is the total number of states. Now, in GEVP method, if the matrix element have a current insertion such that the temporal separation between the source and the current insertion,  $t_1$  and the temporal separation between the source and the current insertion,  $t_2$  are the same, i.e.  $t_1 = t_2$ , then the the systematic error for matrix elements decays as  $O\left(e^{-\frac{\Delta E t}{2}}\right)$  where  $t$  is the source-sink separation [99]. On the other hand, for the sGEVP method, the systematic error decays as  $O(\Delta E t e^{-\Delta E t})$ . Comparing these two decays it can be seen that for the sGEVP method, the systematic error decays much faster than it decays for the GEVP method for all  $t$ . Especially in the asymptotic region  $\Delta E t \gg 1$ , the sGEVP method requires approximately half the total temporal separation for the same size systematic correction compared with the GEVP method. This allows one to access the matrix elements at a much smaller temporal separation than would be possible in the GEVP method. This is crucial for hadron structure calculations since the signals tend to be heavily contaminated by noise as the temporal separation is increased. In fact, the gluonic matrix elements contain more noise compared to matrix elements in other hadronic structure calculations. The sGEVP method utilizes the lowest-lying spectra, conveniently calculated using distillation, by rotating the three-point correlator matrix by a suitable angle, removing much of the excited state contaminations, and therefore performs better

than the summation method [137], which involves only the ground state nucleon.

In principle, increasing the number of states,  $N_n$ , in the sGEVP analysis should lead to a larger  $\Delta E$ , which enables the matrix elements to be extracted from even smaller temporal separations. This, however, also increases the computational cost, because the  $N_n \times N_n$  correlator matrix needs to be constructed, and makes solving the GEVP for the nucleon two-point correlator matrix more challenging.

### 6.4.3 Bare Matrix Elements

The calculation of the gluon PDF involves the extraction of the matrix elements for the gluonic currents flowed by multiple flow times, multiple nucleon momenta and multiple separations between the gluonic fields. The calculation is performed for the flow times,  $\tau/a^2 = 1.0, 1.4, 1.8, 2.2, 2.6, 3.0, 3.4$  and  $3.8$ . For each flow time, the matrix elements for the ground state of the nucleon are calculated for the lattice spatial momenta,  $p = \frac{2\pi l}{aL}$  where  $l = 0$  to  $6$ , and for the field separations,  $z = sa$  where  $s = 0$  to  $6$ , and  $a$  is the lattice spacing. The effective matrix elements  $\mathcal{M}^{\text{eff},s}(t, \tau, p, z)$  are extracted for each flow time, nucleon momentum and field separation using Eq. (6.36).

To choose the optimal set of interpolators for the construction of the matrix elements, the operator overlaps of the nucleon ground state are examined. The interpolators which have significant overlap onto the ground state should be crucial for the sGEVP method. In Figure 6.5, the overlap distributions of the operators onto the ground state of the nucleon for the momenta,  $p = \{1, 5\} \times \frac{2\pi}{aL} = 0.41 \text{ GeV}, 2.05 \text{ GeV}$  are shown.

From Figure 6.5 it's evident that the two hybrid-type interpolators have large overlaps onto the ground state, along with the local interpolator with the zero orbital angular momentum. This shows that the ground state nucleon has a significant hybrid component in addition to the predominant valence qqq component. Three sets of interpolators are

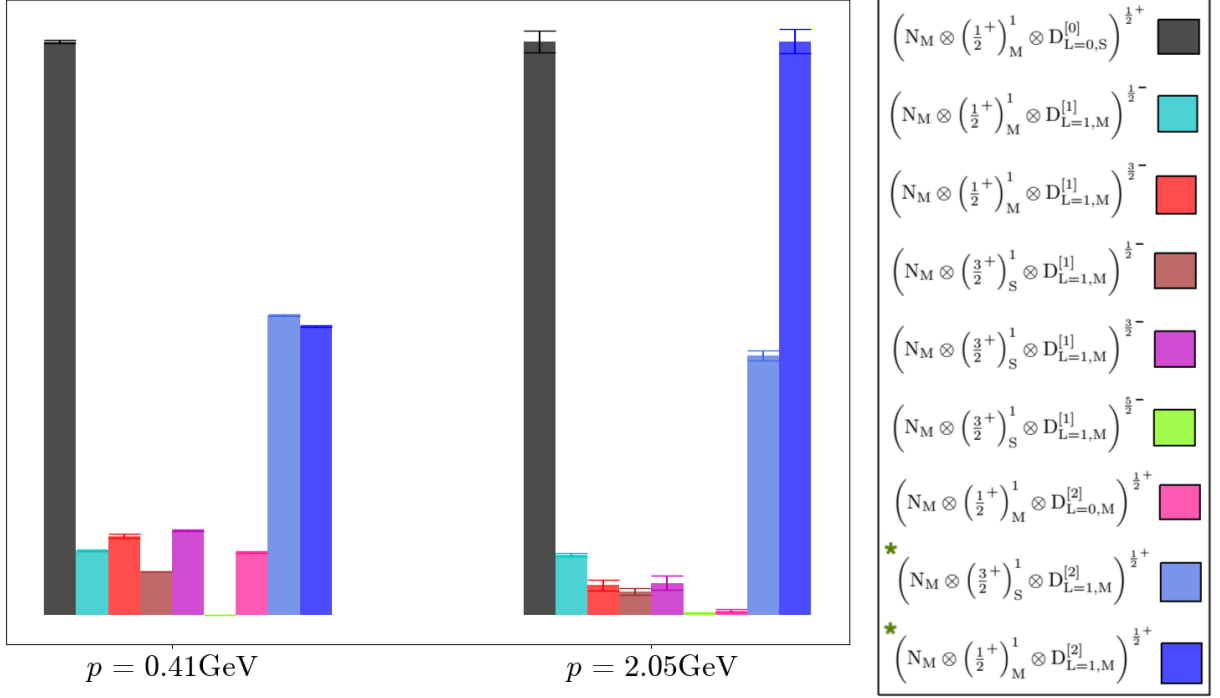


FIG. 6.5: Overlap of the operators onto the ground state of the nucleon for different momenta. The overlap distribution on the left is for the nucleon momentum,  $p = 1 \times \frac{2\pi}{aL} = 0.41\text{GeV}$ , and on the right is for the nucleon momentum,  $p = 5 \times \frac{2\pi}{aL} = 2.05\text{GeV}$ . The asterisks denote the hybrid-type interpolators.

formed, and the associated matrix elements are calculated and compared. In the first set of interpolators, all the interpolators in Table 6.1 are used in the construction of the matrix elements. This set is labeled as “model-A”. Another set of interpolators is constructed including the local interpolator and the two hybrid interpolators, labeled as “model-B”. And in “model-C”, only the local interpolator is considered.

In Figure 6.6, a comparison among the matrix elements calculated from these models is shown for two different flow times, field separations, and nucleon momenta. The matrix elements from model-A and model-B closely follow the same pattern. This is expected as from Figure 6.5, it is clear that the ground state of the nucleon is mostly composed of the interpolators in model-B. The interpolators that are not included in model-B, but exist in model-A, have small contributions to the ground state. A little deviation of the matrix

elements from model-B can be seen at higher nucleon momentum and field separation, due to the inclusion of more interpolators in model-A. The matrix elements from model-C reach plateaux of lower values, at higher source-sink separations, as there is only the local interpolator in this model, making the quantity,  $\Delta E_{N_n+1,n}$  of Eq. (6.41) quite small, resulting in only the partial removal of the excited state contributions comparing with the other two models.

Model	Interpolators
A	All the interpolators from Table 6.1
B	$N^2S_S \frac{1}{2}^+$ , $N^4P_M^* \frac{1}{2}^+$ , $N^2P_M^* \frac{1}{2}^+$
C	$N^2S_S \frac{1}{2}^+$

TABLE 6.2: Nucleon interpolators of the models to construct the matrix elements. The interpolators with asterisk (\*) on them are hybrid in nature.

Although model-B gives a quite satisfactory result, the most computationally expensive part of the calculation, the construction of the nucleon two-point correlators is already done for the interpolators of model-A. So, the calculation of the unpolarized gluon PDF is done using the matrix elements calculated from model-A. For future projects, where the calculation would be done with higher statistics, the computational cost may be lowered by constructing the nucleon two-point correlators for the interpolators from model-B only, without compromising the quality of the matrix elements.

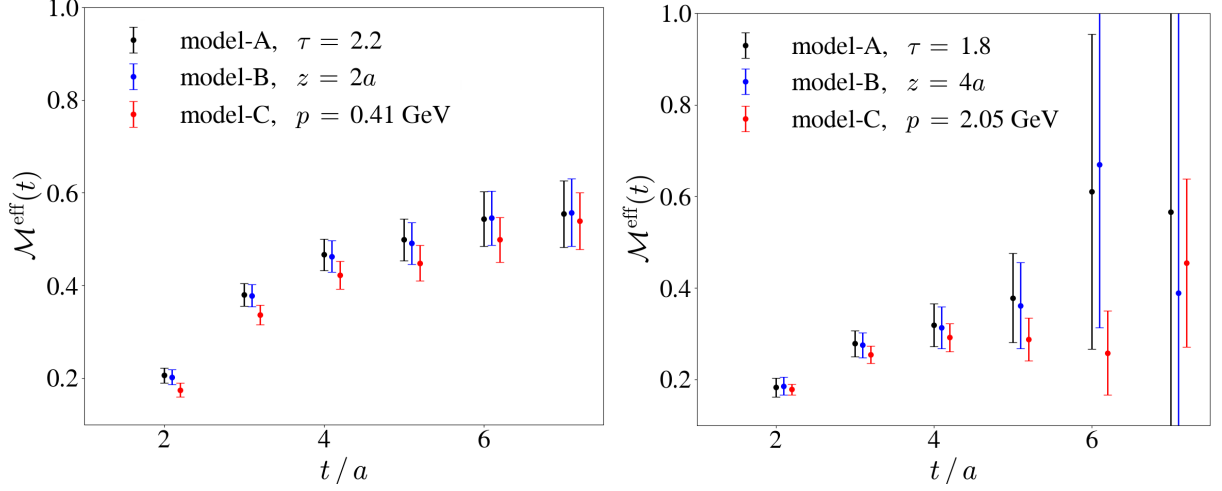


FIG. 6.6: Comparing the matrix elements calculated using the sGEVP method for different sets of interpolators. Model-A consists of all the interpolators in Table 6.1, model-B consists of the local interpolator and the two hybrid interpolators, and model-C consists of only the local interpolator. The panel on the left shows the matrix elements for the flow time,  $\tau = 2.2$  in lattice units, the field separation,  $z = 2a = 0.188$  fm and the nucleon momentum,  $p = 1 \times \frac{2\pi}{aL} = 0.41$  GeV. On the right panel, there are the matrix elements for the flow time,  $\tau = 1.8$  in lattice units, the field separation,  $z = 4a = 0.376$  fm and the nucleon momentum,  $p = 5 \times \frac{2\pi}{aL} = 2.05$  GeV. The matrix elements of model-B and model-C are shifted rightward for better visualization.

#### 6.4.4 Autocorrelation of the Matrix Elements

To check whether the bare matrix elements extracted from the different gauge configurations are correlated or not, the associated integrated autocorrelation time is calculated for each source-sink separation. The integrated autocorrelation time is a measure of how efficiently the Monte Carlo algorithm can be implemented to calculate the desired quantity. In this calculation, each gauge configuration is separated from the next gauge configuration by 10 HMC trajectories. Calculation of the integrated autocorrelation time for a given quantity will indicate whether this separation of 10 HMC trajectories is sufficient to remove autocorrelations between configurations for that quantity. The method of the calculation follows the procedure described in [140].

Let us assume that the object is to be calculated on the lattice is

$$F \equiv f(A_1, A_2, A_3, \dots) \equiv f(A_\alpha). \quad (6.42)$$

where  $A_1, A_2, A_3, \dots$  are the primary observables. The Monte Carlo estimate of the primary observables are  $a_\alpha^i$ , and for each observable, there are  $i = 1, 2, 3, \dots, N_u$  successive estimates separated by a fixed number of HMC updates. It is assumed that the Markov chain has been equilibrated before recording data beginning with  $i = 1$ . The autocorrelation function,  $\Gamma_{\alpha\beta}$  can be defined as [141]

$$\Gamma_{\alpha\beta}(r) = \langle (a_\alpha^i - A_\alpha)(a_\beta^{i+r} - A_\beta) \rangle. \quad (6.43)$$

This autocorrelation function correlates the deviation of the  $i$ 'th estimate for  $A_\alpha$  with the deviation for the variable  $\beta$  after performing  $r \geq 0$  updates. The  $\langle \dots \rangle$  indicates the ensemble average. It is useful to define,  $\Gamma_{\alpha\beta}(-r) = \Gamma_{\beta\alpha}(r)$ . Now, the primary observable,  $A_\alpha$  can be estimated as

$$\bar{a}_\alpha = \frac{1}{N_u} \sum_{i=1}^{N_u} a_\alpha^i. \quad (6.44)$$

Let us consider the estimator for  $F$ ,  $\bar{F} = f(\bar{a}_\alpha)$ . If the estimates of the primary observables are accurate enough, then  $\bar{F}$  can be expanded in a Taylor series,

$$\bar{F} = F + \sum_{\alpha} f_{\alpha} \bar{\delta}_{\alpha} + \frac{1}{2} \sum_{\alpha\beta} f_{\alpha\beta} \bar{\delta}_{\alpha} \bar{\delta}_{\beta} + \dots, \quad (6.45)$$

where

$$f_{\alpha} = \frac{\partial f}{\partial A_{\alpha}}, \quad f_{\alpha\beta} = \frac{\partial^2 f}{\partial A_{\alpha} \partial A_{\beta}}, \quad \bar{\delta}_{\alpha} = \bar{a}_{\alpha} - A_{\alpha}. \quad (6.46)$$

The error  $\sigma_F$  is to leading order given by

$$\sigma_F^2 = \langle (\bar{F} - F)^2 \rangle \simeq \frac{1}{N_u} C_F, \quad (6.47)$$

with

$$C_F = \sum_{\alpha\beta} f_\alpha f_\beta C_{\alpha\beta}, \quad C_{\alpha\beta} = \sum_{r=-\infty}^{\infty} \Gamma(r). \quad (6.48)$$

The expression of the error can be rewritten as

$$\sigma_F^2 = \frac{2\tau_{\text{int}}}{N_u} \nu_F, \quad (6.49)$$

where the variance for  $F$  disregarding autocorrelation is

$$\nu_F = \sum_{\alpha\beta} f_\alpha f_\beta \Gamma_{\alpha\beta}(0), \quad (6.50)$$

and the integrated autocorrelation time for  $F$  is

$$\tau_{\text{int}} = \frac{1}{2\nu_F} \sum_{r=-\infty}^{\infty} \sum_{\alpha\beta} f_\alpha f_\beta \Gamma_{\alpha\beta}(r). \quad (6.51)$$

In this calculation,  $\tau_{\text{int}}$  is calculated for the same primary observable setting  $\alpha = \beta$ . So, the integrated autocorrelation time becomes

$$\tau_{\text{int}} = \frac{1}{2\nu_F} \sum_{r=-\infty}^{\infty} \sum_{\alpha} f_\alpha f_\alpha \Gamma_{\alpha\alpha}(r). \quad (6.52)$$

In absence of autocorrelation,  $\Gamma_{\alpha\alpha}(r) \propto \delta_{r,0}$ . Under this condition, the integrated autocorrelation time becomes  $\tau_{\text{int}} = 0.5$ , and Eq. (6.49) becomes the standard error. For practical reasons, the sum over updates  $r$  is taken over a finite window. The summation window is to be chosen carefully. It has to be large for a small systematic error, but if it is set too large, terms with negligible signal but excessive noise would get included in the calculation.

In Figure 6.7, the integrated autocorrelation time for the bare matrix element at the

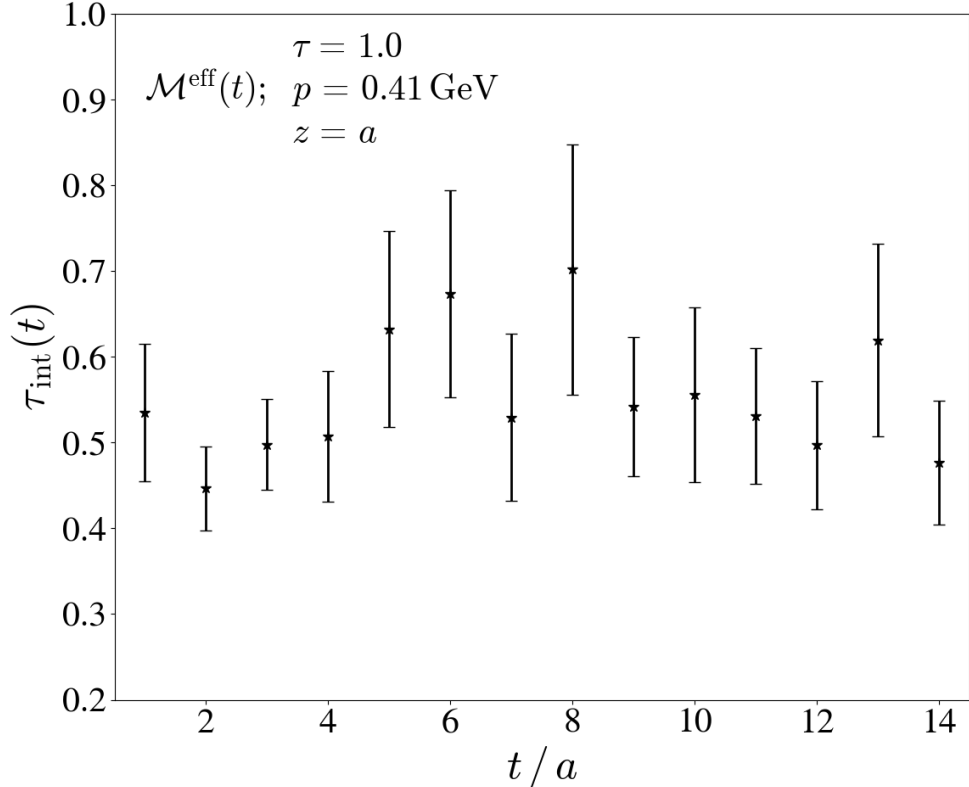


FIG. 6.7: The integrated autocorrelation time of the bare matrix elements calculated for each source-sink separations at the flow time = 1.0 in lattice units, for the field separation,  $z = a = 0.0.094$  fm and for the nucleon momentum,  $p = \frac{2\pi}{aL} = 0.41$  GeV.

flow time = 1.0 in lattice units, for the field separation,  $z = a = 0.0.094$  fm and for the nucleon momentum,  $p = \frac{2\pi}{aL} = 0.41$  GeV is shown for each source-sink separation. As can be seen,  $\tau_{\text{int}}(t)$  stays close to the value of 0.5 for all the source-sink separations indicating that autocorrelation among the bare matrix elements calculated on gauge configurations separated from the next configuration by 10 HMC trajectories is negligible.

### 6.4.5 Bayesian Analysis

The matrix elements are fitted to a suitable expression using the Bayesian analysis technique. The software package, XMBF [142, 143] is used to conduct the analysis. In the fitting procedure, for each fit parameter, a Gaussian distribution is constructed from

a given central value and a prior width. The prior is chosen randomly from the Gaussian distribution, and a simultaneous, fully correlated fit is conducted. The prior width is chosen big enough so that the influence of the priors on the parameters is negligible. The fit procedure minimizes a goodness-of-fit quantity,  $\chi^2$ ,

$$\chi^2 = \chi_{\text{data}}^2 + \chi_{\text{prior}}^2, \quad (6.53)$$

where  $\chi_{\text{data}}^2$  compares the input data with the reconstructed data using the randomly chosen prior, and  $\chi_{\text{prior}}^2$  compares the randomly chosen prior with the given central value and the prior width. Here

$$\chi_{\text{data}}^2 = \sum_{i,j} (\mathbb{C}^{-1})_{ij} [\bar{y}_i - f_i(\mathbf{a})] [\bar{y}_j - f_j(\mathbf{a})], \quad (6.54)$$

where the data correlation matrix is

$$\mathbb{C}_{ij} = \frac{1}{N_s(N_s - 1)} \sum_{s=1}^{N_s} (y_i^s - \bar{y}_i) (y_j^s - \bar{y}_j), \quad (6.55)$$

and  $y_i^s$  is the  $i$ th real valued observable from the  $s$ th statistically independent measurement, and  $N_s$  is the total number of measurements. The number of degrees of freedom is the number of observables less the number of parameters in the fit. The data are to be fitted to the smooth function,  $f_i(\mathbf{a})$ , with real valued parameters,  $a_1, a_2, \dots, a_P$ , and  $\bar{y}_i$  is the average of the  $i$ th observable,

$$\bar{y}_i = \frac{1}{N_s} \sum_{s=1}^{N_s} y_i^s. \quad (6.56)$$

And

$$\chi_{\text{prior}}^2 = \sum_P \frac{(a_P - \tilde{a}_P)^2}{\tilde{\sigma}_P^2}, \quad (6.57)$$

where  $\tilde{a}_P$  and  $\tilde{\sigma}_P^2$  are the input central value and the prior width respectively.

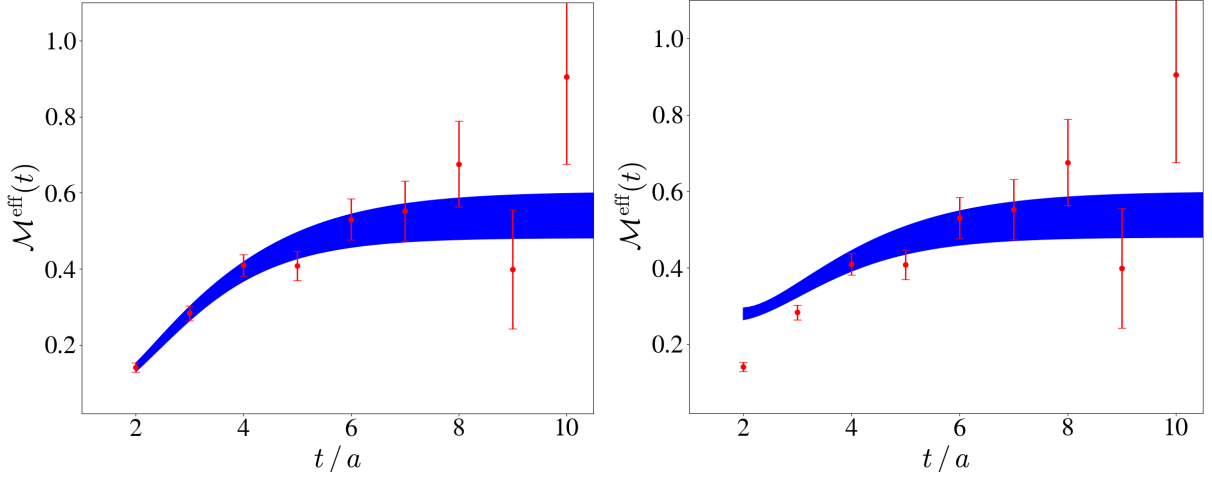


FIG. 6.8: Fitting the matrix elements with different fit expressions, with Eq. (6.58) on the left panel, and with Eq. (6.59) on the right panel. The matrix element shown here is at the flow time = 3.4 in lattice units, for the field separation,  $z = 3a = 0.282$  fm and the nucleon momentum,  $p = 2 \times \frac{2\pi}{aL} = 0.82$  GeV. The red points are the lattice data points and the blue bands are the reconstructions of the matrix elements from the fitted parameters.

According to the sGEVP method, the matrix elements are to be fitted using the functional form in Eq. (6.41), which can be written in simplified notation and arguments as

$$\mathcal{M}^{\text{eff}}(t) = A + B t \exp(-\Delta E t). \quad (6.58)$$

Here,  $A$  is the fitted matrix element to be extracted. The exponential term captures the contributions from the excited states. To check whether adding another exponential term, but without the source-sink separation multiplied by the exponential, would improve the fits, the fit results are compared between two fit expressions, one with a single exponential Eq. (6.58) and one with two exponentials Eq. (6.59).

$$\mathcal{M}^{\text{eff}}(t) = A + B t \exp(-\Delta E t) + C \exp(-\Delta E t). \quad (6.59)$$

In Figure 6.8, the matrix element at the flow time = 3.4 in lattice units, for the field separation,  $z = 3a = 0.282$  fm and the nucleon momentum,  $p = 2 \times \frac{2\pi}{aL} = 0.82$

GeV is shown with the fit expression, Eq. (6.58) on the left panel, and Eq. (6.59) on the right panel. Both the fit results yield plateaux at the same source-sink separation region, and fitted matrix elements with the similar values and uncertainty, and they have similar  $\chi^2/\text{d.o.f.}$ , but the reconstruction of the matrix element is poor for the right panel at the smaller source-sink separations. This is because the second exponential in Eq. (6.59) dies out for the larger source-sink separations, but becomes more prominent at the smaller source-sink separations. Therefore, it is preferable to use Eq. (6.58) as the fit expression for the extraction of the matrix elements. To perform the fit of Eq. (6.58) for a particular nucleon momentum,  $p$  the matrix element for  $z = 0$  is fitted first, and the corresponding fitted value of the parameter  $\Delta E$  determined. This value of  $\Delta E$  is then used to set the prior for the subsequent fits to the matrix elements for  $z > 0$  at that particular nucleon momentum. The prior width of  $\Delta E$  for  $z > 0$  is set to be three times larger than the uncertainty in  $\Delta E$ . A simultaneous and correlated fit is performed to the matrix elements for  $z = \{1, 2, 3, 4, 5, 6\} \times a = 0.094 \text{ fm}, 0.188 \text{ fm}, 0.282 \text{ fm}, 0.376 \text{ fm}, 0.470 \text{ fm}, 0.564 \text{ fm}$  respectively, for each nucleon momentum and each flow time,

$$\mathcal{M}^{\text{eff}}(t)_z = A_z + B_z t \exp(-\Delta E t), \quad (6.60)$$

where  $z = 1, 2, \dots, 6$  and the  $\Delta E$  is assumed to be the same for the matrix elements at a fixed nucleon momentum and flow time. This procedure is particularly helpful for a well-controlled fit to the large momentum matrix elements for which the signal-to-noise ratio is poor, especially at flow times  $\tau/a^2 < 1.6$ .

In Figure 6.9, the fits to the matrix elements for  $\tau/a^2 = 1.0$  and  $3.0$  are illustrated. Here, the fitted matrix elements are compared among the nucleon momenta,  $p = \{1, 6\} \times \frac{2\pi}{aL} = 0.41 \text{ GeV}, 2.46 \text{ GeV}$  respectively; and the field separations,  $z = \{0, 1, 6\} \times a = 0, 0.094 \text{ fm}, 0.564 \text{ fm}$  respectively. The fitted parameters are listed in Table 6.3. It can be seen

immediately that the  $\Delta E$  values determined for the nonzero field separations are almost identical compared to that obtained for the matrix elements at  $z = 0$  where no prior is assigned on the fit parameter  $\Delta E$ . This, along with the goodness-of-fit in the extraction of the matrix elements for the nonzero separations, indicates the validity of the fitting procedure.

From Figure 6.9 and the corresponding fit parameters in Table 6.3, it is clear the lattice data are described well by the fit procedure. The  $\chi^2/\text{d.o.f.}$  shows that the choice of the prior width for  $\Delta E$  at  $z > 0$  is an appropriate one. From Figure 6.9, it can be noticed that the matrix elements for  $z = 6a = 0.564$  fm, have a flat behavior as a function of the source-sink separations. This can be understood from the smallness of  $B$ -parameters listed in Table 6.3, with relatively larger uncertainties.

The nucleon two-point correlators have quite good signal-to-noise ratios up to the source-sink separation,  $t = 9a = 0.846$  fm at  $p = 6 \times \frac{2\pi}{aL} = 2.46$  GeV, as can be seen from Figure 6.3. Figure 6.9 shows, however, that the matrix elements lose almost any statistical signal around the source-sink separation  $t = 6a = 0.564$  fm, which is expected, as the nucleon momentum increases. As shown in [144], the optimized interpolators reduce the excited state contributions allowing one to start the fit at significantly earlier source-sink separations. It can be seen in Figure 6.9 where the matrix elements for  $p = 1 \times \frac{2\pi}{aL} = 0.41$  GeV reach a plateau around the source-sink separation,  $t = 4a = 0.376$  fm.

$\tau/a^2$	$p$ (GeV)	$z$ ( $a$ )	$\nu$	$A$	$B$	$\Delta E$	$\chi^2/\text{d.o.f.}$
1.0	0.41	0	0.00	0.62(4)	-2.69(79)	1.41(18)	0.53
1.0	0.41	1	0.20	0.60(3)	-2.35(50)	1.40(13)	0.77
1.0	0.41	6	1.18	0.13(2)	-0.14(7)	1.40(13)	0.77
1.0	2.46	0	0.00	0.94(12)	-2.56(83)	1.15(25)	0.62

1.0	2.46	1	1.18	0.85(8)	-2.23(28)	1.22(12)	0.29
1.0	2.46	6	7.07	0.09(2)	0.07(13)	1.22(12)	0.29
3.0	0.41	0	0.00	0.62(4)	-1.80(13)	1.03(5)	0.35
3.0	0.41	1	0.20	0.60(2)	-1.68(8)	1.02(4)	0.31
3.0	0.41	6	1.18	0.19(1)	-0.39(4)	1.02(4)	0.31
3.0	2.46	0	0.00	0.91(11)	-2.16(20)	0.91(10)	0.29
3.0	2.46	1	1.18	0.83(7)	-1.90(17)	0.93(7)	0.22
3.0	2.46	6	7.07	0.18(3)	-0.28(13)	0.93(7)	0.22

TABLE 6.3: The fitted parameters and the goodness-of-fits for the matrix elements shown in Figure 6.9. For a particular flow time and nucleon momentum, the matrix elements at  $z = 0$  are fitted first; the information regarding the fit parameter  $\Delta E$  from this fit is used to set the prior for  $\Delta E$  in a simultaneous correlated fit for the matrix elements of all the nonzero separations.

The lattice QCD calculations of the gluonic observables are, in general, much noisier than the quark matrix elements. Measures of the goodness-of-fits do not necessarily reflect all the systematic uncertainties in the extractions of the fit parameters  $A$ ,  $B$ , and  $\Delta E$ . However, by using  $N_n$  interpolators within a variational approach, the Hilbert space is sampled more thoroughly in a particular irrep. in finite volume. This has been proven successful in nucleon structure calculation in [100]. The crucial insight is that projecting to the definite finite volume states via the variational solutions allows taking advantage of the orthogonality of the states in the Hilbert space [138]. There are clearly residual excited state contributions present, so constructing the ideal basis is unrealistic. However, a significant improvement is achieved by incorporating a moderate number of interpolators and applying distillation, one of the most computationally cost-effective methods for

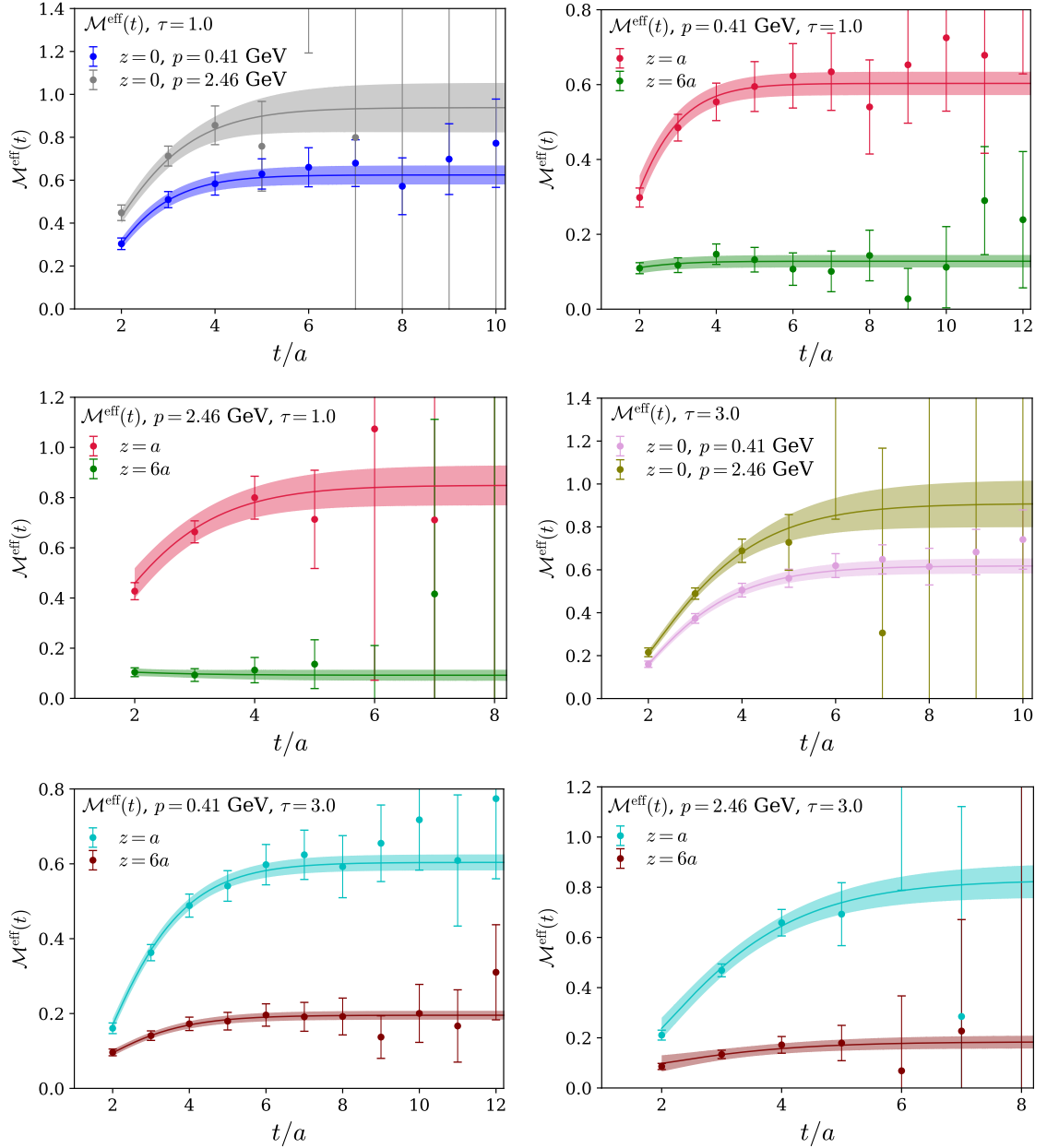


FIG. 6.9: Extraction of the matrix elements using the sGEVP method for different flow times, nucleon momenta, and field separations on the ensemble  $a094m358$ . The bands are the fits described in the text. The left panel at the top row shows the comparison between the matrix elements for the nucleon momenta,  $p = \{1, 6\} \times \frac{2\pi}{aL} = 0.41$  GeV, 2.46 GeV respectively, at zero field separation for the flow time,  $\tau = 1.0$  in lattice units. The top-right panel compares between the matrix elements for the nucleon momenta,  $p = 1 \times \frac{2\pi}{aL} = 0.41$  GeV and the field separations,  $z = \{1, 6\} \times a = 0.094$  fm, 0.564 fm respectively for the same flow time. The middle-left panel does the same comparison as done in the top right panel, but for the nucleon momenta,  $p = 6 \times \frac{2\pi}{aL} = 2.46$  GeV for the same flow time. In the middle-right panel, the bottom-left panel and the bottom-right panel, the comparisons between the matrix elements are shown similar to that of the top-left, the top-right and the middle-left panel respectively, but at the flow time,  $\tau = 3.0$  in lattice units.

implementing a large number of interpolators. Therefore, by adding multiple interpolators, the determination of  $A$ ,  $B$ , and  $\Delta E$  are improved systematically in this calculation. Further investigation with larger statistics will be necessary for a complete estimate of all the systematic uncertainties associated with the excited state contaminations at the large nucleon momenta.

### 6.4.6 Reduced Matrix Elements and Zero Flow Time Extrapolation

From the bare matrix elements, the reduced matrix elements are calculated using the double ratio in Eq. (6.10) for different flow times, nucleon momenta, and field separations. The reduced matrix elements for eight different values of  $\tau/a^2$  are presented in Figure 6.10-6.17. The higher twist contributions, the discretization effects, and the flow time dependence are expected to be minimized through this double ratio.

From the reduced matrix elements at different flow times, the reduced pseudo-ITD distribution is calculated by extrapolating to zero flow time. At fixed values of field separation,  $z$ , and nucleon momentum,  $p$ , the  $\tau$ -dependence is found to be fitted best by a linear form,  $\mathfrak{M}(\tau) = c_0 + c_1\tau$ , which is used to determine the reduced pseudo-ITD matrix elements for the subsequent analyses. The values of the fitted parameters are tabulated in Table 6.4. Out of 36 different fits, six examples of such extrapolation are presented in Figure 6.18. For all the extrapolations,  $\chi^2/\text{d.o.f.} < 1.0$ . The reduced pseudo-ITD in the zero flow time limit is shown in Figure 6.19.

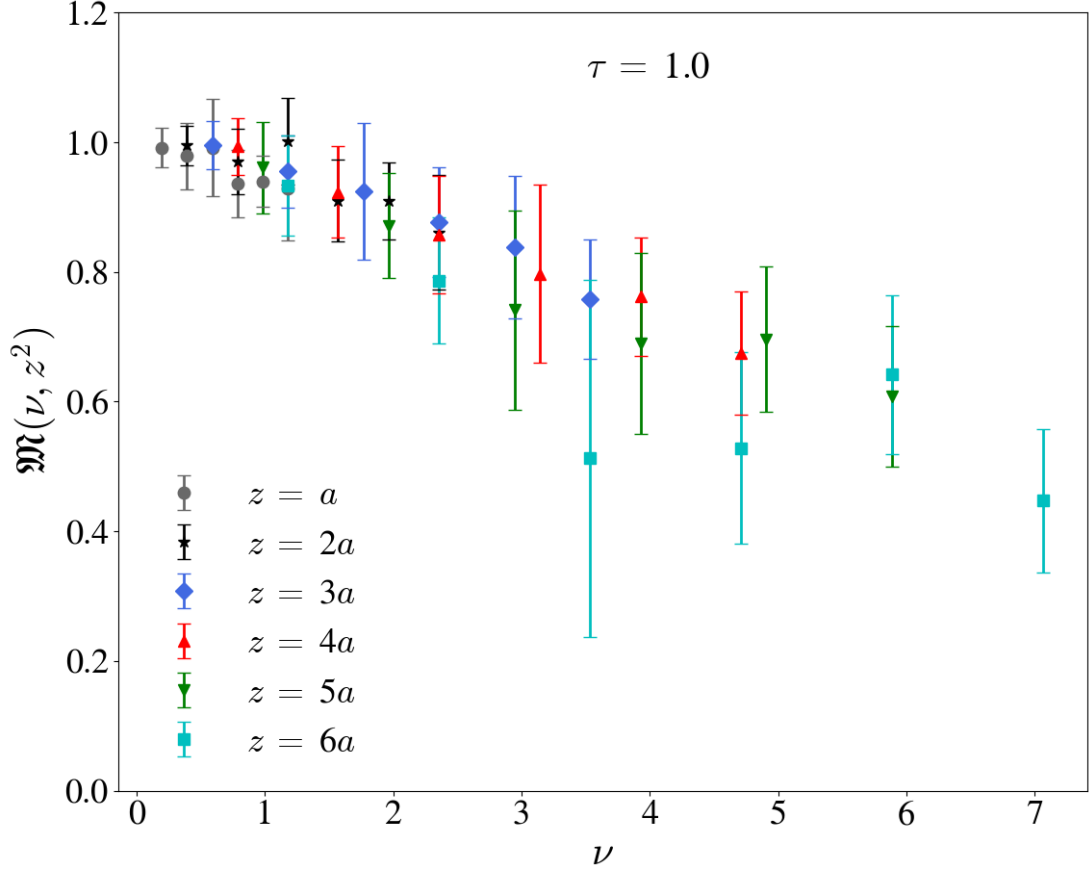


FIG. 6.10: The reduced matrix elements,  $\mathfrak{M}(\nu, z^2)$  with respect to the Ioffe-time for the flow time = 1.0 in lattice units.

$p$ (GeV)	$z(a)$	$A$	$B$	$\chi^2/\text{d.o.f.}$
0.41	1	1.00(3)	-0.00(1)	0.33
0.41	2	0.98(3)	-0.00(1)	0.50
0.41	3	0.97(3)	0.00(1)	0.26
0.41	4	0.97(3)	-0.00(1)	0.27
0.41	5	0.92(5)	0.01(2)	0.32
0.41	6	0.92(5)	0.00(1)	0.40
0.82	1	0.98(4)	-0.00(1)	0.12

0.82	2	0.97(4)	0.00(1)	0.43
0.82	3	0.93(5)	0.00(2)	0.10
0.82	4	0.88(6)	0.02(2)	0.30
0.82	5	0.86(6)	0.00(2)	0.18
0.82	6	0.78(7)	0.01(2)	0.65
1.23	1	0.99(5)	-0.00(2)	0.11
1.23	2	0.99(6)	-0.01(2)	0.11
1.23	3	0.87(7)	0.01(2)	0.15
1.23	4	0.82(7)	0.02(3)	0.13
1.23	5	0.68(10)	0.04(3)	0.09
1.23	6	0.62(12)	0.03(3)	0.55
1.64	1	0.95(3)	-0.00(1)	0.56
1.64	2	0.89(4)	0.01(1)	0.33
1.64	3	0.85(4)	0.01(1)	0.20
1.64	4	0.70(7)	0.04(2)	0.13
1.64	5	0.58(9)	0.05(2)	0.31
1.64	6	0.45(10)	0.08(3)	0.47
2.05	1	0.94(4)	0.00(1)	1.28
2.05	2	0.90(5)	0.01(2)	0.10
2.05	3	0.81(8)	0.02(3)	0.08
2.05	4	0.71(8)	0.01(2)	0.25
2.05	5	0.59(7)	0.03(2)	0.11
2.05	6	0.53(7)	0.04(2)	0.27
2.46	1	0.90(6)	0.00(1)	0.87
2.46	2	0.84(8)	0.02(2)	0.32

2.46	3	0.72(7)	0.03(2)	0.59
2.46	4	0.63(9)	0.03(3)	0.05
2.46	5	0.50(9)	0.04(3)	0.34
2.46	6	0.42(9)	0.03(2)	0.38

TABLE 6.4: The reduced matrix elements extrapolated to the zero flow time for each nucleon momentum and each field separation. The flowed reduced matrix elements are fitted using a linear form:  $\mathfrak{M}(\tau) = c_0 + c_1\tau$ , where  $c_0$  is the reduced matrix elements at  $\tau \rightarrow 0$ , and  $\chi^2/\text{d.o.f.}$  is the goodness-of-fits.

## 6.5 Gluon PDF Extraction

### 6.5.1 Jacobi Polynomial Parametrization

Determining the PDFs from the lattice calculations involves the challenge of how to extract a continuous distribution from the discrete lattice data in the best way, compounded by a limited number of data points due to a finite range of field separations and hadron momenta, and therefore a finite range of  $\nu$ . By performing a phenomenological analysis of the NNPDF unpolarized gluon PDF [29], it has been found in [145] that a much larger  $\nu$ -range than that of the present calculation, or any available lattice QCD determination of the gluon ITD [94, 95], is necessary to determine the gluon distribution in the entire  $x$ -region from the ITD data. Therefore, a proper determination of the gluon distribution is not expected from this calculation in the entire  $x$ -region, especially in the small- $x$  domain.

Moreover, the extraction of the unpolarized gluon PDF from the lattice results in-

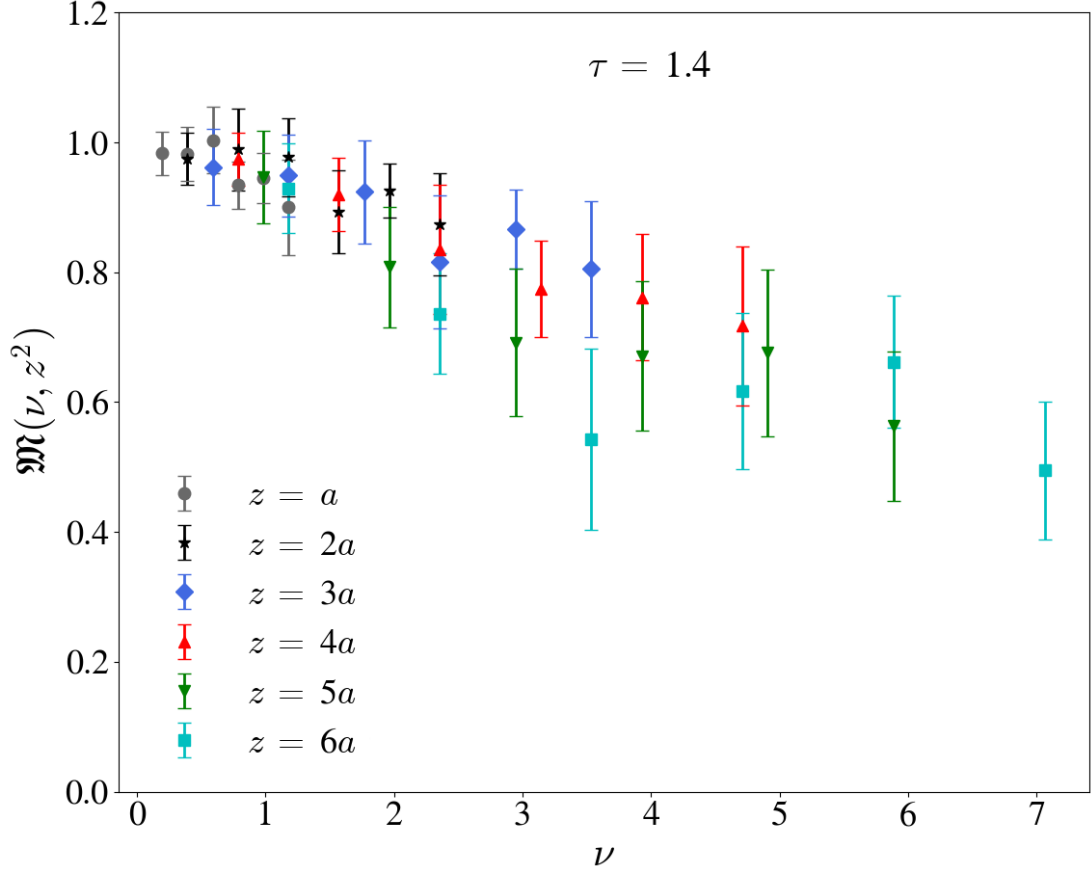


FIG. 6.11: The reduced matrix elements,  $\mathfrak{M}(\nu, z^2)$  with respect to the Ioffe-time for the flow time = 1.4 in lattice units.

volves inverting the convolution that relates the PDF to the lattice matrix elements. As only a limited number of discrete and noisy matrix elements can be accessed on the lattice, this inversion problem is ill-posed. A number of techniques have been proposed to overcome this inverse problem [146], such as discrete Fourier transform, the Backus-Gilbert method [146, 76], the Bayes-Gauss-Fourier transform [84], adapting phenomenologically-motivated functional forms [77], and finally the application of neural networks [147, 148], which provide more flexible parameterizations of the PDFs. Here, the gluon PDF is extracted from the reduced pseudo-ITD using the Jacobi polynomial parametrization proposed in [79] and used in [44, 102]. In this method, the reduced pseudo-ITD is directly

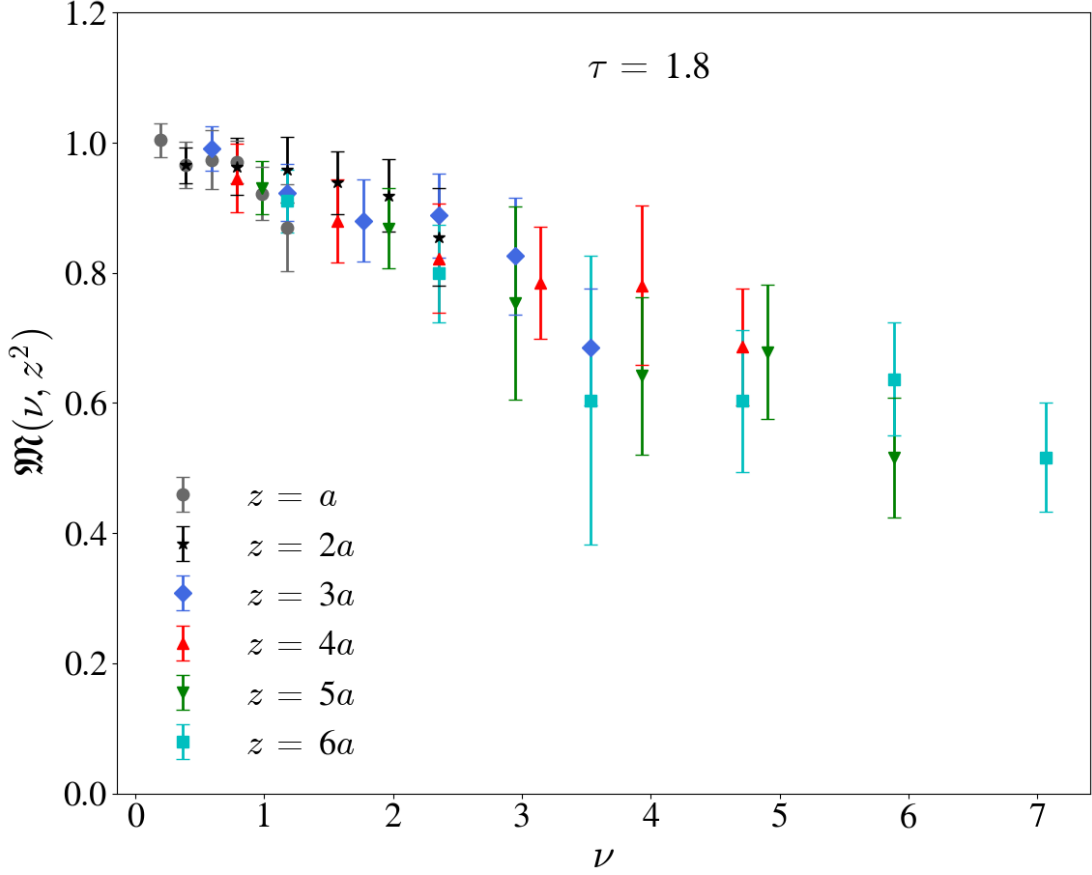


FIG. 6.12: The reduced matrix elements,  $\mathfrak{M}(\nu, z^2)$  with respect to the Ioffe-time for the flow time = 1.8 in lattice units.

parametrized into the gluon PDF, avoiding the intermediate step of calculating the Ioffe-time distribution, thus reducing one source of fitting bias.

The fitting procedure is carried out with different fit-expressions of the gluon PDF, in addition to the lattice spacing correction terms, with the goal of capturing the lattice artifacts. The first model used for the Jacobi polynomial parametrization of the reduced pseudo-ITD is the simplest form for the PDF containing the matching kernel and the leading PDF behavior, which is labeled as [2-param (Q)].

$$\mathfrak{M}(\nu, z^2) = \int_0^1 dx \mathcal{K}(x\nu, \mu^2 z^2) \frac{x^\alpha (1-x)^\beta}{B(\alpha+1, \beta+1)}. \quad (6.61)$$

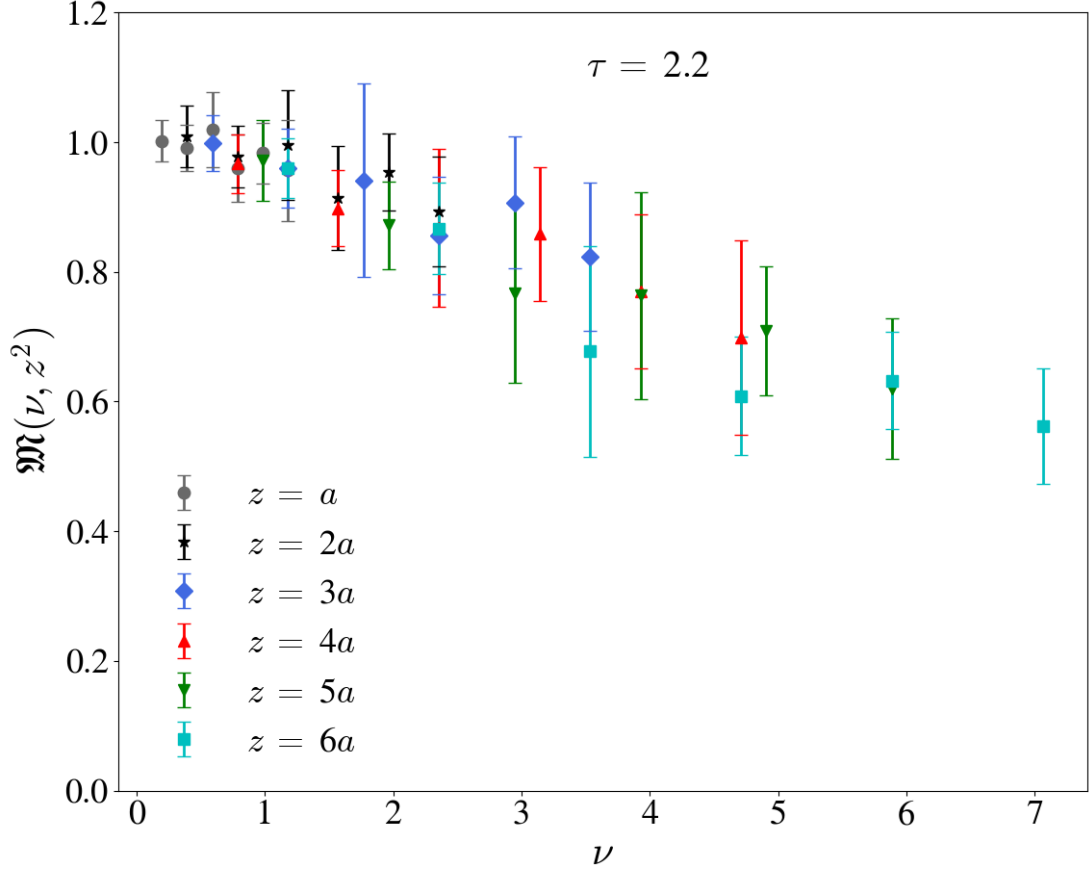


FIG. 6.13: The reduced matrix elements,  $\mathfrak{M}(\nu, z^2)$  with respect to the Ioffe-time for the flow time = 2.2 in lattice units.

Here,  $\mathcal{K}(x\nu, \mu^2 z^2)$  is the matching kernel that factorizes the reduced pseudo-ITD directly to the gluon PDF; and the beta function is  $B(a, b) = \int_0^1 r^{a-1} (1-r)^{b-1} dr$ . To assess the fit model, and the associated systematic uncertainties, other terms are added to the model. The effect of adding one transformed Jacobi polynomial to the functional form of the PDF is considered, labelling this model [3-param (Q)],

$$\mathfrak{M}(\nu, z^2) = \int_0^1 dx \mathcal{K}(x\nu, \mu^2 z^2) x^\alpha (1-x)^\beta \left( \frac{1}{B(\alpha+1, \beta+1)} + d_1^{(\alpha, \beta)} J_1^{(\alpha, \beta)}(x) \right). \quad (6.62)$$

Another model is also considered, denoted by [2-param (Q) + P<sub>1</sub>] for which a nuisance

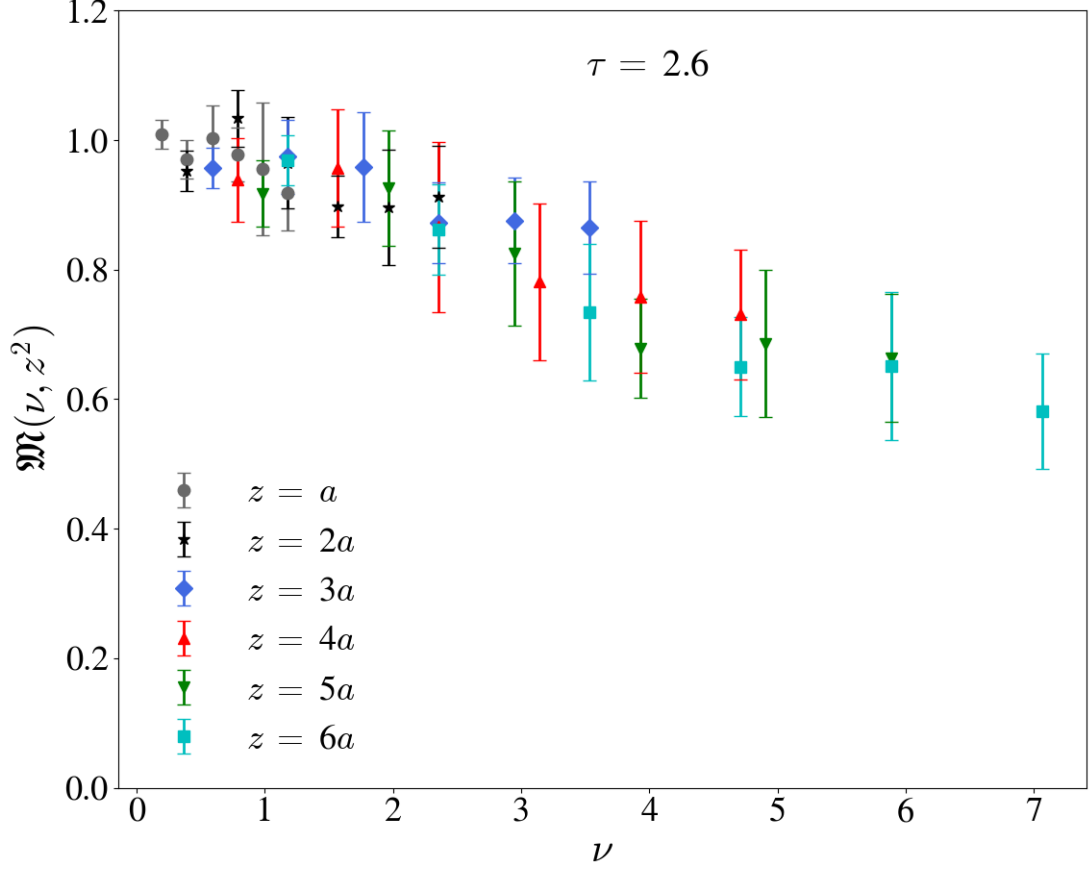


FIG. 6.14: The reduced matrix elements,  $\mathfrak{M}(\nu, z^2)$  with respect to the Ioffe-time for the flow time = 2.6 in lattice units.

term is added to capture possible  $\mathcal{O}\left(\frac{a}{|z|}\right)$  effects. This nuisance term can be parametrized by a transformed Jacobi polynomial [79]

$$\mathfrak{M}(\nu, z^2) = \int_0^1 dx \mathcal{K}(x\nu, \mu^2 z^2) \frac{x^\alpha (1-x)^\beta}{B(\alpha+1, \beta+1)} + \left(\frac{a}{|z|}\right) P_1(\nu), \quad (6.63)$$

where

$$P_1(\nu) = p_1^{(\alpha, \beta)} \int_0^1 dx \cos(\nu x) x^\alpha (1-x)^\beta J_1^{(\alpha, \beta)}(x). \quad (6.64)$$

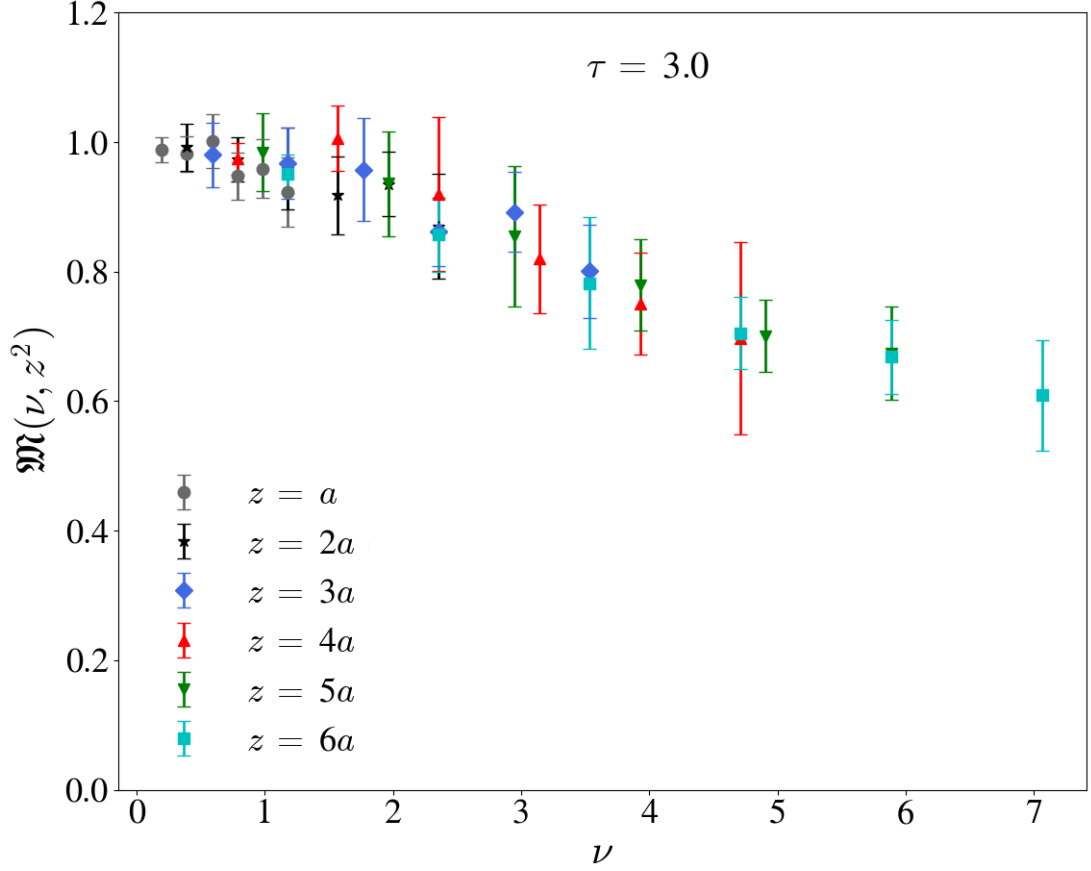


FIG. 6.15: The reduced matrix elements,  $\mathfrak{M}(\nu, z^2)$  with respect to the Ioffe-time for the flow time = 3.0 in lattice units.

The transformed Jacobi polynomials,  $J_n^{(\alpha, \beta)}(x)$  are defined as

$$J_n^{(\alpha, \beta)}(x) = \sum_{j=0}^n \omega_{n,j}^{(\alpha, \beta)} x^j, \quad (6.65)$$

with

$$\omega_{n,j}^{(\alpha, \beta)} = \binom{n}{j} \frac{(-1)^j \Gamma(\alpha + n + 1) \Gamma(\alpha + \beta + n + j + 1)}{n! \Gamma(\alpha + \beta + n + 1) \Gamma(\alpha + j + 1)}. \quad (6.66)$$

Here,  $\Gamma(n)$  is the Gamma function. The orthogonality relation for these transformed Jacobi

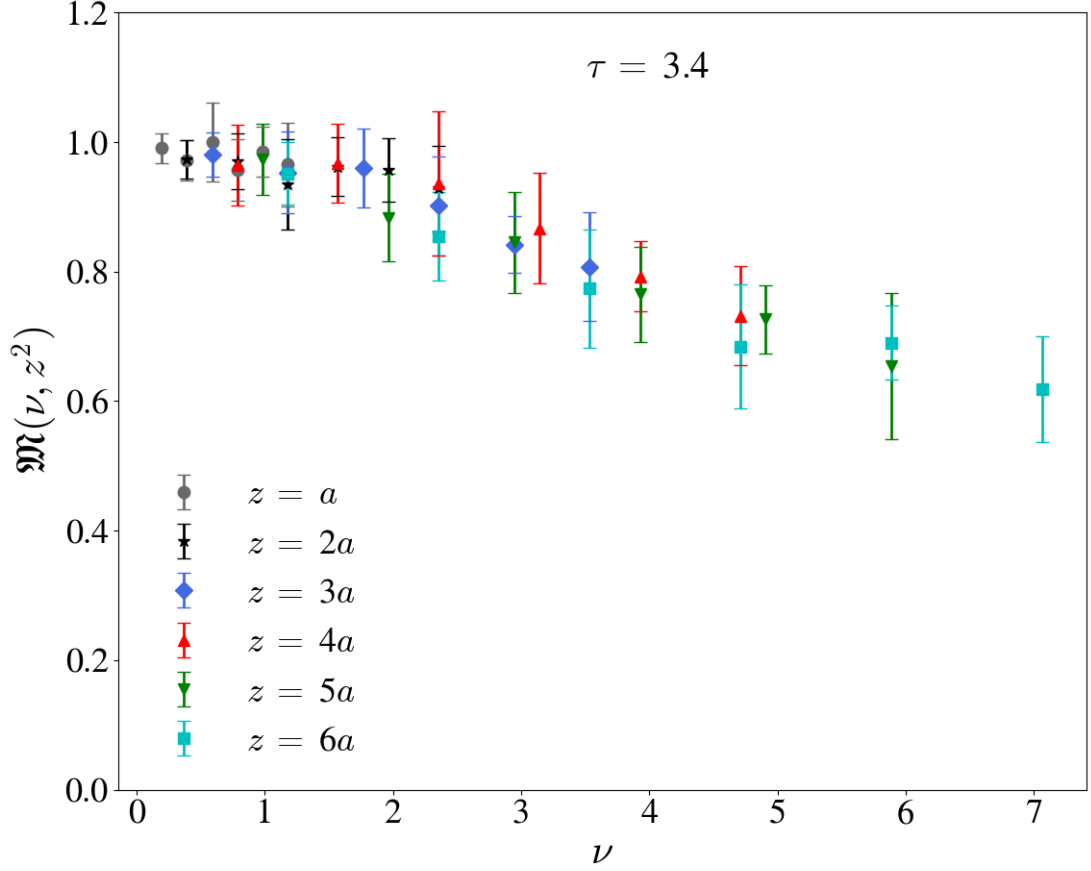


FIG. 6.16: The reduced matrix elements,  $\mathfrak{M}(\nu, z^2)$  with respect to the Ioffe-time for the flow time = 3.4 in lattice units.

polynomials becomes

$$\int_0^1 dx x^\alpha (1-x)^\beta J_n^{(\alpha, \beta)}(x) J_m^{(\alpha, \beta)}(x) = N_n^{(\alpha, \beta)} \delta_{n,m}, \quad (6.67)$$

where

$$N_n^{(\alpha, \beta)} = \frac{1}{2n + \alpha + \beta + 1} \frac{\Gamma(\alpha + n + 1) \Gamma(\beta + n + 1)}{n! \Gamma(\alpha + \beta + n + 1)}. \quad (6.68)$$

The transformed Jacobi polynomials form a complete basis of functions in the interval  $[0,1]$ , making it possible to parametrize the PDF.

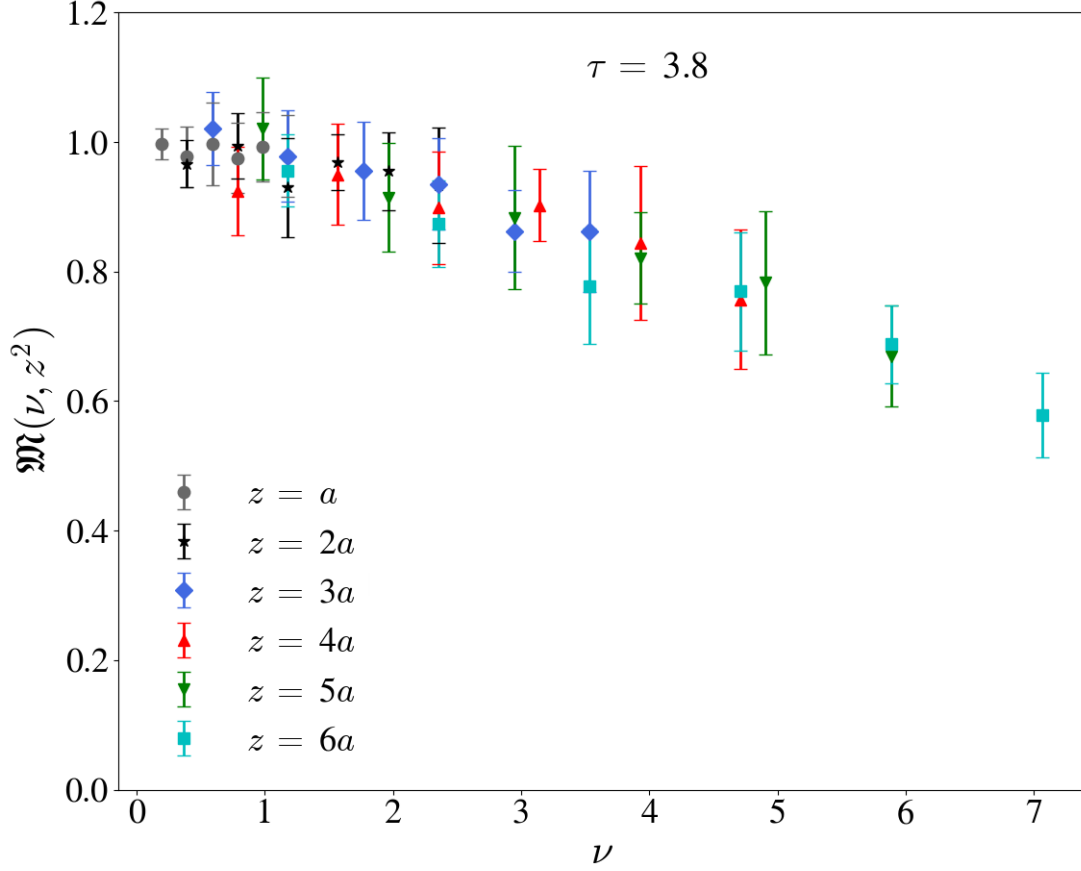


FIG. 6.17: The reduced matrix elements,  $\mathfrak{M}(\nu, z^2)$  with respect to the Ioffe-time for the flow time = 3.8 in lattice units.

Bayesian analysis is used to extract the PDF from the reduced pseudo-ITD. Let the set of fit parameters, which includes the exponents  $\alpha$ ,  $\beta$ , and the linear coefficients of the Jacobi series for the PDF and the additional terms, be denoted by  $\theta$ . Bayes' theorem gives the posterior distribution,  $P[\theta|\mathfrak{M}, I]$ , which describes the probability distribution of a given set of parameters being the true parameters for a given set of data,  $\mathfrak{M}(\nu, z^2)$ , and the prior information,  $I$ , as

$$P[\theta|\mathfrak{M}, I] = \frac{P[\mathfrak{M}|\theta]P[\theta|I]}{P[\mathfrak{M}|I]}. \quad (6.69)$$

Here,  $P[\mathfrak{M}|\theta]$  is the probability distribution of the data for a given set of model parameters.

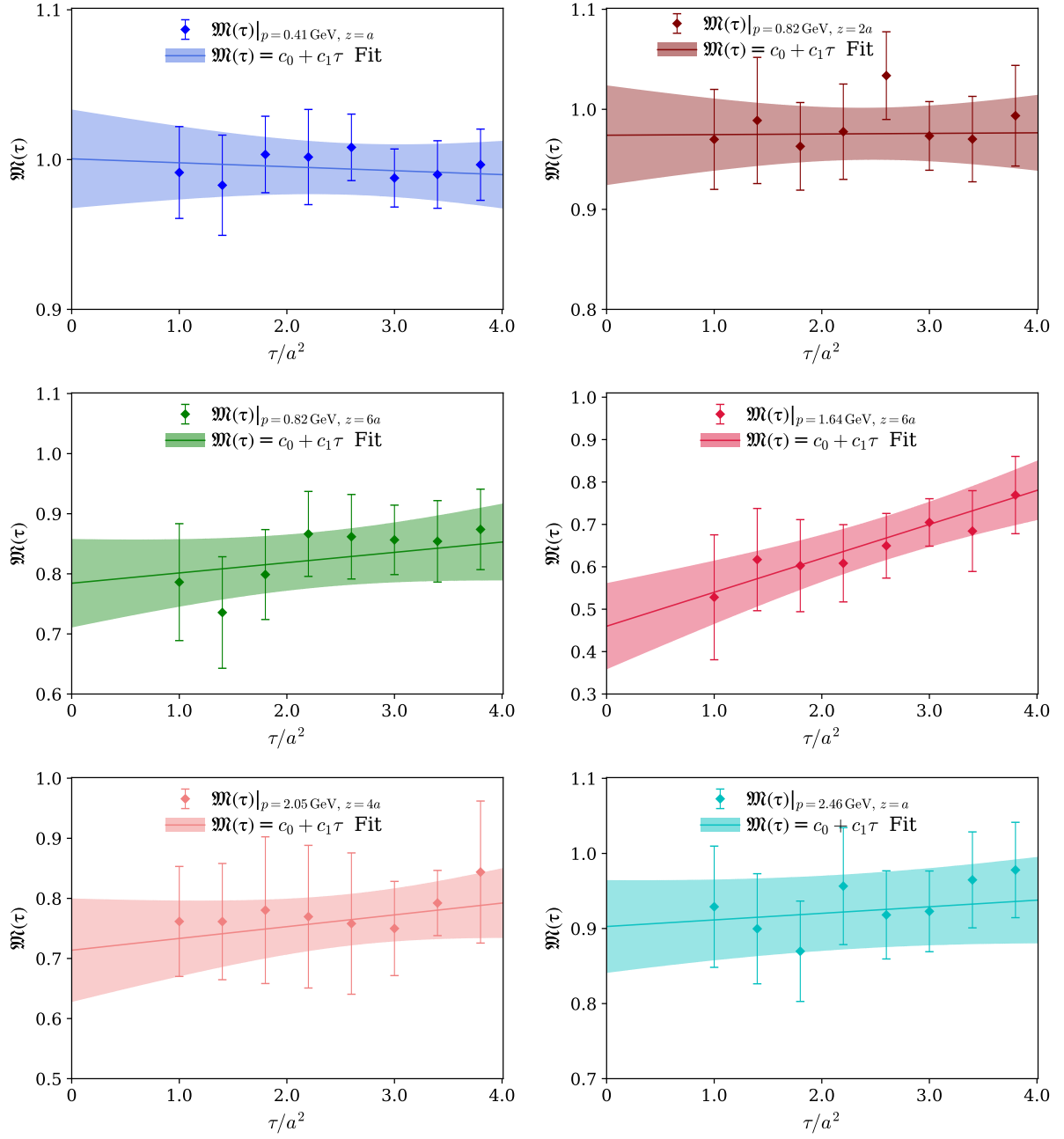


FIG. 6.18: The reduced matrix elements,  $\mathfrak{M}(\tau)$  extrapolated to the  $\tau \rightarrow 0$  limit for different nucleon momenta and different field separations. The functional form used to fit the reduced matrix elements is:  $\mathfrak{M}(\tau) = c_0 + c_1\tau$ . The top-left panel shows the fit for  $p = 1 \times \frac{2\pi}{aL} = 0.41$  GeV and  $z = a = 0.094$  fm. The top-right panel shows the fit for  $p = 2 \times \frac{2\pi}{aL} = 0.82$  GeV and  $z = 2a = 0.188$  fm. The middle-left panel shows the fit for  $p = 2 \times \frac{2\pi}{aL} = 0.82$  GeV and  $z = 6a = 0.564$  fm. The middle-right panel shows the fit for  $p = 4 \times \frac{2\pi}{aL} = 1.64$  GeV and  $z = 6a = 0.564$  fm. The bottom-left panel shows the fit for  $p = 5 \times \frac{2\pi}{aL} = 2.05$  GeV and  $z = 4a = 0.376$  fm. The bottom-right panel shows the fit for  $p = 6 \times \frac{2\pi}{aL} = 2.46$  GeV and  $z = a = 0.094$  fm.

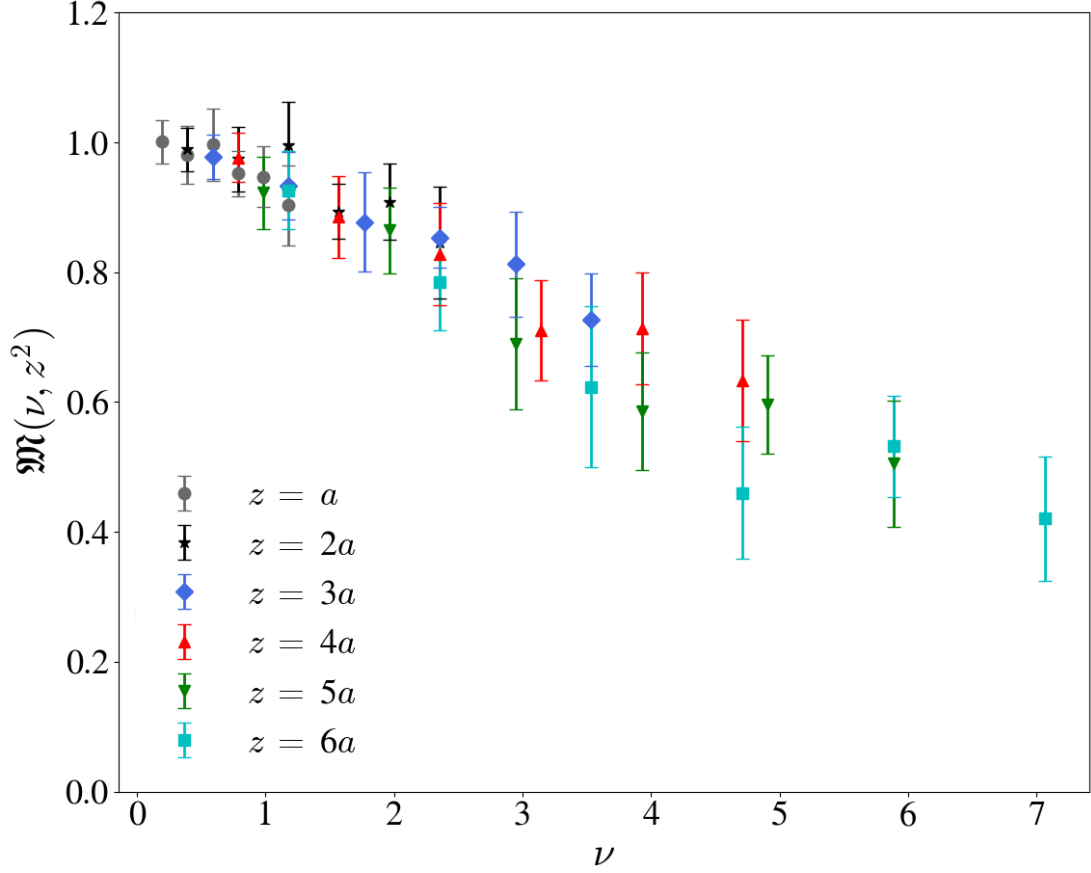


FIG. 6.19: The reduced Ioffe-time pseudo-distribution,  $\mathfrak{M}(\nu, z^2)$  plotted with respect to the Ioffe-time  $\nu$ . For each nucleon momentum and field separation, the reduced matrix elements for different flow times are extrapolated to the limit,  $\tau \rightarrow 0$ , extracting the flow time independent reduced pseudo-ITD.

The prior distribution, which describes the probability distribution of a set of parameters given some previously held information, is  $P[\theta|I]$ , and  $P[\mathfrak{M}|I]$  is the marginal likelihood or evidence that describes the probability that the data are correct given the previously held information.

In this parametrization, the PDF is dominated by the leading behavior  $x^\alpha(1-x)^\beta$ , and the other terms should be small corrections to this. Therefore, in the [3-param (Q)] model, the prior for the PDF model parameter,  $d_1^{(\alpha,\beta)}$  is given by a Gaussian distribution, with a mean and width of  $d_0$  and  $\sigma_d$ , respectively. Similarly, in the [2-param (Q) + P<sub>1</sub>]

model, the parameter for the additional  $P_1$  term,  $p_1^{(\alpha,\beta)}$  is expected to be a small correction to the dominant PDF and a Gaussian distribution is used as a prior. The mean and width of the distribution are given by  $e_0$  and  $\sigma_e$ .

Guided by phenomenological fits of the PDFs,  $\alpha$  and  $\beta$  are set to be positive and their prior distributions are set to be log-normal distributions,

$$P(x, \mu_l, \sigma, x_0) = \frac{1}{(x - x_0)\sigma\sqrt{2\pi}} e^{-[\log(x-x_0)-\mu_l]^2/2\sigma^2}, \quad (6.70)$$

where  $\mu_l$  is the mean and  $\sigma^2$  the variance of the distribution of  $\log(x - x_0)$ , and  $x_0$  is the lower bound of the log-normal distributions. The most likely parameters of the model are found by maximizing the posterior distribution. This is performed by minimizing the negative log of the posterior distribution,

$$L^2 = -2\log(P[\theta|\mathfrak{M}, I]) + C, \quad (6.71)$$

where  $C$  is the normalization of the posterior, which is independent of the model parameters.

In Figure 6.20, the light-cone ITDs obtained from these three models are compared. Here, it can be observed that the ITDs do not differ among the three models, indicating that adding more terms to the functional form of the PDF or adding more nuisance terms does not improve the quality of the fits. The limited Ioffe-time range does not permit the addition of an arbitrary number of parameters to the fit models. Figure 6.21 compares the resulting PDFs from these three models and finds no quantitative difference among them. The  $L^2/\text{d.o.f.}$  and  $\chi^2/\text{d.o.f.}$  of the models are listed in Table 6.5. No significant changes are found among the three models. The  $\chi^2/\text{d.o.f.}$  and  $L^2/\text{d.o.f.}$  values are also in the acceptable range and their proximity shows that the prior distributions on the PDF parameters do not have a significant effect on the fit. Therefore, for the following

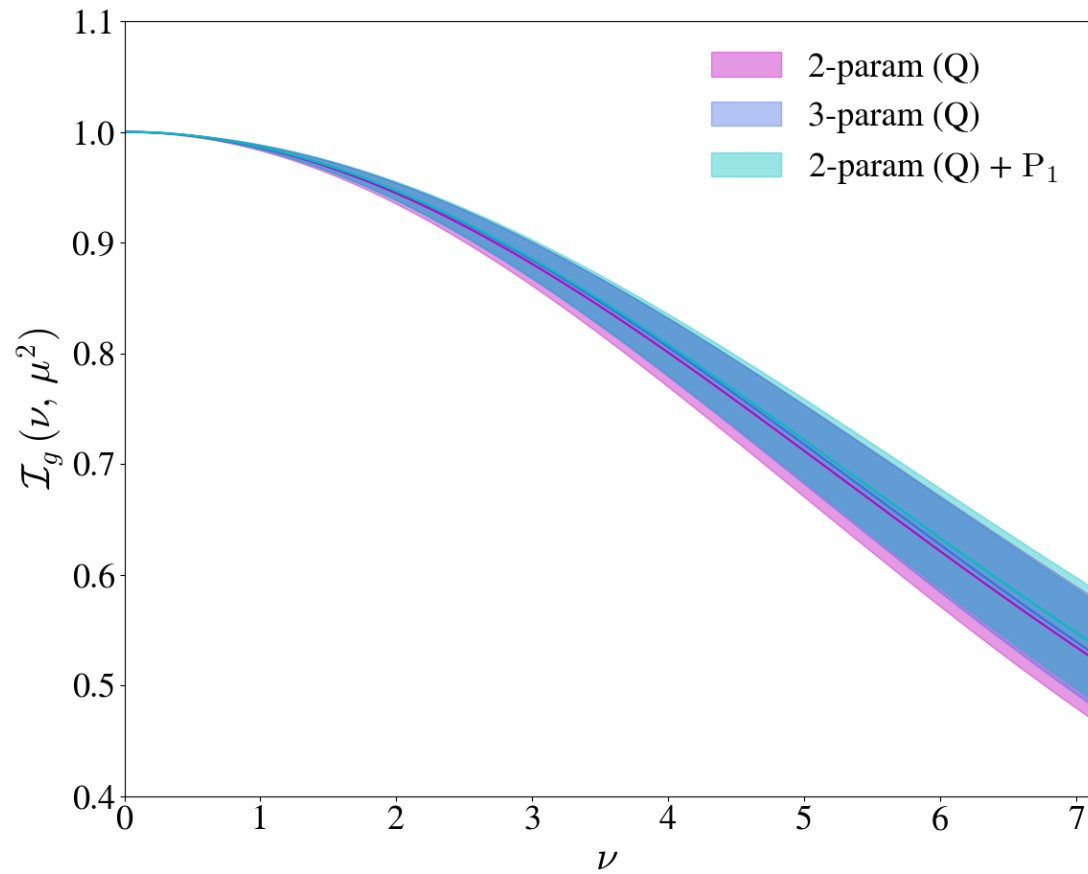


FIG. 6.20: Comparison among the light-cone Ioffe-time distributions calculated from the three models at 2 GeV in the  $\overline{\text{MS}}$ -scheme calculated using the Jacobi polynomial parametrization.

discussion, the focus is on the [2-param (Q)] model.

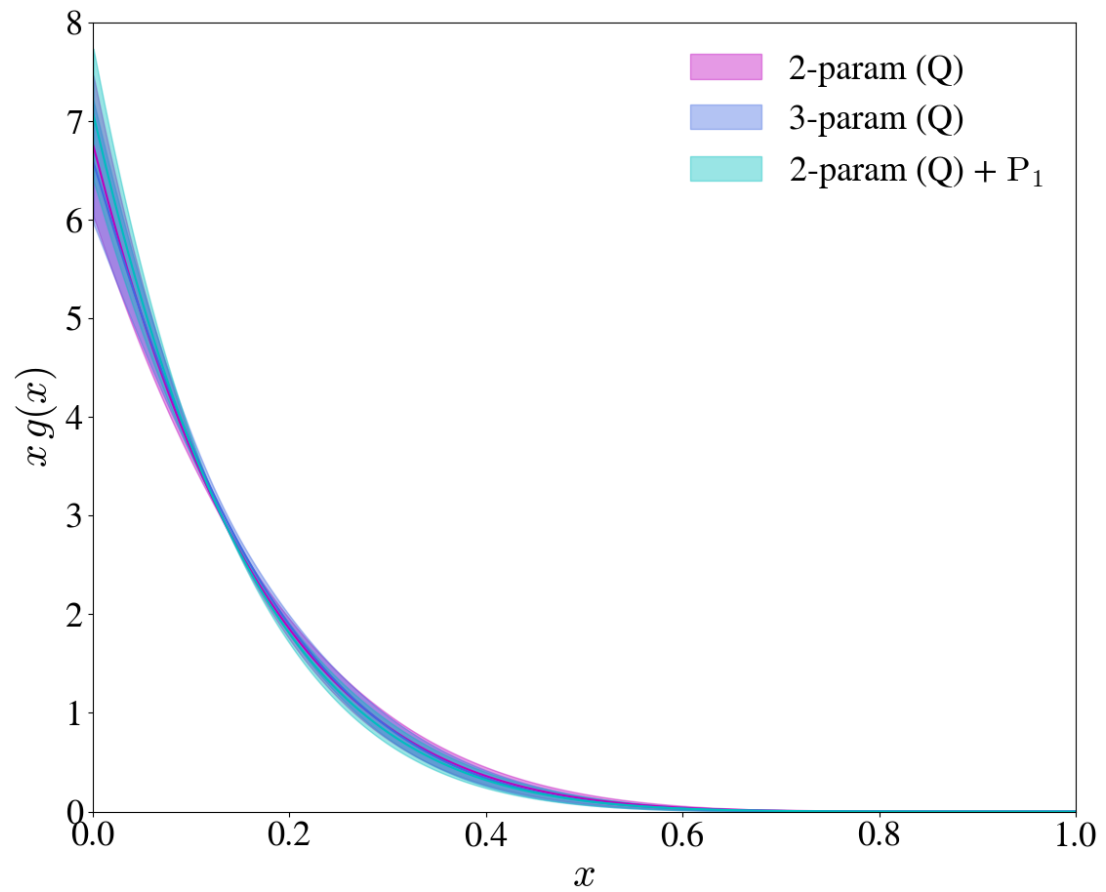


FIG. 6.21: Comparison among the  $xg(x)$  distributions calculated from the three models at 2 GeV in the  $\overline{\text{MS}}$ -scheme calculated using the Jacobi polynomial parametrization.

Model	$L^2/\text{d.o.f.}$	$\chi^2/\text{d.o.f.}$
2-param (Q)	1.07	0.81
3-param (Q)	1.11	0.82
2-param (Q) + P <sub>1</sub>	1.04	0.77

TABLE 6.5: The  $L^2/\text{d.o.f.}$  and the  $\chi^2/\text{d.o.f.}$  of different models used to perform the Jacobi polynomial parametrization of the lattice reduced pseudo-ITD to calculate the gluon PDF.

In Figure 6.22, the reduced pseudo-ITD calculated is shown for different separations,  $z$ , along with its fitted bands obtained from the [2-param (Q)] model. In Figure 6.23, the light-cone Ioffe-time distribution is plotted with the lattice data modified by the matching kernel from the short distance factorization. SDF removes the logarithmic  $z^2$  dependence of the reduced pseudo-ITD and introduces the  $\mu^2$  dependence on the light-cone Ioffe-time distribution. This effect can be observed in Figure 6.23, where after applying the matching kernel, the lattice data points with different field separations shift upward, depending on their field separations, and the data points fall on a regular light-cone Ioffe-time distribution for all  $z^2$ . In previous pseudo-PDF calculations such as the pion valence quark distribution determination [74], the PDF moments extracted by implementing SDF show the logarithmic  $z^2$  dependence removed for  $z$  up to 1 fm. Similar results can be found in [72], where the moments of the quark distribution in the nucleon calculated through SDF are found to be independent of a logarithmic  $z^2$  effect for  $z$  as large as 0.93 fm. On the other hand, if SDF breaks down, there should be a non-polynomial  $z^2$  dependence in the lattice data, especially for large  $z^2$ . No such behavior like that is observed within

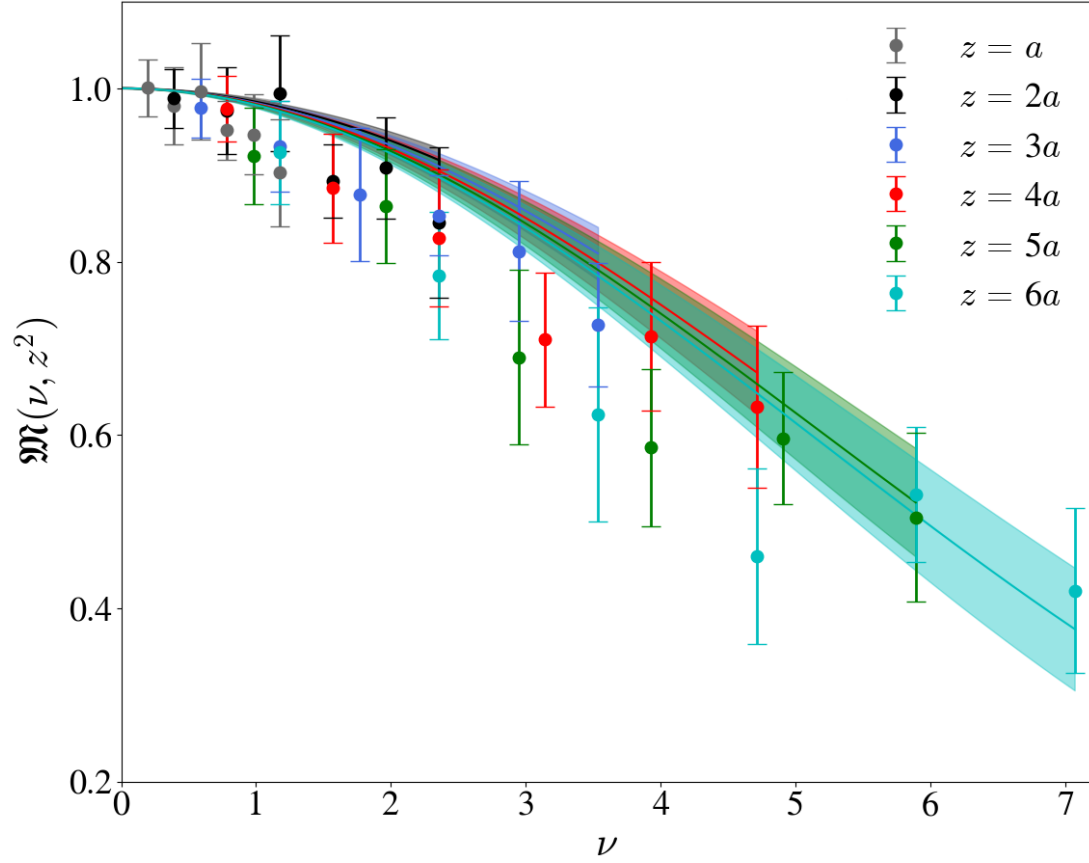


FIG. 6.22: The lattice reduced pseudo-ITD shown along with their reconstructed fitted bands calculated for the model: 2-param (Q).

the current statistics. Instead, the lattice data, after modification by the matching kernel, aligns with the light-cone Ioffe-time distribution band, including the large  $z^2$  data points, indicating that SDF is quite successful in extracting the Ioffe-time distribution.

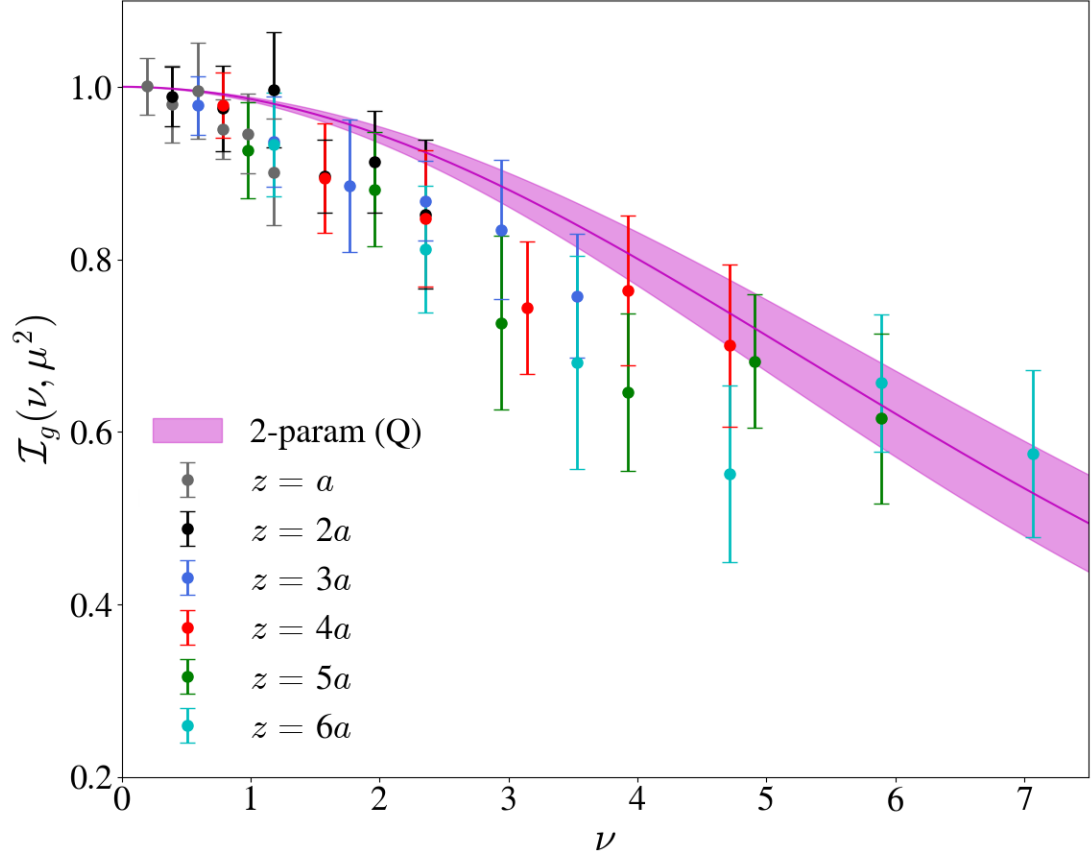


FIG. 6.23: The Ioffe-time distribution after the implementation of the perturbative matching kernel on the lattice reduced pseudo-ITD data along with the light-cone ITD calculated for the model: 2-param (Q), in the  $\overline{\text{MS}}$  renormalization scheme at 2 GeV.

### 6.5.2 Comparison with Phenomenological PDFs

In Figure 6.24, the unpolarized gluon PDF (magenta band) extracted from the [2-param (Q)] model which is described by Eq. (6.61), is presented and compared with the gluon PDFs extracted from the phenomenological data sets CT18 [28], NNPDF3.1 [29], and JAM20 [26] at  $\mu = 2$  GeV. In Figure 6.25, the same comparison is done with the PDFs being plotted in the log-scale along the y axis. This allows one to observe the comparison among the PDFs in the large- $x$  region. A similar comparison can be made with the other global fits of the gluon PDF, such as with CJ15 [30], HERAPDF2.0 [149], MSHT20 [27].

To determine the normalization of the gluon PDF according to Eq. (6.16), the ex-

tracted PDF needs to be normalized with the gluon momentum fraction. There has been a number of lattice calculations to extract the gluon momentum fraction [89, 150], as well as phenomenological calculations [29, 28]. The gluon momentum fraction used in this calculation, is taken from [89], which is  $\langle x \rangle_g = 0.427(92)$  in the  $\overline{\text{MS}}$  scheme at the renormalization scale  $\mu = 2$  GeV, and applied to the gluon PDF. One could similarly adopt the normalization from the  $\langle x \rangle_g$  determination in [150]. The uncertainties of the extracted gluon PDF and the gluon momentum fraction from [89] are considered to be uncorrelated. The statistical uncertainty of the gluon PDF determined from the fit Eq. (6.61) and the uncertainty of the gluon momentum fraction are added in quadrature and the final uncertainty is shown as the lighter magenta band in Figure 6.24 and 6.25.

As discussed in [145], from the fitting of the ITD constructed from the NNPDF  $xg(x)$  distribution, one needs the lattice data beyond  $\nu \sim 15$  to evaluate the gluon distribution in the small- $x$  region. In the present calculation, the ITD is extracted up to  $\nu \sim 7.07$ . Therefore, the larger uncertainty and difference in the small- $x$  region determined from the lattice data is expected. As a cautionary remark, it should be kept in mind that the mixing of the gluon operator with the quark singlet sector is not included in the present calculation. From Eq. (6.12), it is evident that the gluonic distribution mixes with the singlet quark distribution under scale evolution. Since the matrix element associated with the singlet quark distribution has not been calculated, this mixing is neglected here.

Moreover, this calculation is performed at an unphysical pion mass. In principle, the physical pion mass, the continuum, and the infinite volume extrapolations should be performed for a proper comparison with the phenomenological distribution. Therefore, it remains a matter of future investigation to draw a more specific conclusion about the  $xg(x)$  distribution extracted from this lattice QCD calculation. It should also be noted that the shrinking of the statistical uncertainty band in the PDF near  $x \sim 0.15$  results from the correlation of the PDF fit parameters. This feature has also been seen in previous

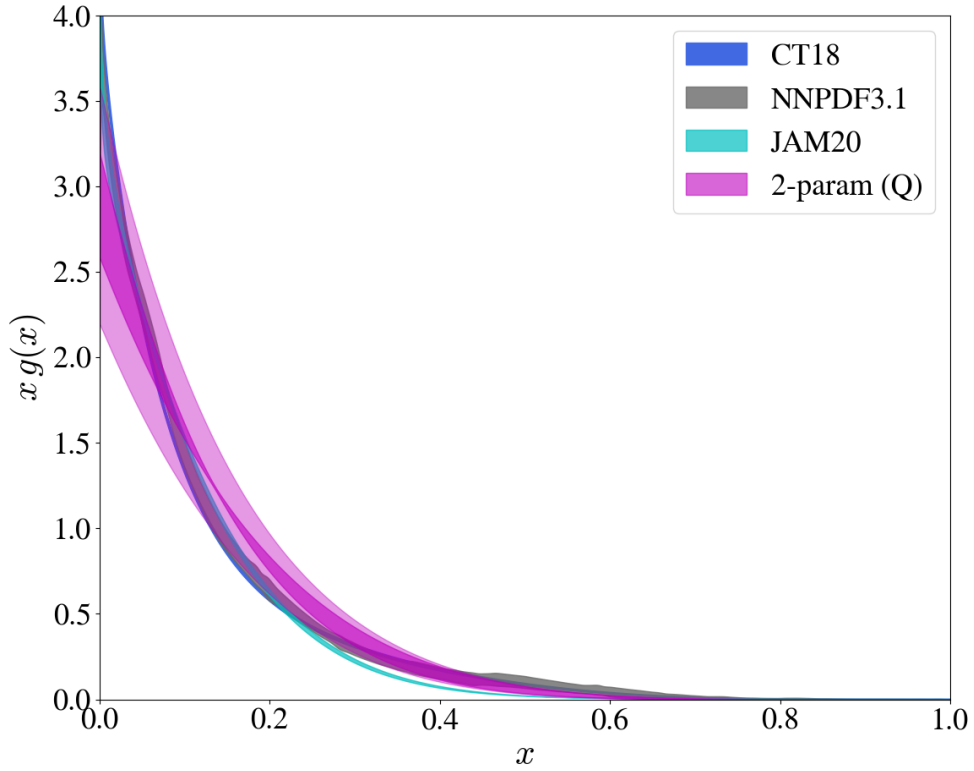


FIG. 6.24: The unpolarized gluon PDF (magenta band) extracted from the lattice data using the 2-param (Q) model. The result is compared with the gluon PDFs extracted from the global fits to the experimental data, CT18 [28], NNPDF3.1 [29], and JAM20 [26]. The normalization of the gluon PDF is performed using the gluon momentum fraction  $\langle x \rangle_g^{\overline{\text{MS}}}(\mu = 2 \text{ GeV}) = 0.427(92)$  from [89]. The statistical uncertainty of the gluon PDF determined from the lattice calculation and the uncertainty of the gluon momentum fraction are added in quadrature and the final uncertainty is shown as the lighter magenta band.

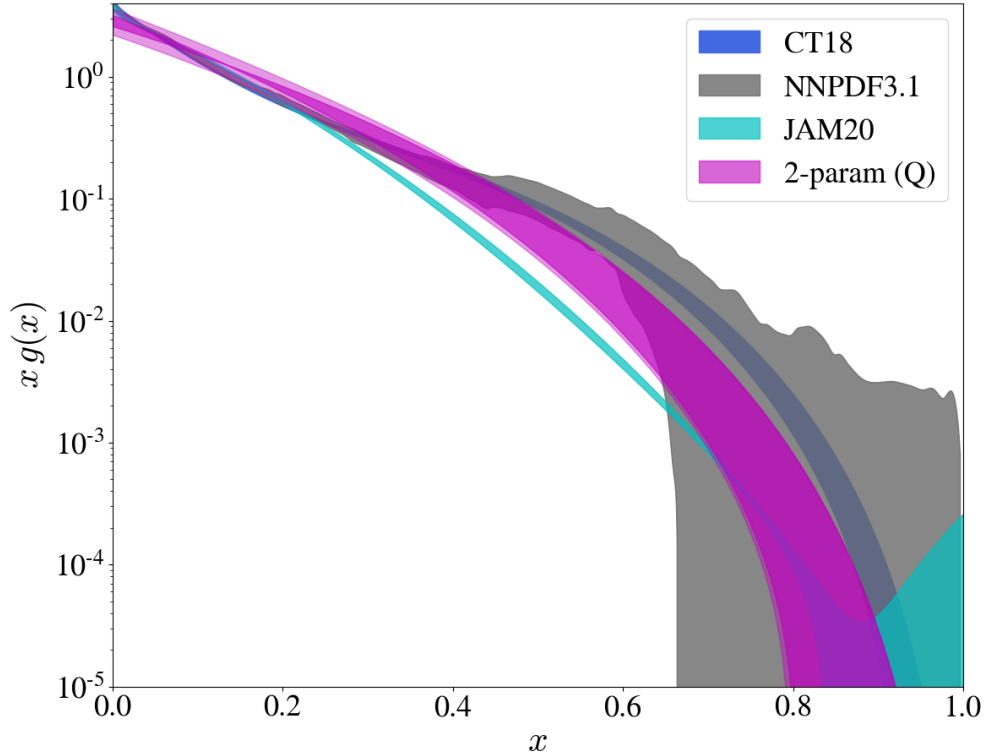


FIG. 6.25: The unpolarized gluon PDF (magenta band) extracted from the lattice data and compared with gluon PDFs from the global fits to the experimental data. The statistical uncertainty of the gluon PDF determined from the lattice calculation and the uncertainty of the gluon momentum fraction are added in quadrature and the final uncertainty is shown as the lighter magenta band. The distributions are shown in log-scale along the y axis to enhance the view of the large- $x$  region.

works [74, 82, 94, 76].

However, within these limitations, the large- $x$  distribution is found to be in reasonable agreement with the global fits of  $xg(x)$  distribution, as can be seen from Figure 6.25. The value of  $\beta = 5.85(72)$  determined in this calculation is statistically in good agreement with the leading  $(1-x)^\beta$  behavior obtained in [145] from the fit to the NNPDF3.1 gluon distribution and a recent phenomenological calculation [151]. The  $\mathcal{I}_S(\nu, \mu^2)$  distribution, which is not included in the present work, is expected to have an increasingly larger

effect as  $\nu$  increases and is expected to have an observable effect in the small- $x$  gluon distribution. However, in the present lattice calculation at heavier up- and down-quark masses, one expects the singlet distribution to increase at a slower rate compared to the phenomenological singlet distribution, therefore having a smaller effect on the Ioffe-time distribution in the  $0 \leq \nu \leq 7.07$ -range.

# CHAPTER 7

## Conclusion and Outlook

The spectral analyses of the positive-parity delta and nucleon using an isotropic clover action support the observations found in earlier works at heavier pion masses and using the anisotropic clover action at a coarser spatial lattice spacing, but finer temporal lattice spacing. In particular, it is found that the rotational symmetry is largely observed at the hadronic scale, enabling one to reliably identify the spins of the states through their predominant overlap of the operators derived from the continuum operators of definite spin. However, the most significant outcome of the spectral analyses is that the spectra exhibit a counting of states in line with that of the quark model, but with additional states that can be identified as “hybrid” in nature, with the gluonic degrees of freedom playing a structural role. The means used to identify such hybrid baryons through the predominant overlap of a class of “hybrid” operators, pioneered in Ref. [1], must inevitably raise the issue of the operator dependence of such an identification. Here using a different action, with a different lattice spacing implemented through the variation of the number of the distillation eigenvectors indicates that the identification of the hybrid-type states in the spectrum is indeed robust.

There are important limitations of the baryon spectral analysis in its use of “single-hadron” operators which do not fully capture the low-lying energy levels in the finite-volume spectrum. The next step in the investigation of the nature of “hybrid” baryons would be to include the multi-hadron operators, and subsequently to compute the infinite-volume momentum-dependent phase shifts. Such a study could also reveal the decay modes of such states, and indeed the first LQCD study of the decay modes of the exotic  $1^{-+}$  hybrid meson has recently been performed [152]. This is more computationally challenging for baryons than for mesons through the increased cost of the Wick contractions, the scaling of the number of the distillation eigenvectors with the increasing volume, and the numerous final states to which they can decay. Nonetheless, the advent of the exascale era of computation makes such computations increasingly realizable. Ultimately, a largely model-independent determination of the quark and gluon content of such resonances will be achieved by the probing of their structure through external currents, and the theoretical framework for such studies is an area of rapid development [153, 154, 155] and application [156, 157].

The second exploration of the role of gluonic degrees of freedom in the nucleon is through the calculation of the gluon PDF. The interpolators that have significant contributions to the ground state of the nucleon are identified from the spectral analysis, and the relevant gluonic matrix elements are calculated by the combined implementation of techniques such as distillation, momentum smearing, gradient flow technique, and the sGEVP method. Distillation allows one not only to improve the sampling of the lattice but also to construct the nucleon two-point correlators with an extended basis of interpolators, which is necessary for the implementation of the sGEVP method. By using momentum smearing, a momentum as high as 2.46 GeV is achieved. The sGEVP method combines the features of the summation method and the GEVP technique, suppressing the excited state contributions to the matrix elements significantly. Gradient flow reduces the UV fluctuations

from the flowed matrix elements. The combination of these techniques enables one to control the signal-to-noise issues to a great extent. The reduced pseudo-ITD is calculated from the flowed reduced matrix elements by fitting the  $\tau$ -dependence using a linear form and extrapolating to the  $\tau \rightarrow 0$  limit. Using the Jacobi polynomial parameterization, the gluon distribution is extracted directly from the reduced pseudo-ITD.

Although systematics like higher-twist contributions, lattice-spacing errors, finite-volume effects, and unphysical pion mass effects cannot be discerned in the present calculation, and the quark-gluon mixing is excluded from the calculation, the resultant ITD has a well-regulated signal-to-noise ratio. The extracted gluon PDF is remarkably consistent with that extracted from various phenomenological distributions. Future endeavors include performing the calculation with a larger number of gauge configurations on the same ensemble, performing the calculation on ensembles at finer lattice spacings and closer-to-physical, light quark masses, and performing a direct calculation of the gluon momentum fraction on the same ensembles. Together, these will enable better control over the systematic uncertainties through the availability of better statistics. Incorporating the quark-gluon mixing into the calculation is another task that is to be undertaken. Further extensions of this work include the calculation of the polarized distributions for which experimental information is particularly sparse. When all the systematic uncertainties are properly quantified and the mixing with the isoscalar quark PDF are included, the lattice calculations will help constrain the gluon PDF at large- $x$ , where the PDF is less constrained by experimental data.

## BIBLIOGRAPHY

- [1] J. J. Dudek and R. G. Edwards, Phys. Rev. D **85**, 054016 (2012), [1201.2349](#).
- [2] M. Gell-Mann (1961).
- [3] J. I. Friedman (1971), URL <https://www.osti.gov/biblio/4715877>.
- [4] P. Zyla et al. (Particle Data Group), PTEP **2020**, 083C01 (2020).
- [5] S. Capstick and N. Isgur, Phys. Rev. D **34**, 2809 (1986), URL <https://link.aps.org/doi/10.1103/PhysRevD.34.2809>.
- [6] N. Isgur and G. Karl, Phys. Rev. D **18**, 4187 (1978), URL <https://link.aps.org/doi/10.1103/PhysRevD.18.4187>.
- [7] K. F. Liu and C. W. Wong, Phys. Rev. D **28**, 170 (1983), URL <https://link.aps.org/doi/10.1103/PhysRevD.28.170>.
- [8] R. G. Edwards, J. J. Dudek, D. G. Richards, and S. J. Wallace, Phys. Rev. D **84**, 074508 (2011), [1104.5152](#).
- [9] T. Barnes and F. Close, Physics Letters B **123**, 89 (1983), ISSN 0370-2693, URL <http://www.sciencedirect.com/science/article/pii/0370269383909656>.
- [10] N. Isgur and J. Paton, Physics Letters B **124**, 247 (1983), ISSN 0370-2693, URL <http://www.sciencedirect.com/science/article/pii/0370269383914454>.

- [11] N. Isgur and J. Paton, Phys. Rev. D **31**, 2910 (1985), URL <https://link.aps.org/doi/10.1103/PhysRevD.31.2910>.
- [12] L. S. Kisslinger and Z. Li, Phys. Rev. D **51**, R5986 (1995), URL <https://link.aps.org/doi/10.1103/PhysRevD.51.R5986>.
- [13] G. K. C. Cheung, C. E. Thomas, J. J. Dudek, and R. G. Edwards (Hadron Spectrum), JHEP **11**, 033 (2017), [1709.01417](https://arxiv.org/abs/1709.01417).
- [14] P. Junnarkar, N. Mathur, and M. Padmanath, Phys. Rev. D **99**, 034507 (2019), [1810.12285](https://arxiv.org/abs/1810.12285).
- [15] M. Chanowitz and S. Sharpe, Nuclear Physics B **222**, 211 (1983), ISSN 0550-3213, URL <http://www.sciencedirect.com/science/article/pii/0550321383906351>.
- [16] J. J. Dudek, R. G. Edwards, M. J. Peardon, D. G. Richards, and C. E. Thomas, Phys. Rev. Lett. **103**, 262001 (2009), [0909.0200](https://arxiv.org/abs/0909.0200).
- [17] J. J. Dudek, R. G. Edwards, M. J. Peardon, D. G. Richards, and C. E. Thomas, Phys. Rev. D **82**, 034508 (2010), [1004.4930](https://arxiv.org/abs/1004.4930).
- [18] J. J. Dudek, R. G. Edwards, B. Joo, M. J. Peardon, D. G. Richards, and C. E. Thomas, Phys. Rev. D **83**, 111502 (2011), [1102.4299](https://arxiv.org/abs/1102.4299).
- [19] J. J. Dudek, R. G. Edwards, P. Guo, and C. E. Thomas (Hadron Spectrum), Phys. Rev. D **88**, 094505 (2013), [1309.2608](https://arxiv.org/abs/1309.2608).
- [20] L. D. Roper, Phys. Rev. Lett. **12**, 340 (1964), URL <https://link.aps.org/doi/10.1103/PhysRevLett.12.340>.
- [21] V. D. Burkert and C. D. Roberts, Rev. Mod. Phys. **91**, 011003 (2019), [1710.02549](https://arxiv.org/abs/1710.02549).

- [22] S. Capstick and P. R. Page, Phys. Rev. D **60**, 111501 (1999), [nucl-th/9904041](#).
- [23] E. Golowich, E. Haqq, and G. Karl, Phys. Rev. D **28**, 160 (1983), [Erratum: Phys.Rev.D 33, 859 (1986)].
- [24] B. Julia-Diaz and D. O. Riska, Nucl. Phys. A **780**, 175 (2006), [nucl-th/0609064](#).
- [25] R. Jaffe and F. Wilczek, Eur. Phys. J. C **33**, S38 (2004), [hep-ph/0401034](#).
- [26] E. Moffat, W. Melnitchouk, T. Rogers, and N. Sato (2021), [2101.04664](#).
- [27] S. Bailey, T. Cridge, L. A. Harland-Lang, A. D. Martin, and R. S. Thorne, Eur. Phys. J. C **81**, 341 (2021), [2012.04684](#).
- [28] T.-J. Hou et al., Phys. Rev. D **103**, 014013 (2021), [1912.10053](#).
- [29] R. D. Ball et al. (NNPDF), Eur. Phys. J. C **77**, 663 (2017), [1706.00428](#).
- [30] A. Accardi, L. T. Brady, W. Melnitchouk, J. F. Owens, and N. Sato, Phys. Rev. D **93**, 114017 (2016), [1602.03154](#).
- [31] S. Dulat, T.-J. Hou, J. Gao, M. Guzzi, J. Huston, P. Nadolsky, J. Pumplin, C. Schmidt, D. Stump, and C. P. Yuan, Phys. Rev. D **93**, 033006 (2016), [1506.07443](#).
- [32] S. Chatrchyan et al. (CMS), Science **338**, 1569 (2012).
- [33] R. Kogler et al., Rev. Mod. Phys. **91**, 045003 (2019), [1803.06991](#).
- [34] I. Albayrak et al., Jefferson Lab PAC 39 Proposal PR12.12.001 (2012).
- [35] A. Accardi et al., Eur. Phys. J. A **52**, 268 (2016), [1212.1701](#).
- [36] A. C. Aguilar et al., Eur. Phys. J. A **55**, 190 (2019), [1907.08218](#).

- [37] R. Abdul Khalek et al. (2021), [2103.05419](#).
- [38] D. P. Anderle et al., *Front. Phys. (Beijing)* **16**, 64701 (2021), [2102.09222](#).
- [39] C.-N. Yang and R. L. Mills, *Phys. Rev.* **96**, 191 (1954).
- [40] H. D. Politzer, *Phys. Rev. Lett.* **30**, 1346 (1973).
- [41] D. J. Gross and F. Wilczek, *Phys. Rev. Lett.* **30**, 1343 (1973).
- [42] K. G. Wilson, *Phys. Rev. D* **10**, 2445 (1974).
- [43] T. Khan, D. Richards, and F. Winter, *Phys. Rev. D* **104**, 034503 (2021), [2010.03052](#).
- [44] T. Khan et al. (HadStruc), *Phys. Rev. D* **104**, 094516 (2021), [2107.08960](#).
- [45] R. P. Feynman, *Phys. Rev. Lett.* **23**, 1415 (1969).
- [46] J. D. Bjorken and E. A. Paschos, *Phys. Rev.* **185**, 1975 (1969).
- [47] V. A. Franke, Y. V. Novozhilov, S. A. Paston, and E. V. Prokhvatilov (1998), [hep-th/9901029](#).
- [48] J. D. Bjorken, *Phys. Rev.* **179**, 1547 (1969).
- [49] K. Symanzik, *Nucl. Phys. B* **226**, 187 (1983).
- [50] K. Symanzik, *Nucl. Phys. B* **226**, 205 (1983).
- [51] M. Lüscher, S. Sint, R. Sommer, and P. Weisz, *Nucl. Phys. B* **478**, 365 (1996), [hep-lat/9605038](#).
- [52] B. Sheikholeslami and R. Wohlert, *Nucl. Phys. B* **259**, 572 (1985).
- [53] C. Gattringer and C. B. Lang, *Quantum chromodynamics on the lattice. An introductory presentation* (2010).

- [54] S. Aoki et al. (Flavour Lattice Averaging Group), *Eur. Phys. J. C* **80**, 113 (2020), [1902.08191](#).
- [55] K.-F. Liu and S.-J. Dong, *Phys. Rev. Lett.* **72**, 1790 (1994), [hep-ph/9306299](#).
- [56] W. Detmold and C. J. D. Lin, *Phys. Rev. D* **73**, 014501 (2006), [hep-lat/0507007](#).
- [57] X. Ji, *Phys. Rev. Lett.* **110**, 262002 (2013), [1305.1539](#).
- [58] X. Ji, *Sci. China Phys. Mech. Astron.* **57**, 1407 (2014), [1404.6680](#).
- [59] A. V. Radyushkin, *Phys. Rev. D* **96**, 034025 (2017), [1705.01488](#).
- [60] Y.-Q. Ma and J.-W. Qiu, *Phys. Rev. D* **98**, 074021 (2018), [1404.6860](#).
- [61] Y.-Q. Ma and J.-W. Qiu, *Phys. Rev. Lett.* **120**, 022003 (2018), [1709.03018](#).
- [62] V. Braun and D. Müller, *Eur. Phys. J. C* **55**, 349 (2008), [0709.1348](#).
- [63] M. Constantinou et al., *Prog. Part. Nucl. Phys.* **121**, 103908 (2021), [2006.08636](#).
- [64] K. Cichy and M. Constantinou, *Adv. High Energy Phys.* **2019**, 3036904 (2019), [1811.07248](#).
- [65] B. L. Ioffe, *Phys. Lett. B* **30**, 123 (1969).
- [66] V. Braun, P. Gornicki, and L. Mankiewicz, *Phys. Rev. D* **51**, 6036 (1995), [hep-ph/9410318](#).
- [67] A. Radyushkin, *PoS QCDEV2017*, 021 (2017), [1711.06031](#).
- [68] A. V. Radyushkin, *Phys. Lett. B* **781**, 433 (2018), [1710.08813](#).
- [69] A. Radyushkin, *Phys. Rev. D* **98**, 014019 (2018), [1801.02427](#).

- [70] I. Balitsky, W. Morris, and A. Radyushkin, Phys. Lett. B **808**, 135621 (2020), [1910.13963](#).
- [71] K. Orginos, A. Radyushkin, J. Karpie, and S. Zafeiropoulos, Phys. Rev. D **96**, 094503 (2017), [1706.05373](#).
- [72] J. Karpie, K. Orginos, and S. Zafeiropoulos, JHEP **11**, 178 (2018), [1807.10933](#).
- [73] B. Joó, J. Karpie, K. Orginos, A. Radyushkin, D. Richards, and S. Zafeiropoulos, JHEP **12**, 081 (2019), [1908.09771](#).
- [74] B. Joó, J. Karpie, K. Orginos, A. V. Radyushkin, D. G. Richards, R. S. Sufian, and S. Zafeiropoulos, Phys. Rev. D **100**, 114512 (2019), [1909.08517](#).
- [75] B. Joó, J. Karpie, K. Orginos, A. V. Radyushkin, D. G. Richards, and S. Zafeiropoulos, Phys. Rev. Lett. **125**, 232003 (2020), [2004.01687](#).
- [76] M. Bhat, K. Cichy, M. Constantinou, and A. Scapellato, Phys. Rev. D **103**, 034510 (2021), [2005.02102](#).
- [77] R. S. Sufian, C. Egerer, J. Karpie, R. G. Edwards, B. Joó, Y.-Q. Ma, K. Orginos, J.-W. Qiu, and D. G. Richards, Phys. Rev. D **102**, 054508 (2020), [2001.04960](#).
- [78] R. S. Sufian, J. Karpie, C. Egerer, K. Orginos, J.-W. Qiu, and D. G. Richards, Phys. Rev. D **99**, 074507 (2019), [1901.03921](#).
- [79] J. Karpie, K. Orginos, A. Radyushkin, and S. Zafeiropoulos (2021), [2105.13313](#).
- [80] K. Zhang, Y.-Y. Li, Y.-K. Huo, P. Sun, and Y.-B. Yang (2020), [2012.05448](#).
- [81] T. Izubuchi, L. Jin, C. Kallidonis, N. Karthik, S. Mukherjee, P. Petreczky, C. Shugert, and S. Syritsyn, Phys. Rev. D **100**, 034516 (2019), [1905.06349](#).

- [82] X. Gao, L. Jin, C. Kallidonis, N. Karthik, S. Mukherjee, P. Petreczky, C. Shugert, S. Syritsyn, and Y. Zhao, Phys. Rev. D **102**, 094513 (2020), [2007.06590](#).
- [83] H.-W. Lin, J.-W. Chen, Z. Fan, J.-H. Zhang, and R. Zhang, Phys. Rev. D **103**, 014516 (2021), [2003.14128](#).
- [84] C. Alexandrou, K. Cichy, M. Constantinou, J. R. Green, K. Hadjiyiannakou, K. Jansen, F. Manigrasso, A. Scapellato, and F. Steffens, Phys. Rev. D **103**, 094512 (2021), [2011.00964](#).
- [85] C. Alexandrou, M. Constantinou, K. Hadjiyiannakou, K. Jansen, and F. Manigrasso, Phys. Rev. Lett. **126**, 102003 (2021), [2009.13061](#).
- [86] Z. Fan, X. Gao, R. Li, H.-W. Lin, N. Karthik, S. Mukherjee, P. Petreczky, S. Syritsyn, Y.-B. Yang, and R. Zhang, Phys. Rev. D **102**, 074504 (2020), [2005.12015](#).
- [87] C. Alexandrou, K. Cichy, M. Constantinou, K. Hadjiyiannakou, K. Jansen, A. Scapellato, and F. Steffens, Phys. Rev. Lett. **125**, 262001 (2020), [2008.10573](#).
- [88] Q.-A. Zhang et al. (Lattice Parton), Phys. Rev. Lett. **125**, 192001 (2020), [2005.14572](#).
- [89] C. Alexandrou, S. Bacchio, M. Constantinou, J. Finkenrath, K. Hadjiyiannakou, K. Jansen, G. Koutsou, H. Panagopoulos, and G. Spanoudes, Phys. Rev. D **101**, 094513 (2020), [2003.08486](#).
- [90] Y.-B. Yang, J. Liang, Y.-J. Bi, Y. Chen, T. Draper, K.-F. Liu, and Z. Liu, Phys. Rev. Lett. **121**, 212001 (2018), [1808.08677](#).
- [91] C. Alexandrou, M. Constantinou, K. Hadjiyiannakou, K. Jansen, C. Kallidonis, G. Koutsou, A. Vaquero Avilés-Casco, and C. Wiese, Phys. Rev. Lett. **119**, 142002 (2017), [1706.02973](#).

- [92] P. E. Shanahan and W. Detmold, Phys. Rev. D **99**, 014511 (2019), [1810.04626](#).
- [93] Z.-Y. Fan, Y.-B. Yang, A. Anthony, H.-W. Lin, and K.-F. Liu, Phys. Rev. Lett. **121**, 242001 (2018), [1808.02077](#).
- [94] Z. Fan, R. Zhang, and H.-W. Lin (2020), [2007.16113](#).
- [95] Z. Fan and H.-W. Lin (2021), [2104.06372](#).
- [96] M. Peardon, J. Bulava, J. Foley, C. Morningstar, J. Dudek, R. G. Edwards, B. Joo, H.-W. Lin, D. G. Richards, and K. J. Juge (Hadron Spectrum), Phys. Rev. D **80**, 054506 (2009), [0905.2160](#).
- [97] C. R. Allton et al. (UKQCD), Phys. Rev. D **47**, 5128 (1993), [hep-lat/9303009](#).
- [98] C. Morningstar and M. J. Peardon, Phys. Rev. D **69**, 054501 (2004), [hep-lat/0311018](#).
- [99] J. Bulava, M. Donnellan, and R. Sommer, JHEP **01**, 140 (2012), [1108.3774](#).
- [100] C. Egerer, D. Richards, and F. Winter, Phys. Rev. D **99**, 034506 (2019), [1810.09991](#).
- [101] C. Egerer, R. G. Edwards, K. Orginos, and D. G. Richards, Phys. Rev. D **103**, 034502 (2021), [2009.10691](#).
- [102] C. Egerer, R. G. Edwards, C. Kallidonis, K. Orginos, A. V. Radyushkin, D. G. Richards, E. Romero, and S. Zafeiropoulos (2021), [2107.05199](#).
- [103] G. S. Bali, B. Lang, B. U. Musch, and A. Schäfer, Phys. Rev. D **93**, 094515 (2016), [1602.05525](#).
- [104] R. Edwards, B. Joó, K. Orginos, D. Richards, and F. Winter, U.S. 2+1 flavor clover lattice generation program (2016), [unpublished](#).

- [105] S. Duane, A. D. Kennedy, B. J. Pendleton, and D. Roweth, *Phys. Lett. B* **195**, 216 (1987).
- [106] H.-W. Lin et al. (Hadron Spectrum), *Phys. Rev. D* **79**, 034502 (2009), [0810.3588](#).
- [107] S. Borsanyi et al., *JHEP* **09**, 010 (2012), [1203.4469](#).
- [108] M. Gockeler, R. Horsley, D. Pleiter, P. E. L. Rakow, G. Schierholz, C. M. Maynard, and D. G. Richards (QCDSF, UKQCD, LHPC), *Phys. Lett. B* **532**, 63 (2002), [hep-lat/0106022](#).
- [109] S. Sasaki, T. Blum, and S. Ohta, *Phys. Rev. D* **65**, 074503 (2002), [hep-lat/0102010](#).
- [110] W. Melnitchouk, S. O. Bilson-Thompson, F. D. R. Bonnet, J. N. Hedditch, F. X. Lee, D. B. Leinweber, A. G. Williams, J. M. Zanotti, and J. B. Zhang, *Phys. Rev. D* **67**, 114506 (2003), [hep-lat/0202022](#).
- [111] D. Brommel, P. Crompton, C. Gattringer, L. Y. Glozman, C. B. Lang, S. Schaefer, and A. Schafer (Bern-Graz-Regensburg), *Phys. Rev. D* **69**, 094513 (2004), [hep-ph/0307073](#).
- [112] S. Basak, R. G. Edwards, G. T. Fleming, K. J. Juge, A. Lichtl, C. Morningstar, D. G. Richards, I. Sato, and S. J. Wallace, *Phys. Rev. D* **76**, 074504 (2007), [0709.0008](#).
- [113] M. S. Mahbub, A. O. Cais, W. Kamleh, B. G. Lasscock, D. B. Leinweber, and A. G. Williams, *Phys. Rev. D* **80**, 054507 (2009), [0905.3616](#).
- [114] J. M. Bulava et al., *Phys. Rev. D* **79**, 034505 (2009), [0901.0027](#).
- [115] M. S. Mahbub, A. O. Cais, W. Kamleh, D. B. Leinweber, and A. G. Williams, *Phys. Rev. D* **82**, 094504 (2010), [1004.5455](#).

- [116] J. Bulava, R. G. Edwards, E. Engelson, B. Joo, H.-W. Lin, C. Morningstar, D. G. Richards, and S. J. Wallace, Phys. Rev. D **82**, 014507 (2010), [1004.5072](#).
- [117] C. Alexandrou, T. Korzec, G. Koutsou, and T. Leontiou, Phys. Rev. D **89**, 034502 (2014), [1302.4410](#).
- [118] S. Basak, R. G. Edwards, G. T. Fleming, U. M. Heller, C. Morningstar, D. Richards, I. Sato, and S. Wallace, Phys. Rev. D **72**, 094506 (2005), [hep-lat/0506029](#).
- [119] S. Basak, R. Edwards, G. T. Fleming, U. M. Heller, C. Morningstar, D. Richards, I. Sato, and S. J. Wallace (Lattice Hadron Physics (LHPC)), Phys. Rev. D **72**, 074501 (2005), [hep-lat/0508018](#).
- [120] J. J. Dudek, R. G. Edwards, N. Mathur, and D. G. Richards, Phys. Rev. D **77**, 034501 (2008), [0707.4162](#).
- [121] C. J. Morningstar and M. Peardon, Phys. Rev. D **60**, 034509 (1999), URL <https://link.aps.org/doi/10.1103/PhysRevD.60.034509>.
- [122] M. Lüscher, Commun. Math. Phys. **104**, 177 (1986).
- [123] G. Silvi et al., Phys. Rev. D **103**, 094508 (2021), [2101.00689](#).
- [124] G. Rendon, L. Leskovec, S. Meinel, J. Negele, S. Paul, M. Petschlies, A. Pochinsky, G. Silvi, and S. Syritsyn, Phys. Rev. D **102**, 114520 (2020), [2006.14035](#).
- [125] C. B. Lang, L. Leskovec, M. Padmanath, and S. Prelovsek, Phys. Rev. D **95**, 014510 (2017), [1610.01422](#).
- [126] J.-H. Zhang, X. Ji, A. Schäfer, W. Wang, and S. Zhao, Phys. Rev. Lett. **122**, 142001 (2019), [1808.10824](#).

- [127] Z.-Y. Li, Y.-Q. Ma, and J.-W. Qiu, Phys. Rev. Lett. **122**, 062002 (2019), [1809.01836](#).
- [128] T. Izubuchi, X. Ji, L. Jin, I. W. Stewart, and Y. Zhao, Phys. Rev. D **98**, 056004 (2018), [1801.03917](#).
- [129] X. Ji, J.-H. Zhang, and Y. Zhao, Phys. Rev. Lett. **120**, 112001 (2018), [1706.08962](#).
- [130] J. Green, K. Jansen, and F. Steffens, Phys. Rev. Lett. **121**, 022004 (2018), [1707.07152](#).
- [131] I. Balitsky, W. Morris, and A. Radyushkin, in 28th International Workshop on Deep Inelastic Scattering and Related Subjects (2021), [2106.01916](#).
- [132] A. S. Gambhir, A. Stathopoulos, K. Orginos, B. Yoon, R. Gupta, and S. Syritsyn, PoS **LATTICE2016**, 265 (2016), [1611.01193](#).
- [133] S. O. Bilson-Thompson, D. B. Leinweber, and A. G. Williams, Annals Phys. **304**, 1 (2003), [hep-lat/0203008](#).
- [134] M. Lüscher, JHEP **08**, 071 (2010), [Erratum: JHEP 03, 092 (2014)], [1006.4518](#).
- [135] M. Lüscher and P. Weisz, JHEP **02**, 051 (2011), [1101.0963](#).
- [136] M. Lüscher, JHEP **04**, 123 (2013), [1302.5246](#).
- [137] C. Bouchard, C. C. Chang, T. Kurth, K. Orginos, and A. Walker-Loud, Phys. Rev. D **96**, 014504 (2017), [1612.06963](#).
- [138] B. Blossier, M. Della Morte, G. von Hippel, T. Mendes, and R. Sommer, JHEP **04**, 094 (2009), [0902.1265](#).

- [139] M. Lüscher and U. Wolff, Nucl. Phys. B **339**, 222 (1990).
- [140] U. Wolff (ALPHA), Comput. Phys. Commun. **156**, 143 (2004), [Erratum: Comput.Phys.Commun. 176, 383 (2007)], [hep-lat/0306017](#).
- [141] N. Madras and A. D. Sokal, J. Statist. Phys. **50**, 109 (1988).
- [142] S. Meinel, XMBF software package 2.40 (2013).
- [143] S. Meinel, Doctoral thesis (2010).
- [144] J. J. Dudek, R. G. Edwards, and C. E. Thomas, Phys. Rev. D **86**, 034031 (2012), [1203.6041](#).
- [145] R. S. Sufian, T. Liu, and A. Paul, Phys. Rev. D **103**, 036007 (2021), [2012.01532](#).
- [146] J. Karpie, K. Orginos, A. Rothkopf, and S. Zafeiropoulos, JHEP **04**, 057 (2019), [1901.05408](#).
- [147] K. Cichy, L. Del Debbio, and T. Giani, JHEP **10**, 137 (2019), [1907.06037](#).
- [148] L. Del Debbio, T. Giani, J. Karpie, K. Orginos, A. Radyushkin, and S. Zafeiropoulos, JHEP **02**, 138 (2021), [2010.03996](#).
- [149] H. Abramowicz et al. (H1, ZEUS), Eur. Phys. J. C **75**, 580 (2015), [1506.06042](#).
- [150] Y.-B. Yang, M. Gong, J. Liang, H.-W. Lin, K.-F. Liu, D. Pefkou, and P. Shanahan, Phys. Rev. D **98**, 074506 (2018), [1805.00531](#).
- [151] G. F. de Téramond, H. G. Dosch, T. Liu, R. S. Sufian, S. J. Brodsky, and A. Deur (2021), [2107.01231](#).
- [152] A. J. Woss, J. J. Dudek, R. G. Edwards, C. E. Thomas, and D. J. Wilson (Hadron Spectrum), Phys. Rev. D **103**, 054502 (2021), [2009.10034](#).

- [153] R. A. Briceño and M. T. Hansen, Phys. Rev. D **92**, 074509 (2015), [1502.04314](#).
- [154] R. A. Briceño, M. T. Hansen, and A. Walker-Loud, Phys. Rev. D **91**, 034501 (2015), [1406.5965](#).
- [155] R. A. Briceño and M. T. Hansen, Phys. Rev. D **94**, 013008 (2016), [1509.08507](#).
- [156] F. M. Stokes, W. Kamleh, and D. B. Leinweber, Phys. Rev. D **102**, 014507 (2020), [1907.00177](#).
- [157] F. M. Stokes, W. Kamleh, and D. B. Leinweber, PoS **LATTICE2019**, 182 (2019), [2001.07919](#).